# Lightning return stroke current waveforms aloft from measured field change, current, and channel geometry

J. C. Willett,[1] D. M. Le Vine,[2] and V. P. Idone[3]

Received 6 October 2006; revised 8 May 2007; accepted 9 November 2007; published 9 April 2008.

[1] Three-dimensional reconstructions of six rocket-triggered lightning channels are derived from stereo photographs. These reconstructed channels are used to infer the behavior of the current in return strokes above the ground from current waveforms measured at the channel base and electric field change waveforms measured at a range of 5.2 km for 24 return strokes in these channels. Streak photographs of 14 of the same strokes are analyzed to determine the risetimes, propagation speeds, and amplitudes of relative light intensity for comparison with the electrical inferences. Results include the following: (1) The fine structure of the field change waveforms that were radiated by these subsequent return strokes can be explained, in large part, by channel geometry. (2) The average 10–90% risetime of the stroke current increased by about a factor of seven in our sample, from an observed 0.31 ± 0.17 $\mu$s at the surface to an inferred 2.2 ± 0.5 $\mu$s at 1 km path length above the surface. (3) The three-dimensional propagation speed of the current front averaged 1.80 ± 0.24 × $10^8$ m/s over channel lengths typically greater than 1 km. (4) Assuming that the measured current was entirely due to the return stroke forced an unreasonably large and abrupt reduction in inferred current amplitude over the first few tens of meters above the surface, especially in cases when the leader was bright relative to its stroke. Therefore a significant fraction of the current at the surface was probably due to the leader in such cases. (5) Independent of the above, peak return stroke currents decreased by approximately 37 ± 12% between 100 m and 1 km of path length above the surface. Because of uncertainty about how to partition the measured current between leader and return stroke, however, we are unable to infer the variation of current amplitude near the ground.

**Citation:** Willett, J. C., D. M. Le Vine, and V. P. Idone (2008), Lightning return stroke current waveforms aloft from measured field change, current, and channel geometry, *J. Geophys. Res.*, *113*, D07305, doi:10.1029/2006JD008116.

## 1. Introduction

[2] The return strokes in cloud-to-ground lightning flashes are the most powerful known lightning processes in terms of both local energy dissipation and electromagnetic radiation [e.g., *Guo and Krider*, 1982; *Willett et al.*, 1990]. Although the threat that they pose to objects on the ground has now been reasonably well quantified, the peak electric currents, current risetimes, and electromagnetic field intensities above the surface are not known. These quantities have practical importance to the hardening of aircraft and missiles, which can trigger lightning discharges in flight [*Mazur et al.*, 1984; *Christian et al.*, 1989], since the flashes so triggered are likely to contain return strokes if initiated close enough to the ground. "In testing to determine the immunity of a system to a direct lightning strike... the flash current is generally that observed at the base of a severe flash to ground even though aircraft and space vehicles in flight will likely encounter the smaller currents associated either with the upper portion of return strokes or with various in-cloud currents from either ground or cloud discharges" [*Uman*, 1988, p. 1560].

[3] In addition to this engineering application, information about the evolution of speed, shape, and amplitude of the upward propagating current waveform is needed to test, and to guide the further development of, physical models of the return stroke [e.g., *Strawe*, 1979; *Mattos and Christopoulos*, 1990]. Such models give predictions of these quantities that (except for propagation speed) have yet to be compared to observations above the surface.

[4] Direct measurements of the current waveforms in both natural and rocket-triggered return strokes exist, but only at the channel base [*Berger et al.*, 1975; *Eriksson*, 1978; *Garbagnati and Lo Pipero*, 1982; *Leteinturier et al.*, 1990; *Leteinturier and Hamelin*, 1991; *Fisher et al.*, 1993; *Depasse*, 1994; *Crawford*, 1998; *Uman et al.*, 2000; *Schoene et al.*, 2003]. Time-resolved photographic and photoelectric measurements that show the evolution of

[1]Garrett Park, Maryland, USA.
[2]NASA Goddard Space Flight Center, Greenbelt, Maryland, USA.
[3]Department of Earth and Atmospheric Sciences, State University of New York at Albany, Albany, New York, USA.

Copyright 2008 by the American Geophysical Union.
0148-0227/08/2006JD008116

luminosity along the visible channel on microsecond temporal, and several-meter spatial, scales are also available [*Schonland et al.*, 1935; *Idone and Orville*, 1982; *Jordan and Uman*, 1983; *Idone et al.*, 1984; *Mach and Rust*, 1989; *Jordan et al.*, 1997; *Wang et al.*, 1999a, 1999b; *Olsen et al.*, 2004]. These optical measurements generally imply that the propagation speed and the peak amplitude of return stroke current waveforms both decrease with increasing height above the surface, while the current risetime increases with height. (One exception is *Olsen et al.* [2004], who reported that the photoelectric stroke propagation speed increased with height over the lowest 100–200 m of five strokes in a rocket-triggered flash.)

[5] Unfortunately, the relation between optical emission per unit channel length and instantaneous current is not well known under the conditions found in lightning return strokes. *Colvin et al.* [1987] found an approximately linear relation between instantaneous current and channel brightness in oscillatory laboratory discharges having current periods of about 2 ms. These discharges were intended to simulate "nuclear lightning," however, so their timescales were slow enough that pressure equilibrium was well established within the current-carrying channels. *Murphy et al.* [1986, Figure 13] made similar measurements on a laboratory discharge ringing with about 30 $\mu$s period and having a current rise rate of approximately 10 kA/$\mu$s. (Note that this current derivative is roughly one order of magnitude smaller than those typically measured at the channel base in rocket-triggered return strokes [*Leteinturier et al.*, 1990; *Leteinturier and Hamelin*, 1991; *Schoene et al.*, 2003] but might be comparable to those occurring in lightning channels a few hundred meters above the ground.) *Murphy et al.* [1986, p. 8] concluded, "This discharge rings on a timescale too short for pressure equilibrium to be established with the surrounding atmosphere, thus its brightness is not a simple function of the discharge current." *Gomes and Cooray* [1998] measured the optical emissions from the entire length of laboratory sparks in 250 mm and 500 mm gaps. They found that, for a current risetime of 1.1 $\mu$s, the optical risetime remained near 1.2 $\mu$s over a range of peak currents from 0.6 to 3.5 kA; that optical and current risetimes were nearly proportional over a range of 0.3 to 15 $\mu$s (peak current varied with risetime); and that peak optical emission was approximately linearly related to peak current, although with a large zero intercept that eliminated any proportionality between these two parameters.

[6] In measurements on rocket-triggered lightning, *Idone and Orville* [1985] reported approximate proportionality between peak current measured at the ground and peak relative luminosity about 50 m above ground for 20 strokes in one flash and 17 strokes in another. *Wang et al.* [2005] found proportionality between instantaneous current and instantaneous relative light intensity in the lowest 3.6 m of channel during the rapidly rising portion only of four triggered strokes. Nevertheless, the contradictory nature of the laboratory results to date makes it premature to deduce current behavior directly from optical luminosity measurements.

[7] (Note further that rocket-triggered lightning differs from natural cloud-to-ground lightning in that the former has no analog to the natural first return stroke [e.g., *Uman*, 1987, section 12.5]. *Le Vine et al.* [1989] have argued the similarity between rocket-triggered and natural subsequent strokes, on the basis of wideband recordings of their radiation fields, but the current waveforms in natural first strokes are expected to be different for various reasons (see review and discussion by *Willett et al.* [1995]). Thus the results in this paper may not apply to natural first return strokes.)

[8] There are numerous, semiempirical, "engineering" models of return stroke currents in the literature [e.g., *Bruce and Golde*, 1941; *Uman and McLain*, 1970; *Lin et al.*, 1980; *Hubert*, 1985; *Heidler*, 1985; *Diendorfer and Uman*, 1990; *Baba and Ishii*, 2002]. These and other model variations have been reviewed and extended by *Nucci et al.* [1990], *Thottappillil and Uman* [1993], and *Rakov and Uman* [1998]. Many of these models have been tested against observed channel base current and remote electromagnetic field waveforms [*Lin et al.*, 1980; *Thottappillil and Uman*, 1993; *Rakov and Uman*, 1998], but only assuming a straight, vertical lightning channel and a "realistic" profile of propagation speed. *Le Vine and Willett* [1995] have presented evidence, however, that the channel morphology plays an important role in determining the structure of the radiation field waveform, even for subsequent return strokes.

[9] *Master et al.* [1981] computed the electromagnetic fields to be expected aloft from a nearby return stroke, on the basis of a modification of the model of *Lin et al.* [1980], but they could find no measurements with which to compare their results. More recently, *Reazer et al.* [1987], *Mazur et al.* [1990], and *Mazur and Moreau* [1992] have presented in situ observations of a few events in direct lightning strikes to aircraft that they believe to have been return strokes, but the evidence for this claim is problematic. *Reazer et al.* [1987] found peak currents of 1–4 kA and risetimes around 2 $\mu$s in these events, in agreement with the general expectation that return stroke peak currents should be smaller, and current risetimes should be longer, aloft than at the ground. *Mazur et al.* [1990] and *Mazur and Moreau* [1992] did not report peak currents or risetimes, but *Mazur and Moreau* [1992, p. 579] state, "...return stroke currents at flight altitudes are much smaller in amplitude than those measured on the ground, and are usually smaller than current pulses of dart leaders and recoil streamers. This observation strongly indicates the need for reexamining the threat to aircraft from return strokes."

## 2. Data and Approach

[10] The present paper exploits an existing set of channel base current recordings, stereo still photographs, streak photographs, and remote electric field waveforms of rocket-triggered lightning return strokes to deduce quantitative features of their current waveforms above the ground. This uniquely comprehensive data set was obtained during the summer of 1987 at the NASA Kennedy Space Center in Florida and has been described in detail by *Willett et al.* [1989a]. A novel feature of these data is the stereo pairs of still photographs, which have enabled piecewise linear reconstruction of the actual three-dimensional geometry of six cloud-to-ground channels, as outlined previously by *Willett and Le Vine* [1995]. (See Appendix A for details.) The reconstructed channels are believed accurate to a few tens of meters or better. They are smooth and approximately straight over the lowest few hundred meters, where the

lightning followed the triggering wires, and tortuous above. Both current and electric field change waveforms were recorded during a total of 24 return strokes in these channels, and two-dimensional stroke propagation speeds were also measured from the streak photographs for 14 of these strokes in five channels.

[11] It has been shown theoretically [*Hill*, 1969; *Le Vine and Meneghini*, 1978; *Le Vine and Kao*, 1988; *Cooray and Orville*, 1990; *Vecchi et al.*, 1994] that kinks and bends in a lightning channel should produce signatures in the return stroke radiation field. For example, if an unchanging current waveform were to propagate at constant speed (the "transmission line model" (TLM) of *Uman and McLain* [1970]) up such a tortuous channel, each successive kink would radiate a facsimile of the current waveform with an amplitude, polarity, and time delay determined by the geometry of that kink relative to the observer [e.g., *Le Vine and Willett*, 1992]. Thus it is tempting to conclude that knowledge of the channel geometry would permit deconvolution of the radiated field to yield the spatial evolution of the current waveform along the channel.

[12] Mathematically, this inverse problem cannot be solved, of course, since the return stroke current is, in general, a function of both time and path length along the lightning channel, whereas the field waveform observed at a single location is a function of time alone. Even if the current were constrained to reduce its dimensionality from two to one, the solution might not be unique. Here the constrained inverse problem is avoided by solving the forward problem with various assumptions about the current distribution and comparing the results to observation. Preliminary results of this approach have been presented by *Willett et al.* [1989b] and by *Willett and Le Vine* [1996, 2002, 2003].

## 3. Calculation of the Field Change

[13] *Le Vine and Meneghini* [1983, equation 26] derived the following equation in vector notation for the total electric field due to a TLM current waveform, $I_{TLM}([t - t_a] - \hat{\mathbf{l}} \cdot [\mathbf{r}' - \mathbf{r_a}']/v)$, propagating on an arbitrarily located, arbitrarily oriented, short, linear channel segment in free space. (This equation is repeated in the work by *Le Vine and Willett* [1992, equation 1], where a sketch of the geometry is also given as Figure 1a.) Here $v$ is the propagation speed of the current waveform, $\hat{\mathbf{l}}$ is a unit vector in the direction of propagation along the channel segment (also taken to be the positive direction for current flow), and $t_a$ is the retarded time that the onset of the waveform, $I_{TLM}(0)$, arrives at the origin of the channel segment, $\mathbf{r_a}'$. (This "retarded" time is delayed by the interval, $|\mathbf{r_a}' - \mathbf{r}|/c$, that is required for information to propagate at the speed of light, $c$, from the origin of the segment to the observer's location, $\mathbf{r}$.)

$$\mathbf{E}(\mathbf{r},t) = -\frac{\mu_0}{4\pi}\int_{\text{segment}} [\dot{I}_{\text{TLM}}]\{\hat{\mathbf{l}} - (\hat{\mathbf{l}}\cdot\nabla R)\nabla R\}\frac{ds'}{R} - \frac{\mu_0 c}{4\pi}\int_{\text{segment}} [I_{\text{TLM}}]\{\hat{\mathbf{l}} - 3(\hat{\mathbf{l}}\cdot\nabla R)\nabla R\}\frac{ds'}{R^2} - \frac{\mu_0 c^2}{4\pi}\int_{\text{segment}} \left\{\int_{-\infty}^{t} [I_{\text{TLM}}]\{\hat{\mathbf{l}} - 3(\hat{\mathbf{l}}\cdot\nabla R)\nabla R\}dt'\right\}\cdot\frac{ds'}{R^3} \quad (1)$$

The integrals in (1) are line integrals that are evaluated along the channel segment. The integrations are to be done in the "primed" coordinate system, where d$s'$ denotes a differential length along the segment, and $\nabla R$ is effectively a unit vector pointing from the source point, $\mathbf{r}'$, to the observer along the separation distance, $R \equiv |\mathbf{r} - \mathbf{r}'|$. The square brackets in the integrands in equation (1) only, [*function*], denote the retarded value of the argument of the enclosed function, and the dot above these brackets denotes a derivative with respect to the single argument of that function.

[14] Starting from the first term in (1), *Le Vine and Willett* [1992, equation B3] derived a simple formula for the electric radiation (i.e., "far") field, measured at the surface of an infinite, horizontal, conducting plane, due to a current-carrying channel segment above that plane:

$$\mathbf{E_{rad}}(\mathbf{r},t) = \frac{\mu_0 v}{2\pi R_0}\frac{\sin(\theta)\left(\hat{\boldsymbol{\theta}}\cdot\hat{\mathbf{l}}\right)\hat{\mathbf{z}}}{\left[1 - \frac{v}{c}\left(\hat{\mathbf{l}}\cdot\nabla R_0\right)\right]}[I_{\text{TLM}}(t - t_a) - I_{\text{TLM}}(t - t_b)] \quad (2)$$

In this formula we have assumed a spherical coordinate system, ($R_0$, $\theta$, $\varphi$), that is centered on the channel segment but has its symmetry axis, $\hat{\mathbf{z}}$, oriented vertically, perpendicular to the conducting plane. (Thus the zenith angle, $\theta$, is greater than 90° for sources above the plane.) The geometrical situation is sketched in Figure 1. $R_0$ is the distance from the center of the segment aloft to the observer on the ground plane, $\mu_0$ is the magnetic permeability of free space, $t_b$ is the retarded time that the onset of the current waveform arrives at the termination of the channel segment, $\mathbf{r_b}'$, and $I_{TLM}(argument)$ is the functional form of the current at the center of that segment.

[15] The "induction" and "static" components of the complete electric field due to the same channel segment can be readily computed from the second and third terms of (1), respectively. They are given in the same notation as (2) by equations (3) and (4):

$$\mathbf{E_{ind}}(\mathbf{r},t) = \frac{\mu_0 c\left|\mathbf{r'_b} - \mathbf{r'_a}\right|\hat{\mathbf{z}}}{2\pi R_0^2}\left[\sin(\theta)\left(\hat{\boldsymbol{\theta}}\cdot\hat{\mathbf{l}}\right) + 2\cos(\theta)\left(\hat{\mathbf{l}}\cdot\nabla R_0\right)\right]\cdot I_{\text{TLM}}\left(t - \frac{t_a + t_b}{2}\right) \quad (3)$$

$$\mathbf{E_{stat}}(\mathbf{r},t) = \frac{\mu_0 c^2\left|\mathbf{r'_b} - \mathbf{r'_a}\right|\hat{\mathbf{z}}}{2\pi R_0^3}\left[\sin(\theta)\left(\hat{\boldsymbol{\theta}}\cdot\hat{\mathbf{l}}\right) + 2\cos(\theta)\left(\hat{\mathbf{l}}\cdot\nabla R_0\right)\right]\cdot\int_{-\infty}^{t} I_{\text{TLM}}\left(t' - \frac{t_a + t_b}{2}\right)dt' \quad (4)$$

(We have used the average retarded arrival time on the segment in question in order to minimize systematic errors in equations (3) and (4).)

[16] As with (1), equations (2)–(4) require the current to obey the TLM, but only within each segment. Thus any desired current distribution can be approximated by dividing the entire lightning channel into short, linear segments and varying the current waveform and propagation speed appropriately between successive segments. These three

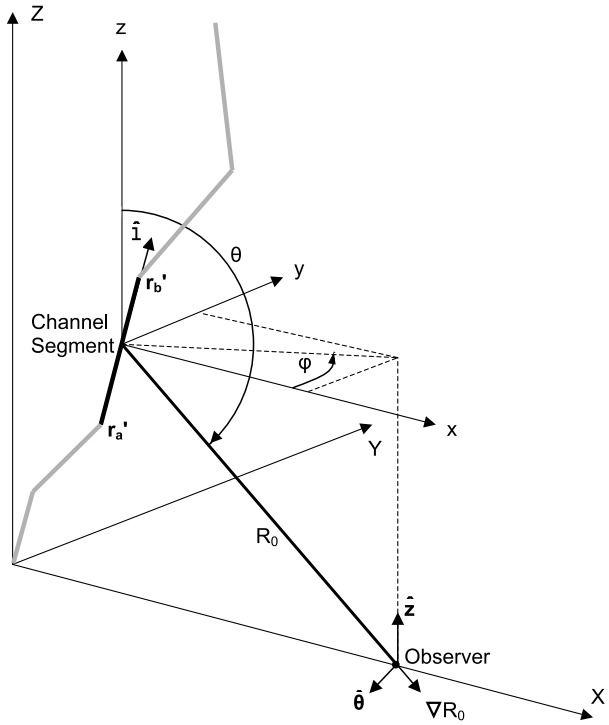


**Figure 1.** Geometry that is assumed in equations (2)–(4) and thereafter. The base of our piecewise linear lightning channel is the origin of the uppercase Cartesian coordinate system, ($X$, $Y$, $Z$), in which the horizontal conducting plane is $X$-$Y$. The observer is located on the $X$ axis in this plane. An auxiliary coordinate system, indicated by lowercase ($x$, $y$, $z$), has its origin at the center of the channel segment of interest (which in this case lies in front of the $X$-$Z$ plane, e.g., at negative $Y$) and its axes parallel to those of the uppercase system. The corresponding spherical coordinate system, ($R_0$, $\theta$, $\varphi$), locates the observer with respect to this channel segment and is used to calculate expressions like $(\hat{\boldsymbol{\theta}} \cdot \hat{\mathbf{l}})$ in equations (2)–(4). (Since $\nabla R_0$ points from the segment to the observer, $\varphi$ is positive in this case and $\theta > \pi/2$ always.)

equations are used here to calculate the total field change that would be produced at the location of the electric field change sensor by various assumed current distributions over all of the segments that make up each piecewise linear, reconstructed channel. Further details of this procedure are outlined in Appendix B.

## 4. Formal Assumptions About the Return Stroke Current Distribution

[17] As indicated above, we expect both the propagation speed and the peak amplitude of return stroke current waveforms to decrease with increasing height above the surface, while the current risetime should increase with height. Therefore we adopt a "generalized TLM" current distribution similar to that of *Cooray and Orville* [1990]. (The engineering models of *Diendorfer and Uman* [1990] and of *Baba and Ishii* [2002] also permit the current risetime to increase with height, which is essential when the lightning channel is tortuous, as we will see below.) The current as a function of time and position on the lightning channel is given by

$$i(t,s) = a(s)I(t_1,s) \tag{5}$$

where $t$ is time measured from stroke onset at the surface, $s$ is path length measured upward from the surface along the tortuous channel, $a(s)$ is an amplitude factor that allows for permanent charge deposition along the channel, and $I(t_1, s)$ is a smoothed version of the current waveform measured at the ground, allowing the risetime to increase with path length as defined in equations (7) and (8), below. $I(t_1, s) \equiv 0$ for $t_1 \leq 0$, and the current onset is assumed to propagate monotonically upward with position-dependent "TLM velocity," $v(s)$. $t_1$ accounts for the resulting propagation delay as a function of $s$:

$$t_1 = t - \int_0^s \frac{ds'}{v(s')} \tag{6}$$

[18] The current waveform that was measured at the surface, $i_0(t)$, is smoothed by convolution with a "smoothing kernel," $K(t, s)$,

$$I(t_1,s) = \int_0^{t_1} i_0(t_1 - t')K(t',s)dt', \quad t_1 > 0 \tag{7}$$

where the limits of integration result from the requirement that both $i_0(t)$ and $K(t, s)$ vanish for $t < 0$. We use the following form for our "causal" smoothing kernel:

$$K(t',s) = \frac{e^{-\frac{t'}{\tau(s)}}t'^2}{2\tau^3(s)}, \quad t' \geq 0 \tag{8}$$

$\tau(s)$ is a timescale that controls the degree of smoothing as a function of path length. (The "equivalent width" (the width of a rectangle with the same peak magnitude and total area) of this smoothing kernel is $[\tau(s)\ e^2]/2$.) $K(t', s)$ has been normalized so that the integral of $I(t_1, s)$ over time is independent of path length. Therefore, although the peak amplitude of $I(t_1, s)$ typically decreases as its risetime increases (a result of increased smoothing due to $\tau(s)$ increasing with $s$), $a(s)$ alone scales the total charge passing any $s$. Notice, however, that the peak current (the maximum over $t$ of $i(t, s)$ at any $s$) is determined not only by $i_0(t)$ but also by both $a(s)$ and $\tau(s)$. Hereafter we refer to this technique of increasing the risetime of the current as "convolution smoothing."

[19] The forms chosen for the various parameters defined above are as follows:

$$a(s) = \left[a_{\min 1} + (1 - a_{\min 1})e^{-s/L_{a1}}\right]\left[a_{\min 2} + (1 - a_{\min 2})e^{-s/L_{a2}}\right] \tag{9}$$

$$v(s) = v_{\min} + (v_{\max} - v_{\min})e^{-s/L_{v1}} + v_{\mathrm{ampl}}\, e^{-s/L_{v2}} \tag{10}$$

$$\tau(s) = \tau_{\max}\left(1 - e^{-s/L_\tau}\right) \tag{11}$$

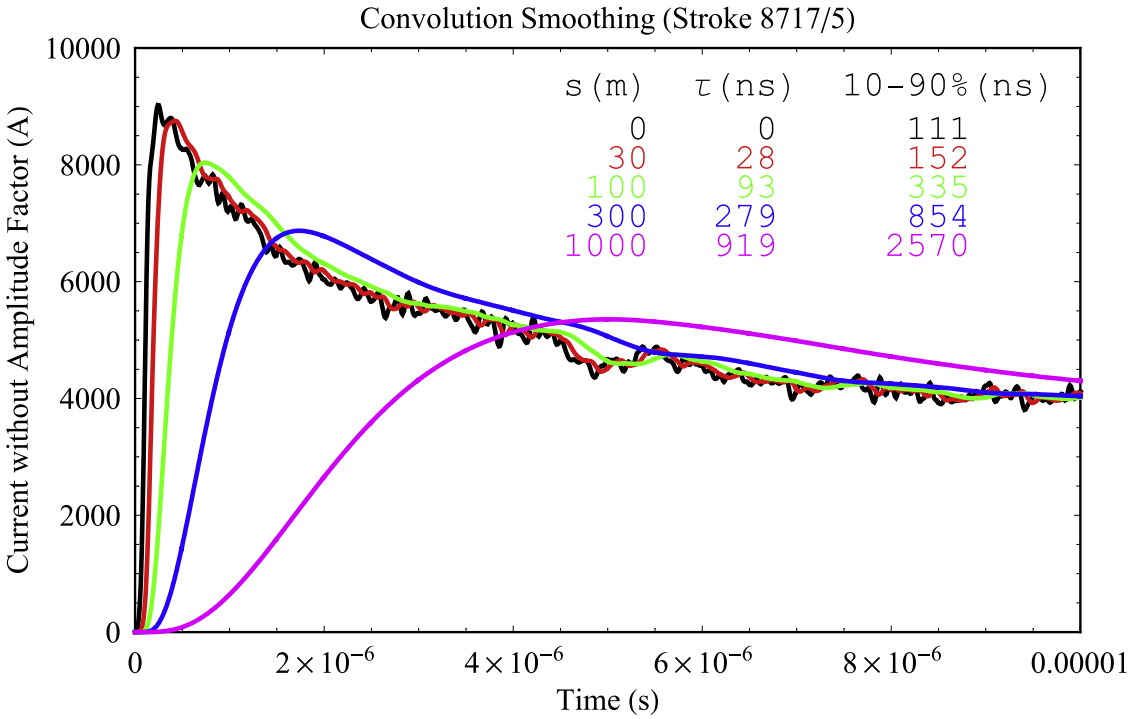


**Figure 2.** An example of our "convolution smoothing" of the measured current waveform (black curve) to produce different waveshapes, $I(t_1, s)$ in equation (7), at different heights. The corresponding values of kernel timescale, $\tau(s)$, and 10–90% risetime are tabulated in the figure.

where $a_{\min 1}$, $a_{\min 2}$, $L_{a1}$, $L_{a2}$, $v_{\min}$, $v_{\max}$, $v_{ampl}$, $L_{v1}$, $L_{v2}$, $\tau_{\max}$, and $L_\tau$ are constants.

[20] Note that the generalized-TLM form that is adopted here (as opposed to the piecewise TLM requirement in the previous section) restricts somewhat the possible current distributions along the return stroke channel. For example, it is not clear whether the class of engineering models known as "current generation" models [*Cooray*, 2003], including the model that was described by *Diendorfer and Uman* [1990], can be represented within this formalism. Nevertheless, the present assumptions allow us to explore the types of current variations that we expect, on the basis of optical observations, while introducing a manageable number of free parameters. An understanding of the effects of these various parameters can be obtained by examining the examples of $I(t_1, s)$ in Figure 2 and of $v(s)$ and $a(s)$ in Figures 6 and 8, respectively, in section 5. (The corresponding free parameter values are given in the figure captions.)

[21] Eleven free parameters may seem like a lot to fit a given observed electric field change waveform. Note, however, that we are really just allowing the current amplitude to vary on two different height scales (often required to fit the peak radiation field, as illustrated below), the TLM velocity to vary on two scales as well, and the current risetime to vary on one height scale. In a later section, a physical explanation is offered for one of the amplitude scales, probably rendering it moot. The second TLM velocity scale is required for only a few strokes. Finally, it is not the values of the individual free parameters themselves, but rather the characters of the variations of current amplitude, risetime, and propagation speed with height, that are the real objectives of this investigation. Therefore our fitting procedure does not turn out to have as many degrees of freedom as it might seem.

## 5. Detailed Example of Fitting Procedure: Stroke 8732/2

[22] The approach that is used in this paper to deduce the evolution of return stroke current with height comprises the following steps: (1) Guess the current parameters in equations (9)–(11). (2) Compute the magnitude of the resulting field change, $E_c(t)$, at the observing site from equations (2)–(4), according to Appendix B. (3) Compare $E_c(t)$ with the measured field change for the same stroke, $E_m(t)$. (4) Iterate until a good fit is obtained. We shall see that this procedure gives reasonably definite results, in spite of the apparent ill-posedness of the general mathematical inversion problem. As an example, we examine in detail the fitting of stroke 2 in flash 8732 (stroke and flash identifiers as in the work by *Willett et al.* [1989a]).

### 5.1. Smoothing and Extrapolation of the Current Waveform

[23] The channel base current for these events was recorded for either 20 $\mu$s (flashes 8715 and 8717) or 5 $\mu$s (flashes 8725–8732), including pretrigger delay. In order to compute $E_c(t)$ for the entire time interval during which the current onset propagates from bottom to top of the visible channel (typically about 10 $\mu$s), it was therefore necessary to extrapolate the measured current waveforms for more than half of the events in our data set. Furthermore, the smaller-amplitude waveforms were rather noisy, leading to

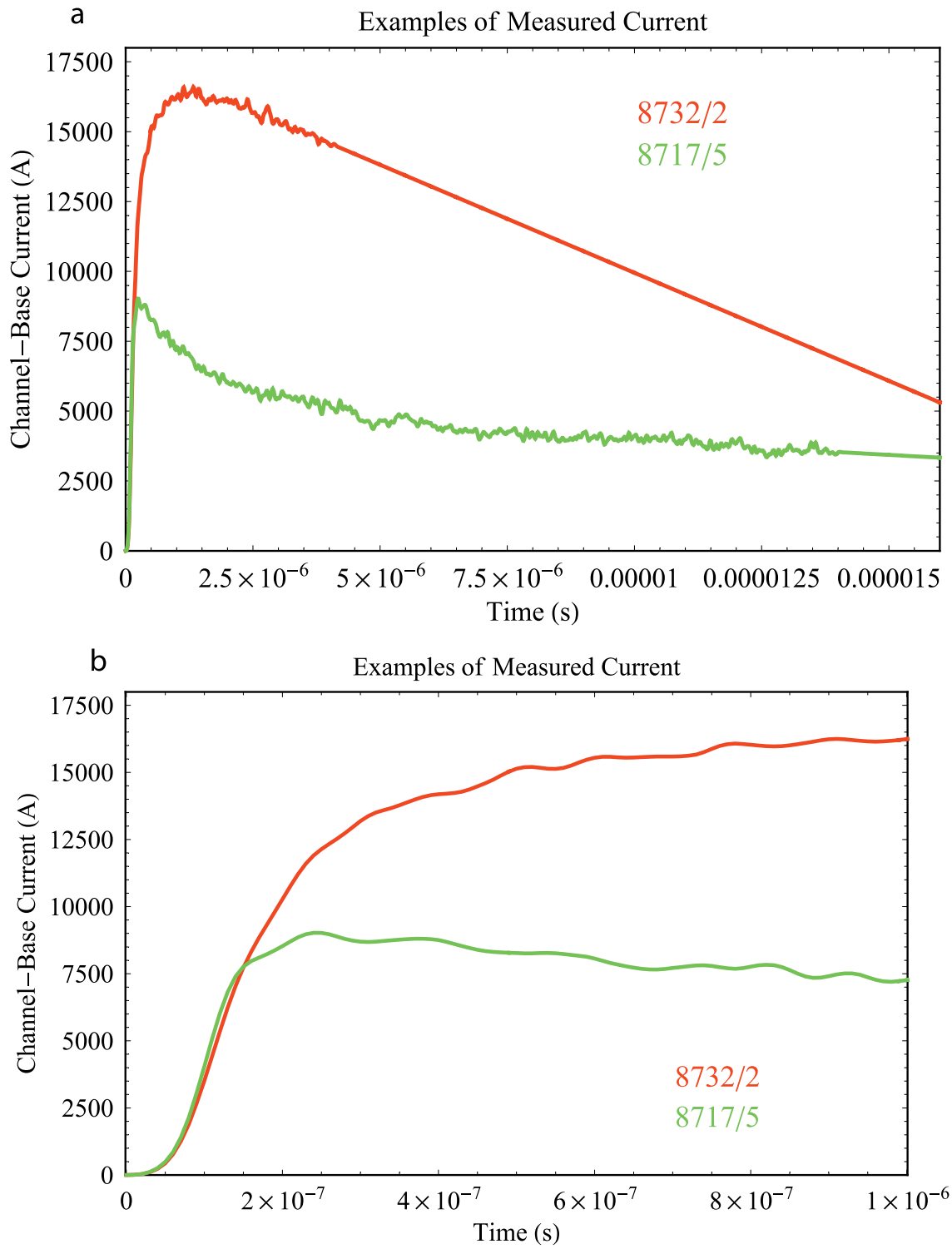


**Figure 3.** Two examples of truncated, smoothed, and extrapolated channel base current waveforms. (a) This figure shows the full 15 $\mu$s time series, illustrating the extrapolations. (b) Similar to Figure 3a but showing only the first 1 $\mu$s, illustrating onset truncation and noise smoothing.

(1) uncertainty in the precise time of current onset and (2) spurious noise in our piecewise linear calculation of the radiation field via equation (2), so some smoothing was beneficial. (If the current waveform is significantly different on adjoining channel segments, errors are produced in the radiated field. These errors can be minimized either by smoothing the channel base current or by using inconveniently short channel segments near the ground.)

[24] In practice, the onset of the measured current waveform was truncated at some small magnitude (less than the

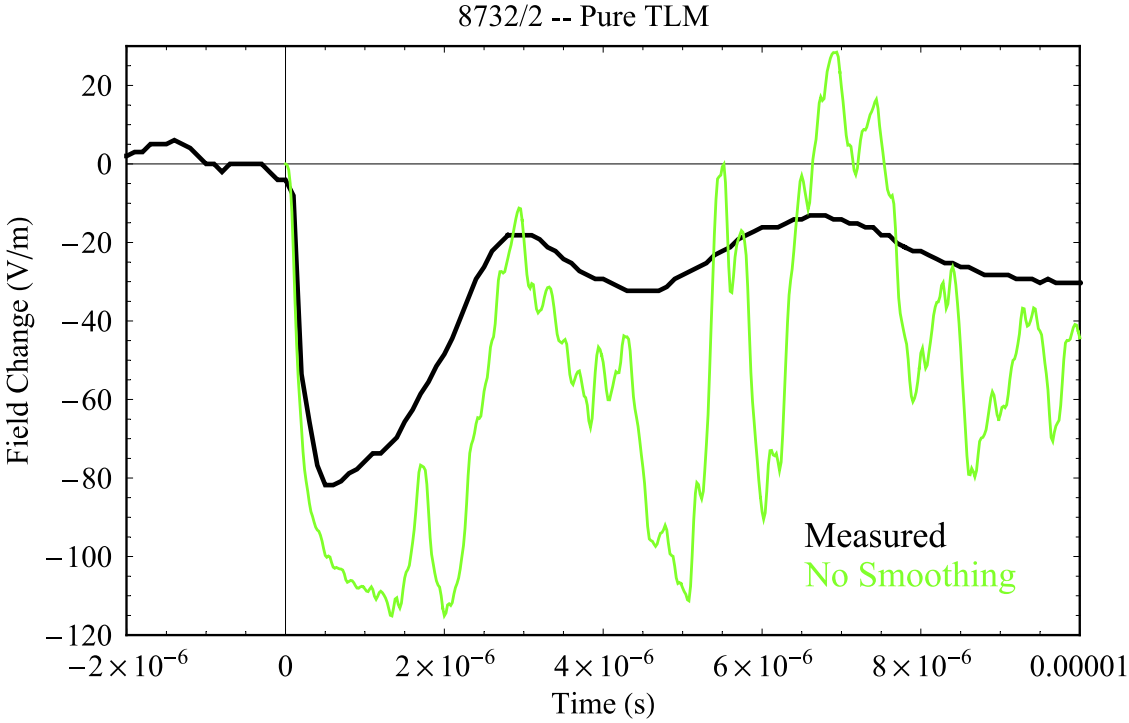


**Figure 4.** Measured field change for stroke 8732/2 (top curve) compared to that calculated when the measured current waveform propagates at a constant speed of $1.71 \times 10^8$ m/s without changing either shape or amplitude (bottom curve).

digitization interval), and then the remaining record was smoothed with a tapered, 11-point (60 ns FWHM) moving average. This resulted in a relatively smooth $i_0(t)$ having a definite onset time ($t = 0$) without appreciably changing its risetime or waveshape. Next the decaying portion of the recorded waveform, starting well after the peak, was fitted with the sum of a constant, a linear slope, and (in many of the cases) an exponential decay. The resulting analytic shape was used to extrapolate $i_0(t)$ to later times, as needed. This quasi-objective extrapolation procedure is not regarded as part of the matching of $E_c(t)$ to $E_m(t)$, per se. In most cases the results are reasonable (see Figure 3 for two examples), but they appeared to produce artifacts in a few cases, as we shall see later.

### 5.2. Determination of Current Risetime

[25] The most obvious result of our analysis, first reported by *Willett et al.* [1989b] and by *Willett and Le Vine* [1996], is that the current risetime must increase rapidly with height (or with path length, $s$) in order for $E_c(t)$ to resemble $E_m(t)$. Thus the first step in our fitting procedure was always to adjust $\tau_{max}$ and $L_\tau$ in equation (11) in order to obtain an $E_c(t)$ with approximately the right amount of "fine structure."

[26] Figure 4 illustrates the excessive fine structure that is obtained for stroke 8732/2 if $i_0(t)$ (see Figure 3) is allowed the propagate up the reconstructed channel at a constant speed of $1.71 \times 10^8$ m/s, effectively the pure TLM. (Note that this propagation speed along our 3-D channel was chosen to be somewhat faster than the measured 2-D propagation speed of $1.6 \times 10^8$ m/s ± 20% in order to line up the major waveform features in time.) The fine structure on $E_c(t)$ is reduced to a more reasonable level, as shown by the green curve in Figure 5, when $\tau_{max} = 4.36$ $\mu$s and $L_\tau = 7084$ m (that is, $\tau(s)$ is nearly linear with an initial slope of 0.615 $\mu$s/km). Unfortunately, the remaining fine structure is now delayed significantly with respect to that of the observed waveform, forcing us to adjust the propagation speed. The reason for this delay is that increased smoothing (via equations (7) and (8)) delays the fast rising portion of the current waveform by an increased interval relative to current onset (which, by definition, propagates according to $v(s)$) (see also Figure 2).

### 5.3. Determination of Propagation Speed

[27] The horizontal, solid green line in Figure 6 illustrates the constant TLM velocity profile that corresponds to the green curve in Figure 5. In the numerical code it is possible to calculate, at each time step, the propagation speed of the half-amplitude point on the rising portion of the current front, while accounting for the fact that the current waveform is becoming increasingly smooth (the risetime is becoming longer) with increasing height. (Later, this calculation also accounts for a decreasing amplitude factor, $a(s)$, with height.) For $v(s) = 1.71 \times 10^8$ m/s, the resulting "front velocity, $v_{eff}(s)$," as we call this calculated effective speed, is shown by the green dots in Figure 6. Notice that, not only is $v_{eff}(s)$ significantly slower than $v(s)$, but it also increases somewhat with height.

[28] In general, we adjusted the TLM velocity profile so that the fine structure of $E_c(t)$ coincided in time with that of $E_m(t)$, while striving to keep the front velocity constant or

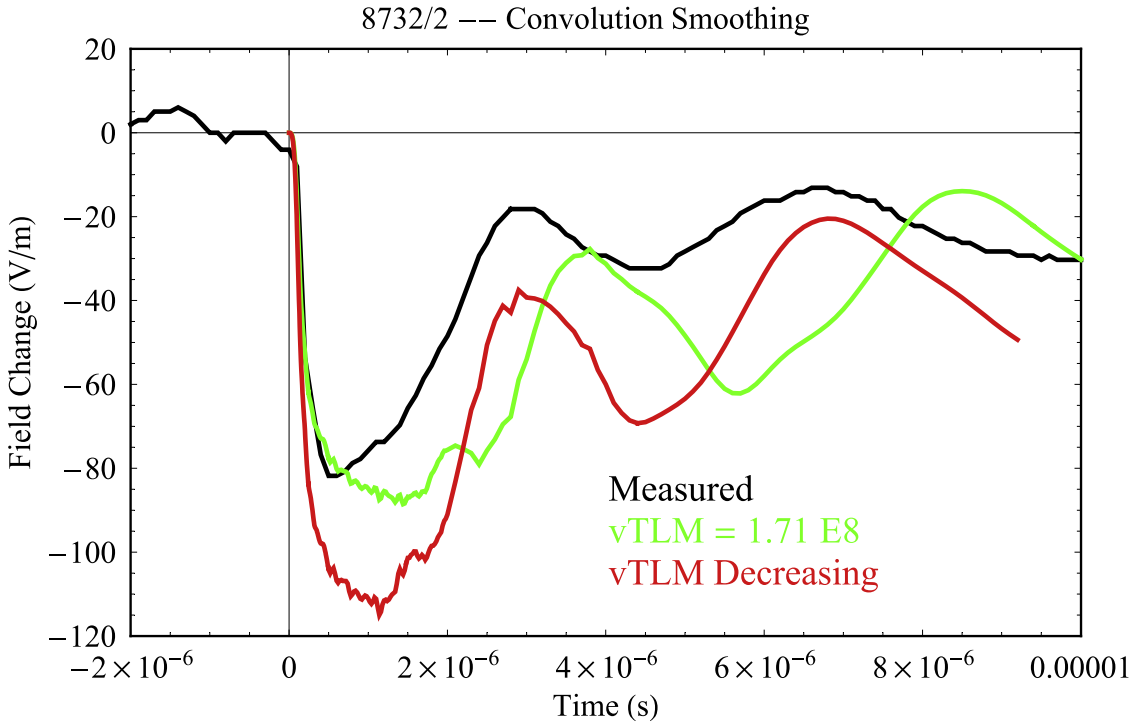


**Figure 5.** Similar to Figure 4 but this time convolution smoothing ($\tau_{max}$ = 4.36 $\mu$s, $L_\tau$ = 7084 m) is included to produce the green curve and then decreasing TLM velocity ($v_{min}$ = 2.1 × $10^8$ m/s, $v_{max}$ = 2.6 × $10^8$, $L_{v1}$ = 500 m) is added to produce the red curve.

decreasing with height. (The latter was not always possible, however, as shown below.) For stroke 8732/2 a nearly constant $v_{eff}(s)$ was obtained with $v_{min}$ = 2.1 × $10^8$ m/s, $v_{max}$ = 2.6 × $10^8$ m/s, $v_{ampl}$ = 0, and $L_{v1}$ = 500 m, as shown by the red profiles of Figure 6. Here the average front velocity is almost exactly 1.71 × $10^8$ m/s, and the fine structure of the resulting $E_c(t)$ waveform is in good temporal

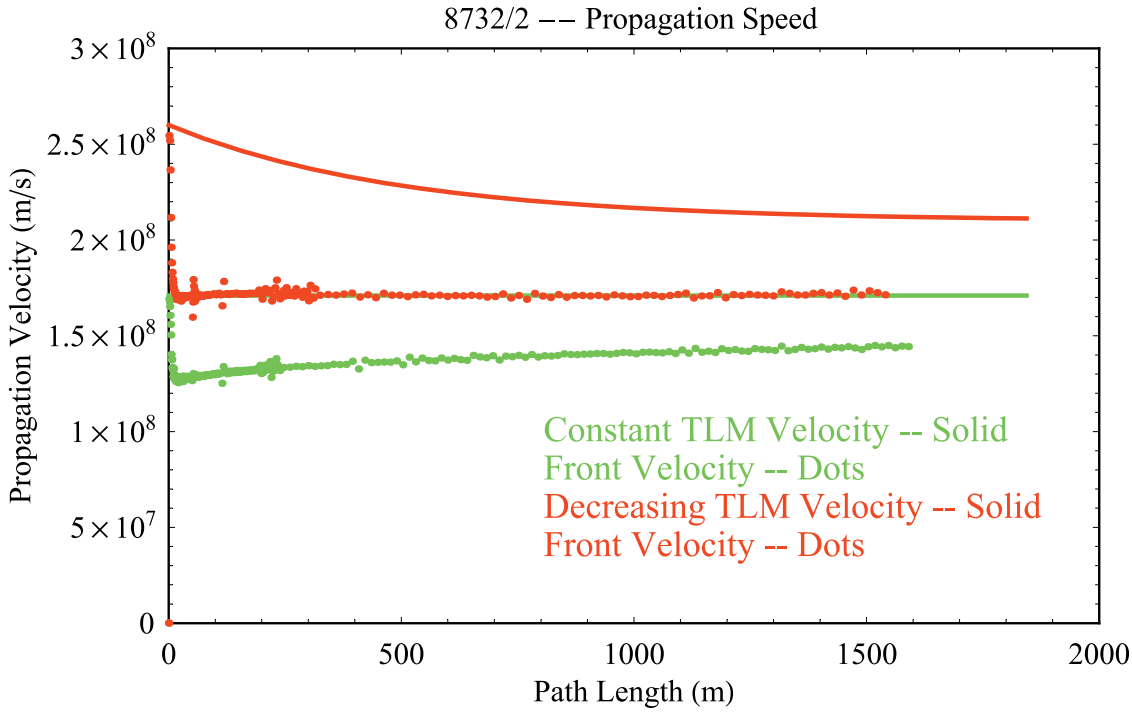


**Figure 6.** TLM velocity profiles ($v(s)$, solid curves) and current front effective velocity profiles ($v_{eff}(s)$, dots) for the two calculations shown in Figure 5 (colors correspond).

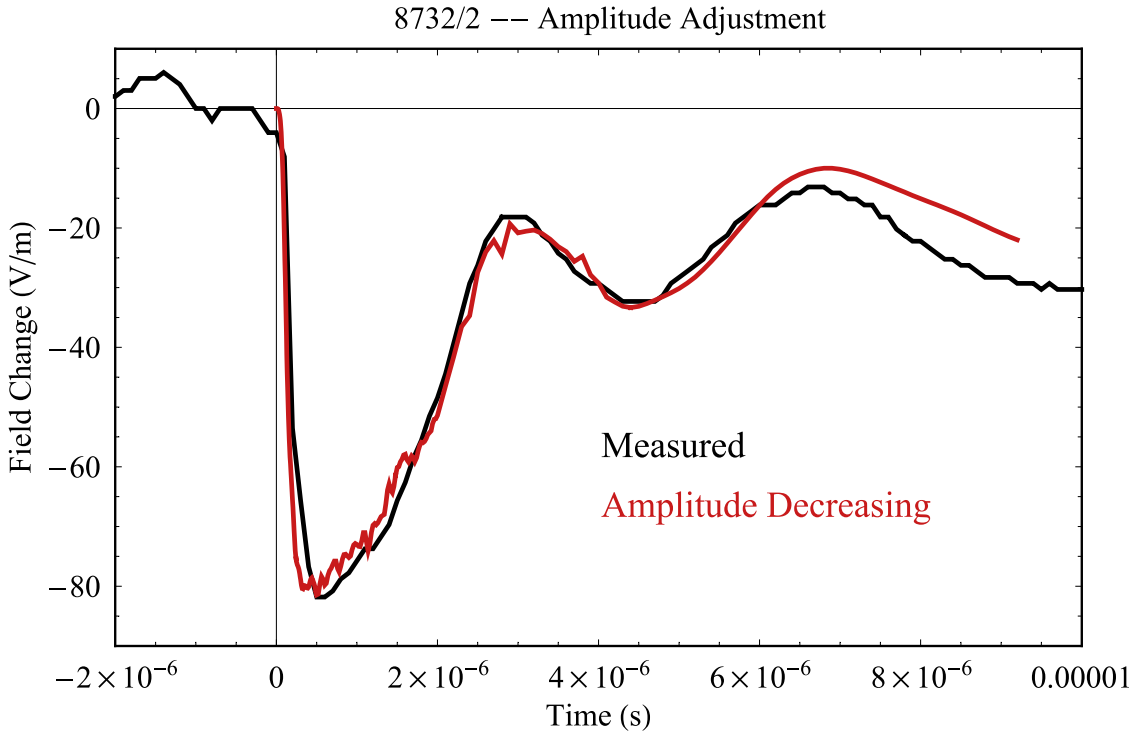


**Figure 7.** Similar to Figure 5 except that the simulation (red curve) has been further modified by a decreasing amplitude factor ($a_{\min 1}$ = 0.7, $L_{a1}$ = 60 m, $a_{\min 2}$ = 0.6, $L_{a2}$ = 400 m).

agreement with that of $E_m(t)$, as can be seen from the red curve in Figure 5.

### 5.4. Determination of Amplitude Factor

[29] It turns out to be generally true (at least within the context of equations (5)−(11)) that the amplitude of $E_c(t)$ is directly proportional, not to $v(s)$, but to $v_{eff}(s)$. Thus it is not surprising to find the peak amplitude of the red curve in Figure 5 (corresponding to $v_{eff}(s) \approx 1.7 \times 10^8$ m/s) to be about 29% larger than that of the green curve ($v_{eff}(s) \approx 1.3 \times 10^8$ m/s). Unfortunately, the red curve also peaks about 37% higher than the black curve, $E_m(t)$, indicating that some adjustment of the current amplitude is required.

[30] It is not satisfactory in general to eliminate this "overprediction" of peak field by adjusting the velocity profile. First, this would normally result in the front velocity's increasing markedly with height, which is considered unphysical. More importantly, it would almost always delay features of the predicted fine structure relative to those observed. Therefore the only practical way to adjust the amplitude of $E_c(t)$ is to adjust the amplitude factor in equation (5). In the case of stroke 8732/2, the parameters, $a_{\min 1}$ = 0.70, $a_{\min 2}$ = 0.60, $L_{a1}$ = 60 m, and $L_{a2}$ = 400 m, result in good agreement, as shown in Figure 7.

[31] The corresponding profile of $a(s)$ is given by the top curve in Figure 8. Notice that two height scales are usually required: a short one to bring the peak field into agreement with observation and a relatively long one to tailor the "tail" of the field change waveform. As mentioned above, nonuniform $a(s)$ results in a change in the linear charge density on the channel from before to after the return stroke's passage. This change, which we call the "deposited" charge density after *Thottappillil et al.* [1997], is proportional to $-\mathrm{d}a/\mathrm{d}s$ because the integral of $I(t_1, s)$ over time is independent of path length (see equations (5)−(8) and the discussion following), and is illustrated by the bottom curve of Figure 8. Notice that an appreciable fraction of the stroke charge is deposited quite close to the surface in this case. This turns out to be true generally in our data set and is interpreted further in a later section.

## 6. Fitting Variations and Problem Cases

### 6.1. Adjustment of $E_c(t)$ Peak Shape Using Velocity Profile

[32] Occasionally it was not possible to match the shape and/or amplitude of the $E_m(t)$ peak by adjusting $a(s)$ alone. In such cases the initial front velocity could often be increased, at the expense of introducing a second height scale for $v(s)$, to yield a larger and/or sharper $E_c(t)$ peak. Figures 9 and 10 show the best example of this type of velocity adjustment and its results for stroke 8732/1.

### 6.2. Consequences of the Limit, $v(s) \leq c$

[33] There is a physical limit on the TLM velocity: the current onset cannot propagate up the channel faster than the speed of light. As indicated above, we tried to prevent $v_{eff}(s)$ from increasing with height. This was not always possible, however, without violating the constraint on $v(s)$, especially when a rapid increase in current risetime with height and/or a relatively large $v_{eff}(s)$ was required. The most dramatic example of such behavior is stroke 8728/11, illustrated in Figure 11. Nevertheless, we were able to fit

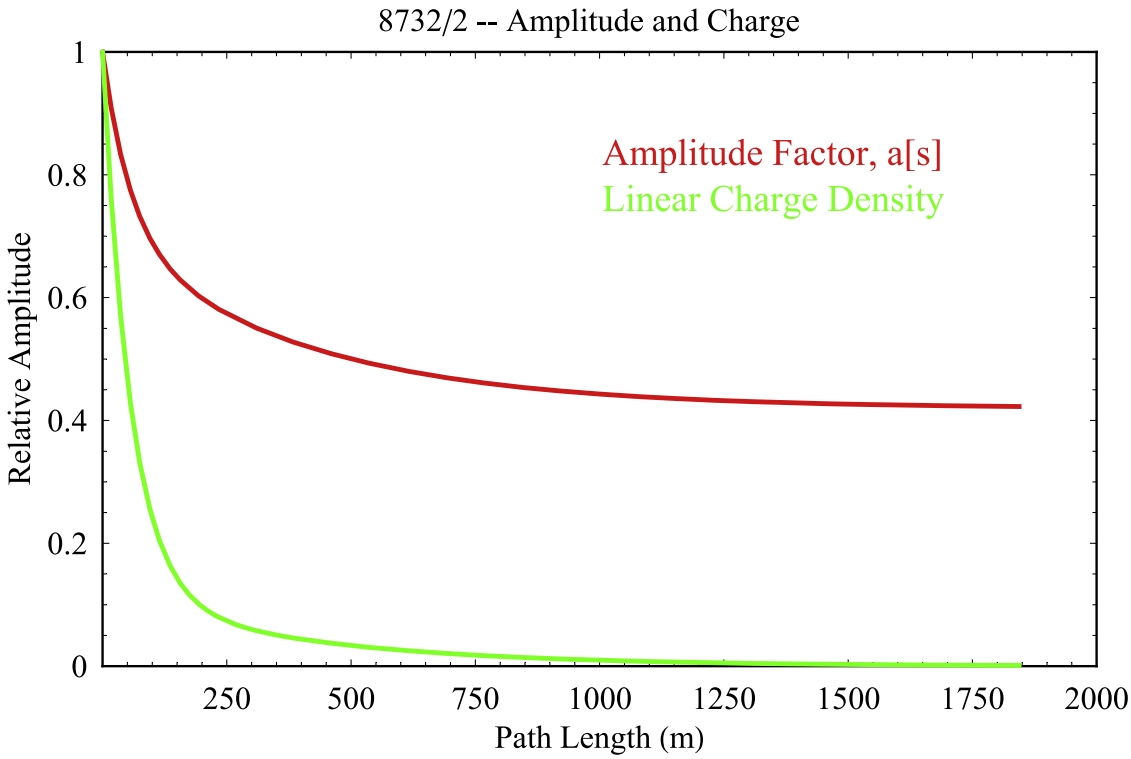


**Figure 8.** Profile of the amplitude factor ($a(s)$, top curve) and the corresponding relative profile of charge deposition on the channel by the model return stroke shown in Figure 7 (bottom curve).

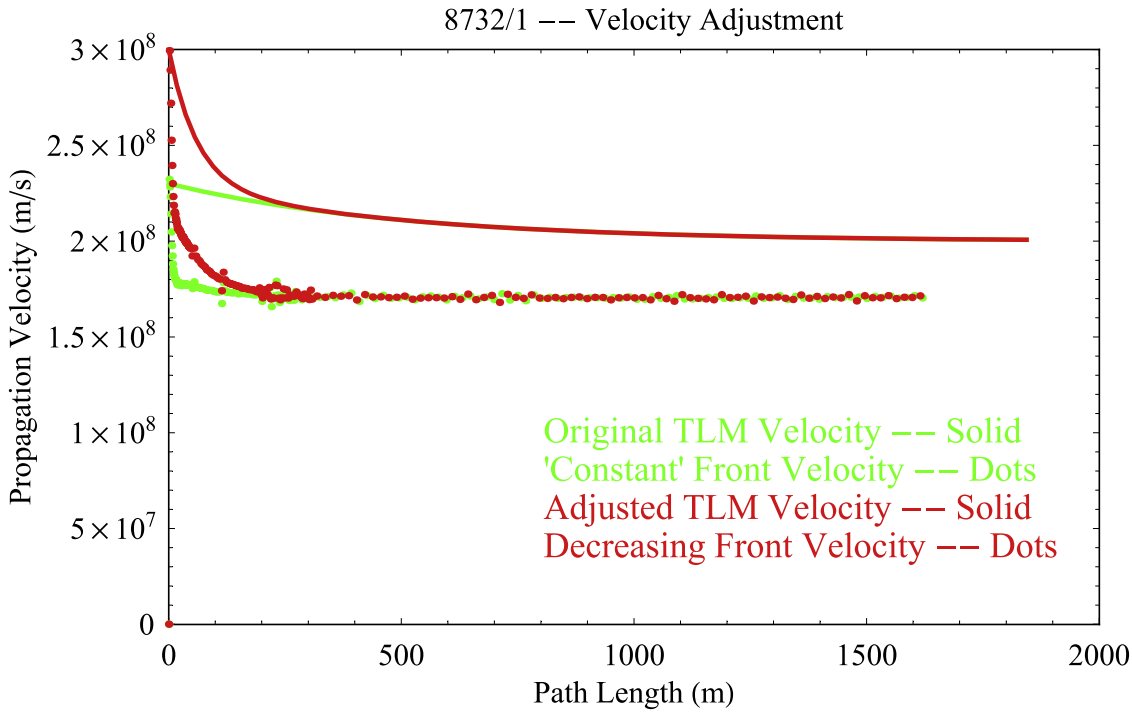


**Figure 9.** TLM and front velocity profiles, as in Figure 6, for stroke 8732/1, which required propagation speed adjustment, as well as amplitude adjustment, in order to match both the peak and the subsequent structure of $E_m(t)$. The solid green curve is for $v_{min} = 2.0 \times 10^8$ m/s, $v_{max} = 2.3 \times 10^8$, and $L_{v1} = 500$ m. The red curve adds the parameters, $v_{ampl} = 0.7 \times 10^8$ m/s and $L_{v2} = 60$ m.

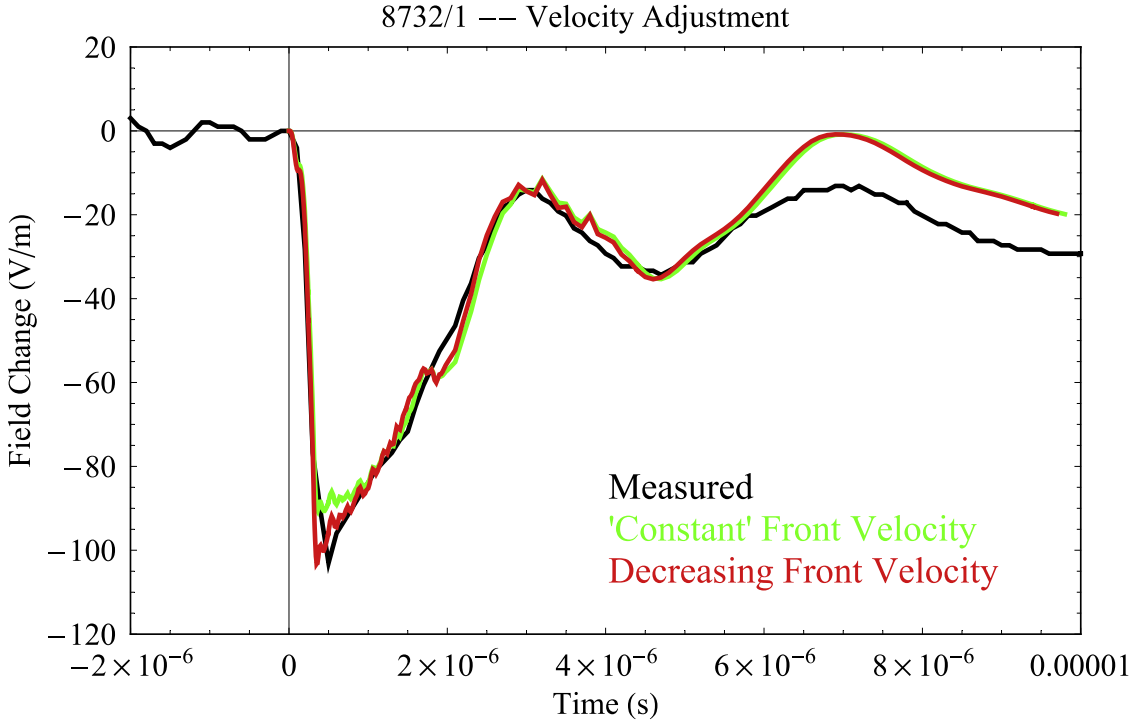


**Figure 10.** Computed field change waveforms (colors) corresponding to the velocity profiles in Figure 9 compared with observed field change (black).

$E_c(t)$ to $E_m(t)$ quite satisfactorily in this case, as can be seen in Figure 16a in section 7.

### 6.3. Extremely Fast Decay of Current Amplitude

[34] Several cases require both $a_{min1}$ significantly less than unity and $L_{a1} \leq 10$ m in order to obviate a sharp initial peak on $E_c(t)$. This implies that a significant fraction of the return stroke charge is deposited in the lowest ~10 m above the ground in these cases (although the need for a very rapid decrease in $a(s)$ will be examined further below). Stroke 8726/3, for which $a_{min1} = 0.69$ and the preferred value of $L_{a1} = 5$ m, is one of the

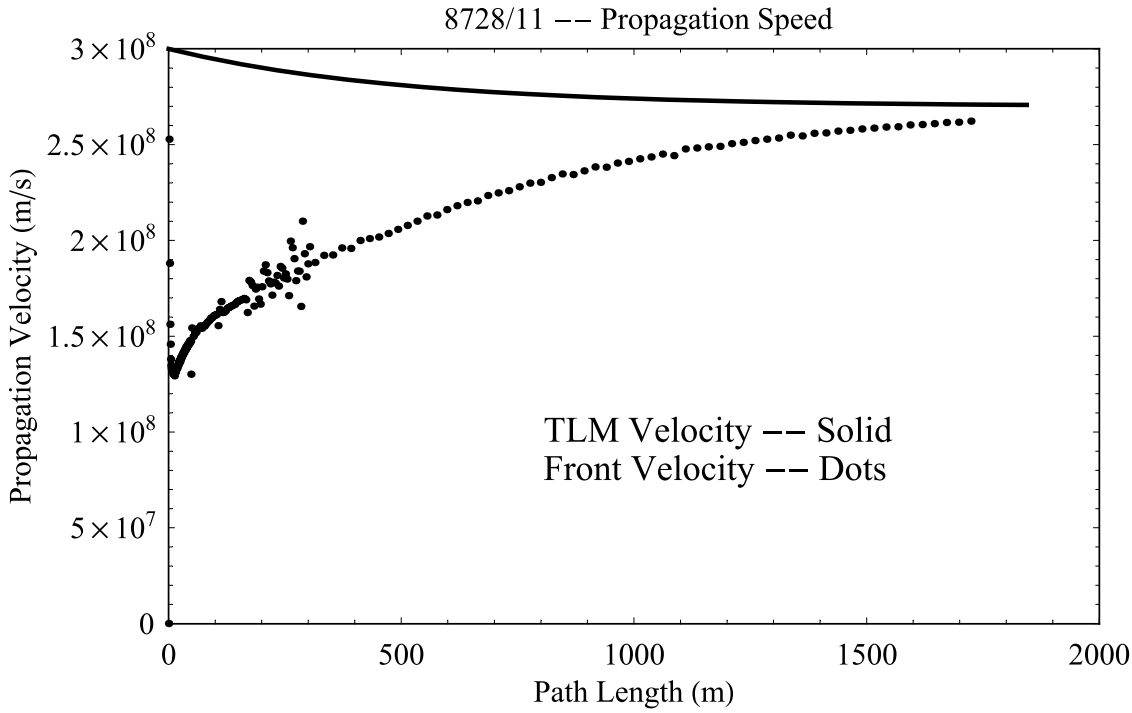


**Figure 11.** TLM velocity (solid) and front velocity (dots) profiles for stroke 8728/11. The parameters for the solid curve are $v_{min} = 2.7 \times 10^8$ m/s, $v_{max} = 3.0 \times 10^8$, and $L_{v1} = 500$ m.

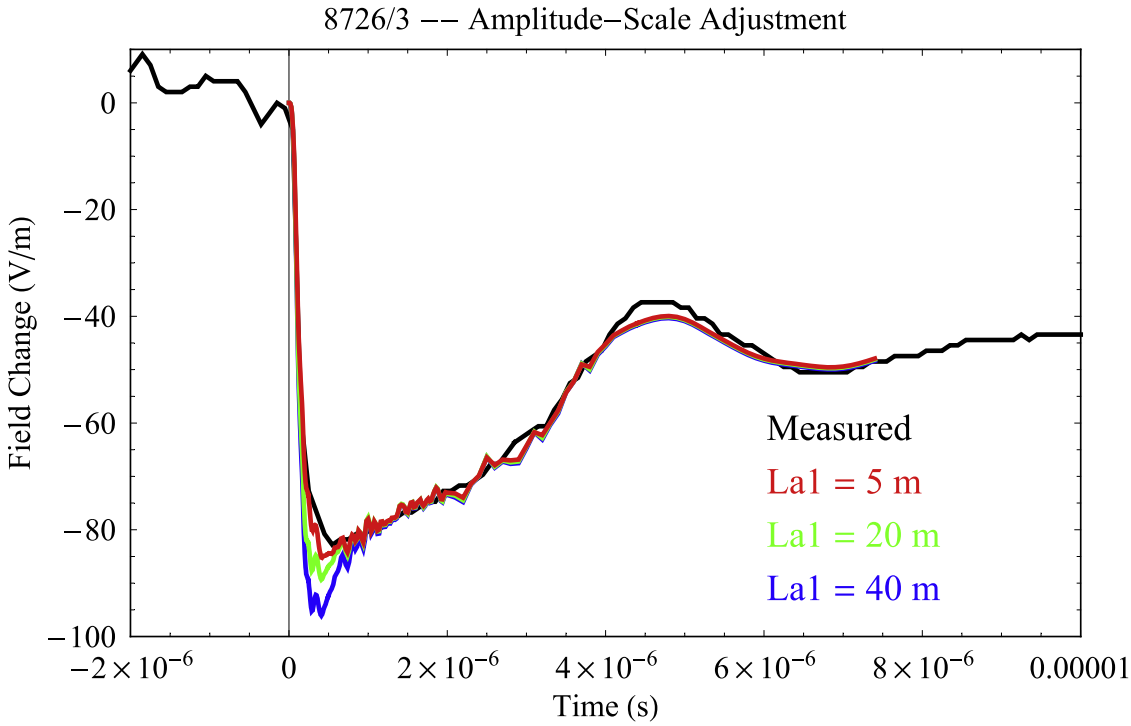


**Figure 12.** Effect of a very rapid amplitude factor decrease in a case with the parameters, $\tau_{max}$ = 1.16 $\mu$s, $L_\tau$ = 1851 m, $v_{min}$ = 2.3 × $10^8$ m/s, $v_{max}$ = 3.0 × $10^8$, $L_{v1}$ = 500 m, and as given in the caption of Figure 13.

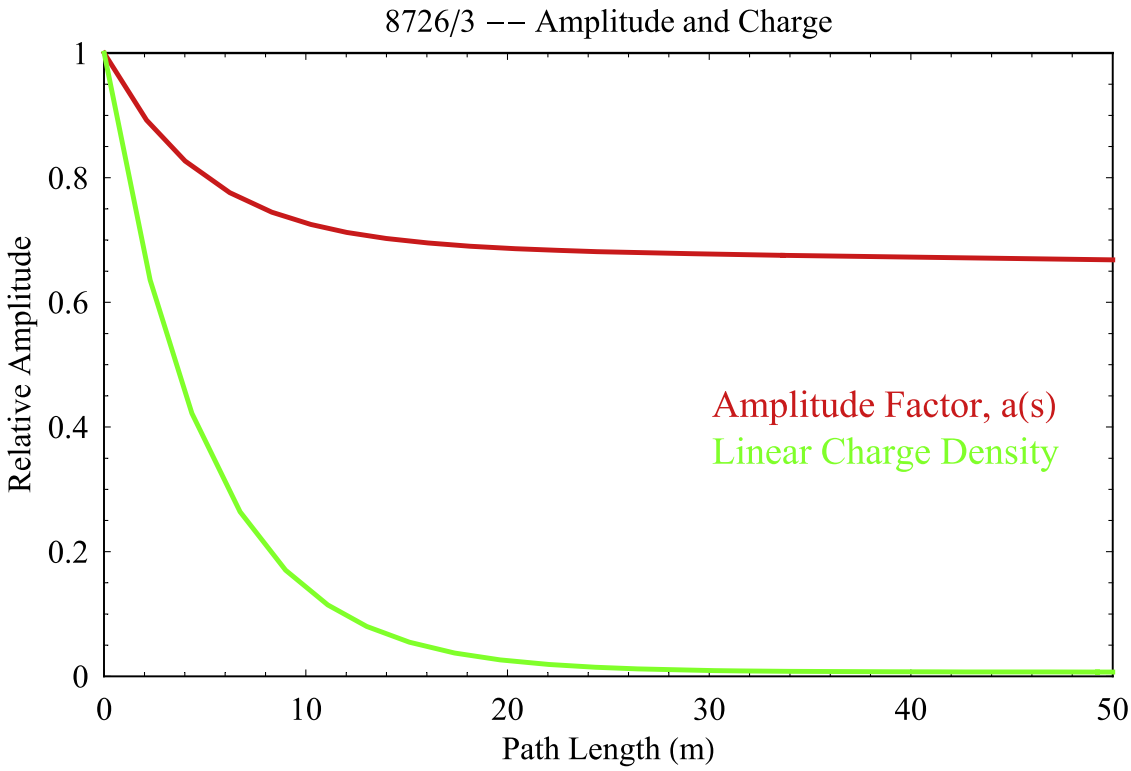


**Figure 13.** Similar to Figure 8 but shown on an expanded height scale for the parameters, $a_{min1}$ = 0.69, $L_{a1}$ = 5 m, $a_{min2}$ = 0.35, $L_{a2}$ = 1000 m, that correspond to the red curve in Figure 12.

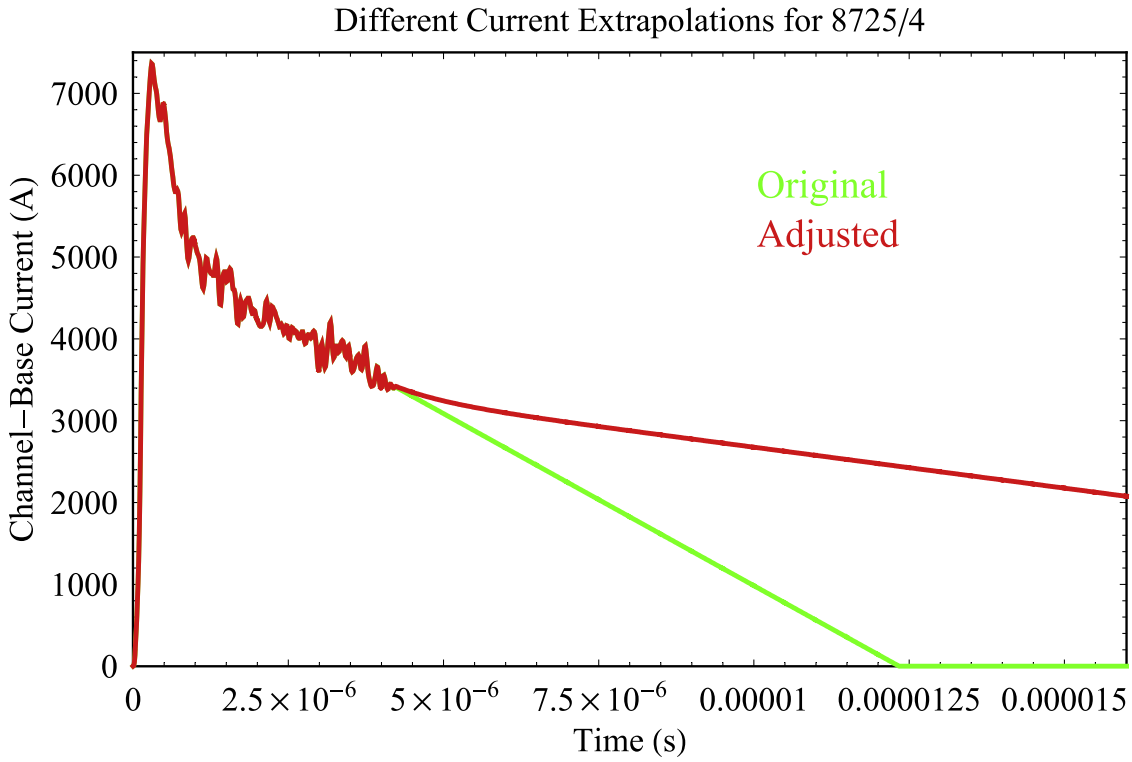


**Figure 14.** Two different current waveform extrapolations for stroke 8725/4.

most extreme cases in this regard. Figure 12 compares $E_c(t)$ for three different values of $L_{a1}$ with $E_m(t)$. Evidently the best agreement is for $L_{a1}$ = 5 m. Figure 13 shows the resulting profiles of $a(s)$ and linear charge density on an expanded height scale. A possible physical explanation of this and other similar results is offered in section 9 below.

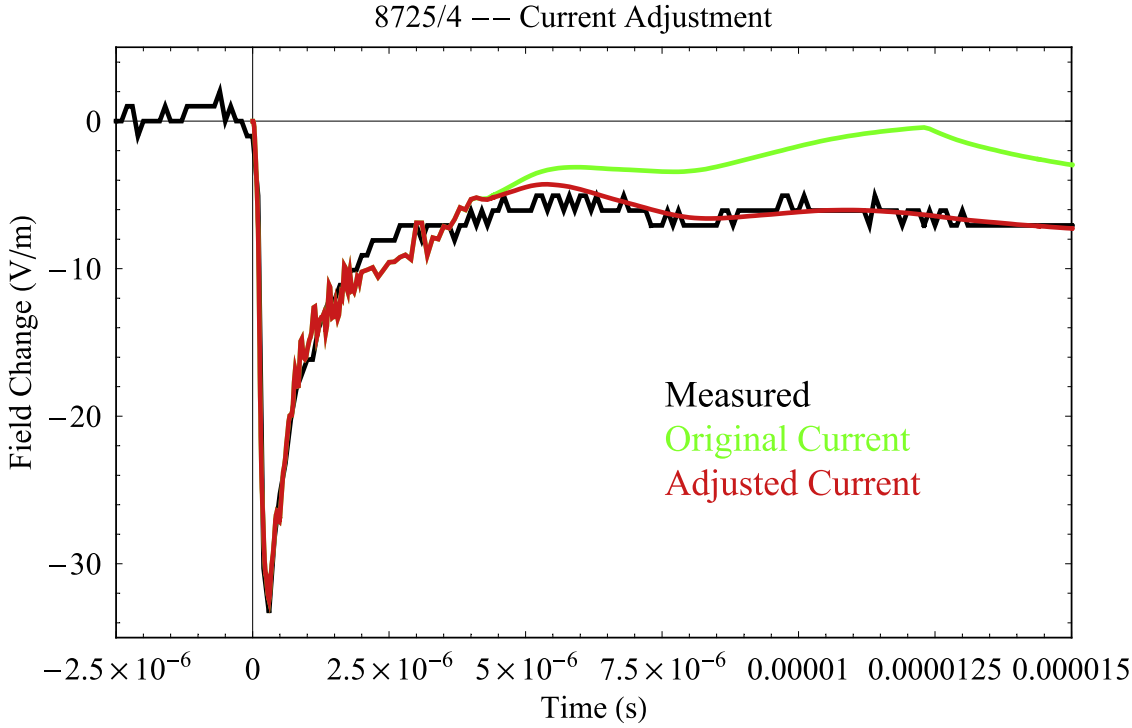


**Figure 15.** Model field change waveforms (green and red, corresponding to the similarly colored current waveforms in Figure 14) compared with the observed field change (black).

**Table 1.** Free Parameters in Current Model

| Event (Flash/Stroke) | Geometry | | Kernel Scale, $\tau(s)$ | | | TLM Velocity, $v(s)$ | | | | | | Amplitude Factor, $a(s)$ | | | | Onset at Channel Top, $\mu$s |
|---|---|---|---|---|---|---|---|---|---|---|---|---|---|---|---|---|
| | Wire Tip, m | Channel Top, m | $\tau_{max}$, $\mu$s | $L_\tau$, m | Initial Slope, $\mu$s/km | $v_{min}$, $10^8$ m/s | $v_{max}$, $10^8$ m/s | $L_{v1}$, m | $v_{ampl}$, $10^8$ m/s | $L_{v2}$, m | Constant Slope, m/s/m | $a_{min1}$ | $L_{a1}$, m | $a_{min2}$ | $L_{a2}$, m | |
| 8715/2 | 184 | 1240 | | | 0.817 | 2.50 | 3.00 | 150 | 0.00 | | | 0.65 | 100 | 1.00 | | 5.91 |
| 8715/3 | 184 | 1240 | | | 0.653 | 2.50 | 3.00 | 150 | 0.00 | | | 0.78 | 50 | 0.80 | 200 | 5.91 |
| 8715/4 | 184 | 1240 | | | 0.653 | 2.50 | 3.00 | 150 | 0.00 | | | 0.80 | 20 | 0.77 | 200 | 5.91 |
| 8715/6 | 184 | 1240 | | | 1.037 | 3.00 | | | 0.00 | | | 0.80 | 30 | 0.79 | 150 | 5.19 |
| 8715/7 | 184 | 1240 | | | 0.653 | 3.00 | | | 0.00 | | | 0.75 | 5 | 0.74 | 75 | 5.19 |
| 8715/8 | 184 | 1240 | | | 0.817 | 2.75 | 3.00 | 75 | 0.00 | | | 0.77 | 20 | 0.55 | 1000 | 5.55 |
| 8715/9 | 184 | 1240 | | | 0.817 | 3.00 | | | 0.00 | | | 0.59 | 35 | 1.00 | | 5.19 |
| 8715/10 | 184 | 1240 | | | 0.653 | 2.50 | 3.00 | 150 | 0.00 | | | 0.73 | 5 | 0.85 | 200 | 5.91 |
| 8717/3 | 269 | 2220 | | | 0.935 | 2.10 | 2.60 | 70 | 0.40 | 700 | | 0.45 | 130 | 1.00 | | 10.94 |
| 8717/5 | 269 | 2220 | | | 0.935 | 2.10 | 2.60 | 70 | 0.40 | 700 | | 0.55 | 130 | 1.00 | | 10.94 |
| 8725/1 | 370 | 1842 | 0.663 | 782 | 0.848 | 2.20 | 3.00 | 400 | 0.00 | | | 0.69 | 40 | 0.52 | 400 | 8.73 |
| 8725/2 | 370 | 1842 | 0.663 | 782 | 0.848 | 2.20 | 3.00 | 400 | 0.00 | | | 0.81 | 5 | 0.52 | 200 | 8.73 |
| 8725/3 | 370 | 1842 | 0.663 | 782 | 0.848 | 2.10 | 3.00 | 400 | 0.00 | | | 0.58 | 10 | 0.64 | 500 | 9.01 |
| 8725/4 | 370 | 1842 | 1.691 | 845 | 2.001 | 0.75 | 2.15 | 100 | 0.85 | 800 | | 0.50 | 150 | 1.00 | | 18.09 |
| 8725/5 | 370 | 1842 | | | 0.682 | 2.30 | 2.70 | 100 | 0.00 | | | 0.70 | 5 | 0.50 | 500 | 8.85 |
| 8726/1 | 552 | 1704 | | | 0.236 | | 3.00 | | | | −100000 | 0.46 | 10 | 0.90 | 300 | 8.97 |
| 8726/2 | 552 | 1704 | 1.160 | 1851 | 0.627 | 1.80 | 2.60 | 30 | 0.40 | 500 | | 0.80 | 30 | 0.50 | 400 | 9.48 |
| 8726/3 | 552 | 1704 | 1.160 | 1851 | 0.627 | 2.30 | 3.00 | 500 | 0.00 | | | 0.69 | 5 | 0.35 | 1000 | 7.43 |
| 8726/4 | 552 | 1704 | 1.160 | 1851 | 0.627 | 1.80 | 2.60 | 30 | 0.40 | 500 | | 0.80 | 30 | 0.50 | 400 | 9.46 |
| 8726/5 | 552 | 1704 | 1.160 | 1851 | 0.627 | 2.40 | 3.00 | 300 | 0.00 | | | 0.67 | 10 | 0.45 | 1000 | 7.40 |
| 8728/10 | 171 | 1754 | 0.792 | 814 | 0.973 | 2.70 | 3.00 | 500 | 0.00 | | | 0.68 | 70 | 0.65 | 500 | 8.13 |
| 8728/11 | 171 | 1754 | 0.727 | 531 | 1.369 | 2.70 | 3.00 | 500 | 0.00 | | | 0.75 | 100 | 0.50 | 400 | 8.13 |
| 8732/1 | 197 | 1844 | | | 0.458 | 2.00 | 2.70 | 60 | 0.30 | 500 | | 0.70 | 80 | 0.64 | 300 | 9.75 |
| 8732/2 | 197 | 1844 | 4.360 | 7084 | 0.615 | 2.10 | 2.60 | 500 | 0.00 | | | 0.70 | 60 | 0.60 | 400 | 9.22 |

**Table 2.** Representative Values of Current Behavior

| Event (Flash/Stroke) | 10–90% Risetime of Current | | | | | | Front Velocity, $v_{eff}(s)$ | | | | | Amplitude Factor, $a(s)$ | | | | |
|---|---|---|---|---|---|---|---|---|---|---|---|---|---|---|---|---|
| | Surface, $\mu$s | 10 m, $\mu$s | 30 m, $\mu$s | 100 m, $\mu$s | 300 m, $\mu$s | 1000 m, $\mu$s | Average, $10^8$ m/s | 10 m, $10^8$ m/s | 100 m, $10^8$ m/s | 300 m, $10^8$ m/s | 1000 m, $10^8$ m/s | 10 m | 30 m | 100 m | 300 m | 1000 m |
| 8715/2 | 0.296 | 0.300 | 0.327 | 0.470 | 0.951 | 2.50 | 1.72 | 1.60 | 1.70 | 1.72 | 1.75 | 0.97 | 0.91 | 0.78 | 0.67 | 0.65 |
| 8715/3 | 0.179 | 0.180 | 0.196 | 0.329 | 0.764 | 1.99 | 1.85 | 1.90 | 1.85 | 1.82 | 1.85 | 0.95 | 0.88 | 0.75 | 0.66 | 0.63 |
| 8715/4 | 0.189 | 0.191 | 0.215 | 0.344 | 0.729 | 2.17 | 1.84 | 1.88 | 1.83 | 1.83 | 1.82 | 0.91 | 0.82 | 0.73 | 0.66 | 0.62 |
| 8715/6 | 0.175 | 0.183 | 0.228 | 0.436 | 1.050 | 3.39 | 1.74 | 1.52 | 1.70 | 1.75 | | 0.93 | 0.84 | 0.72 | 0.65 | 0.63 |
| 8715/7 | 0.186 | 0.190 | 0.213 | 0.353 | 0.759 | 2.22 | 2.04 | 1.90 | 1.93 | 2.05 | 2.08 | 0.76 | 0.69 | 0.61 | 0.56 | 0.56 |
| 8715/8 | 0.191 | 0.193 | 0.215 | 0.360 | 0.794 | 2.58 | 1.84 | 1.70 | 1.78 | 1.83 | 1.86 | 0.91 | 0.81 | 0.74 | 0.68 | 0.55 |
| 8715/9 | 0.356 | 0.358 | 0.375 | 0.501 | 0.991 | 2.81 | 1.87 | 1.68 | 1.75 | 1.87 | | 0.90 | 0.76 | 0.61 | 0.59 | 0.59 |
| 8715/10 | 0.270 | 0.268 | 0.275 | 0.375 | 0.757 | 2.12 | 1.84 | 1.88 | 1.82 | 1.83 | 1.84 | 0.76 | 0.72 | 0.69 | 0.64 | 0.62 |
| 8717/3 | 0.138 | 0.136 | 0.163 | 0.377 | 0.898 | 2.57 | 1.60 | 1.70 | 1.61 | 1.60 | 1.58 | 0.96 | 0.89 | 0.70 | 0.50 | 0.45 |
| 8717/5 | 0.111 | 0.116 | 0.152 | 0.335 | 0.854 | 2.57 | 1.60 | 1.65 | 1.65 | 1.62 | 1.55 | 0.97 | 0.91 | 0.76 | 0.59 | 0.55 |
| 8725/1 | 0.553 | 0.544 | 0.536 | 0.609 | 0.964 | 1.83 | 1.95 | 1.70 | 1.74 | 1.86 | 2.02 | 0.92 | 0.81 | 0.64 | 0.52 | 0.39 |
| 8725/2 | 0.433 | 0.432 | 0.437 | 0.550 | 0.969 | 1.76 | 1.95 | 1.63 | 1.72 | 1.83 | 2.00 | 0.82 | 0.76 | 0.66 | 0.51 | 0.42 |
| 8725/3 | 0.355 | 0.357 | 0.369 | 0.481 | 0.879 | 1.80 | 1.90 | 1.68 | 1.74 | 1.83 | 1.93 | 0.73 | 0.59 | 0.54 | 0.49 | 0.40 |
| 8725/4 | 0.162 | 0.171 | 0.249 | 0.541 | 1.400 | 3.09 | 0.93 | 1.11 | 1.20 | 1.01 | 0.90 | 0.97 | 0.92 | 0.75 | 0.45 | 0.45 |
| 8725/5 | 0.159 | 0.161 | 0.175 | 0.297 | 0.700 | 2.02 | 1.74 | 1.70 | 1.71 | 1.71 | 1.73 | 0.73 | 0.68 | 0.64 | 0.54 | 0.40 |
| 8726/1 | 0.888 | 0.875 | 0.871 | 0.871 | 0.944 | 1.54 | 1.84 | 2.76 | 2.36 | 2.21 | 1.76 | 0.66 | 0.48 | 0.45 | 0.43 | 0.42 |
| 8726/2 | 0.491 | 0.494 | 0.514 | 0.586 | 0.831 | 1.71 | 1.62 | 1.83 | 1.62 | 1.61 | 1.61 | 0.93 | 0.84 | 0.72 | 0.59 | 0.43 |
| 8726/3 | 0.269 | 0.266 | 0.268 | 0.358 | 0.720 | 1.91 | 1.96 | 1.90 | 1.92 | 1.97 | 1.97 | 0.73 | 0.68 | 0.65 | 0.57 | 0.41 |
| 8726/4 | 0.339 | 0.340 | 0.349 | 0.421 | 0.705 | 1.61 | 1.62 | 1.88 | 1.62 | 1.60 | 1.60 | 0.93 | 0.84 | 0.72 | 0.59 | 0.43 |
| 8726/5 | 0.323 | 0.322 | 0.316 | 0.412 | 0.828 | 2.09 | 1.93 | 1.90 | 1.91 | 1.90 | 1.95 | 0.79 | 0.68 | 0.63 | 0.57 | 0.44 |
| 8728/10 | 0.400 | 0.402 | 0.416 | 0.579 | 1.050 | 2.23 | 2.14 | 1.55 | 1.70 | 1.88 | 2.28 | 0.95 | 0.87 | 0.71 | 0.58 | 0.47 |
| 8728/11 | 0.216 | 0.223 | 0.273 | 0.522 | 1.120 | 2.15 | 2.18 | 1.30 | 1.60 | 1.87 | 2.41 | 0.96 | 0.90 | 0.75 | 0.56 | 0.41 |
| 8732/1 | 0.410 | 0.410 | 0.416 | 0.448 | 0.682 | 1.57 | 1.72 | 2.17 | 1.80 | 1.70 | 1.70 | 0.95 | 0.88 | 0.71 | 0.55 | 0.46 |
| 8732/2 | 0.408 | 0.408 | 0.413 | 0.494 | 0.870 | 2.09 | 1.71 | 1.70 | 1.71 | 1.72 | 1.71 | 0.94 | 0.86 | 0.69 | 0.55 | 0.44 |

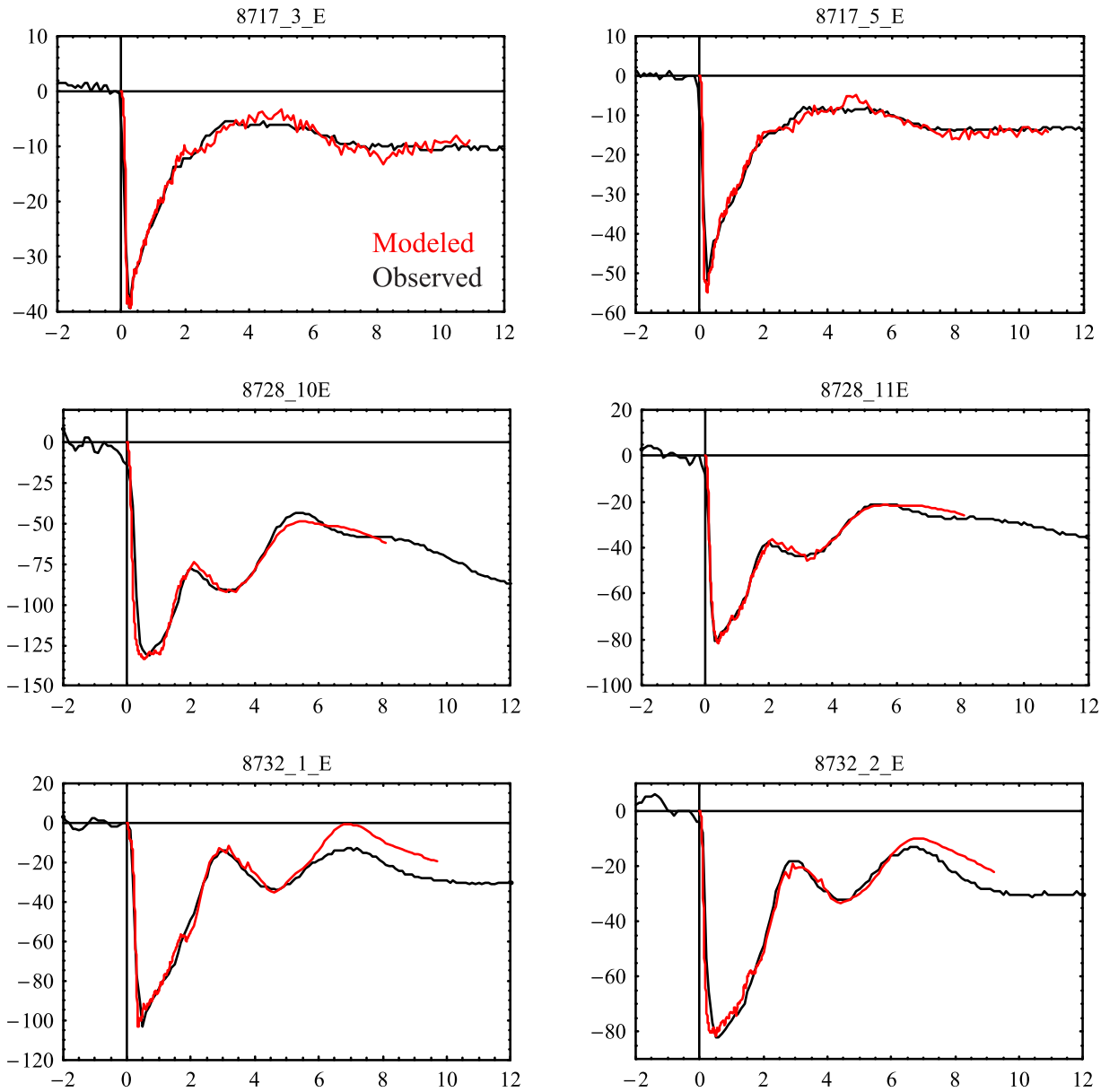


**Figure 16a.** Observed (black) and modeled (red) field change waveforms for all 24 return strokes in our data set. The scales are field change in V/m versus time in $\mu$s throughout. Note that the timescale is always 14 $\mu$s, whereas the field change scale depends on the magnitude of the stroke. This figure collects the events from three flashes for which we could analyze only two strokes each.

### 6.4. Probable Failure of Current Extrapolation

[35] In a few cases it appears impossible to get a good fit to the latter part of $E_m(t)$. We have already seen an example in stroke 8732/1 (Figure 10), where the amplitude of $E_c(t)$ becomes too small after the first 6 $\mu$s. Since the current for this stroke (see Figure 17a in section 7) was extrapolated from a linear fit to less than 3 $\mu$s of fairly steeply falling data following the peak, it seems probable that this phenomenon is caused by poor extrapolation. A more extreme example of this behavior is stoke 8725/4. The green waveform in Figure 14 shows the original current extrapolation for this case (simply our standard constant-plus-linear-plus-exponential fit to some 3.8 $\mu$s of descending current record), which falls to zero about 12 $\mu$s after onset. The resulting modeled field change is shown in green in Figure 15 and is seen to disagree with observation after the first 5 $\mu$s or so. If we arbitrarily force the current extrapolation to remain high, however (red curve in Figure 14), the resulting $E_c(t)$ (red curve in Figure 15, all fitting parameters remaining the same) agrees much better with $E_m(t)$. (This is the only case in which we have "tinkered" with the current extrapolation in order to obtain a better fit to the observed field change.)

[36] (Neglecting the high-frequency noise from the current waveform, notice that there is still too much fine structure in $E_c(t)$, relative to $E_m(t)$, during the first 5 $\mu$s of stroke 8725/4. We could not further increase the current risetime during the early part of this stroke while maintain-

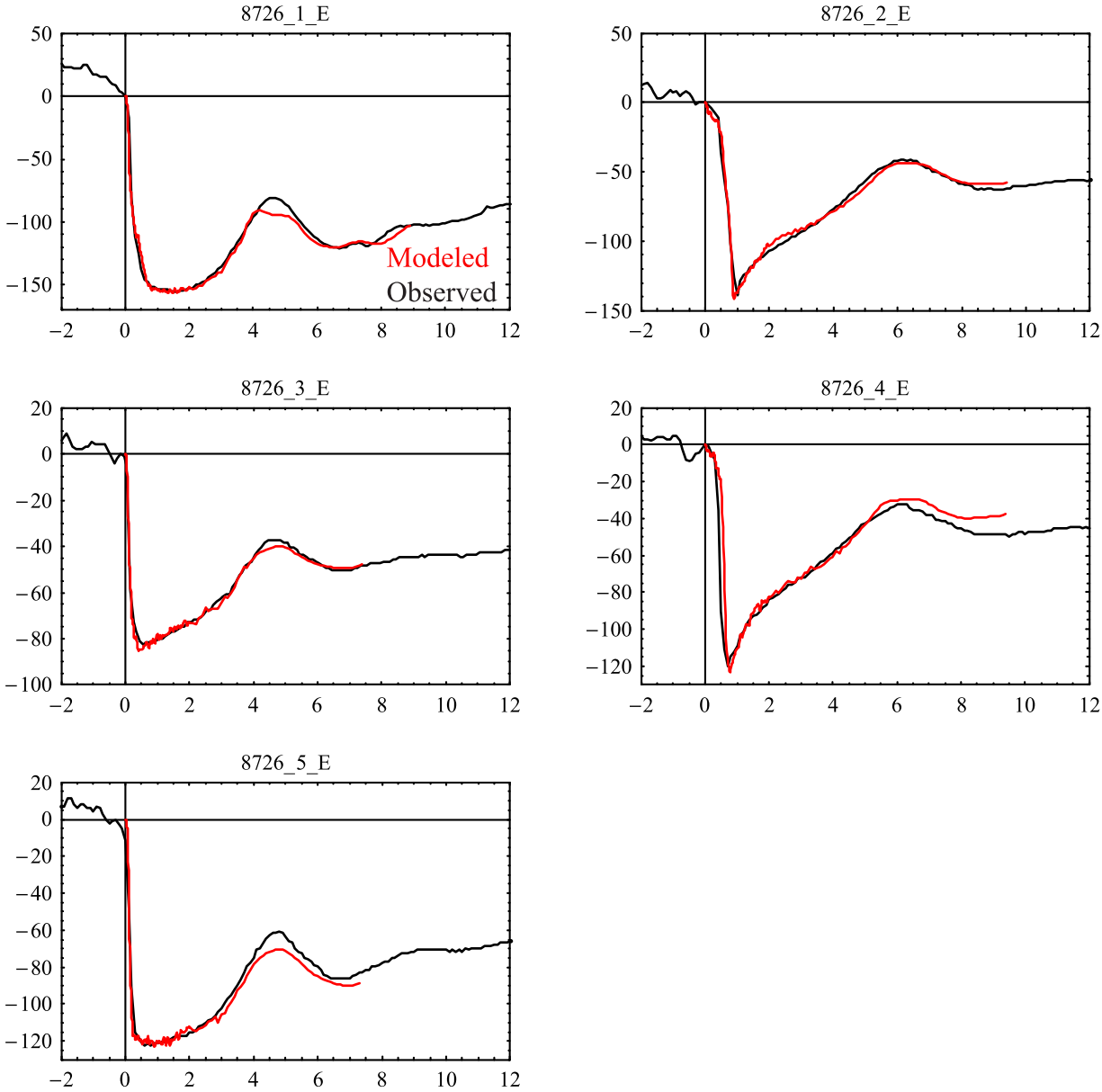


**Figure 16b.** Similar to Figure 16a but this figure shows several strokes from a single flash.

ing the observed peak field change without violating the constraint that $v(s) \leq c$. Such a rapid increase of $\tau(s)$ near channel base would significantly reduce $v_{eff}(s)$ there and, consequently, limit $E_c(t)$.)

## 7. Summary of Results for All 24 Strokes

[37] Table 1 gives values of the 11 free parameters in equations (9)–(11) for each stroke in our data set. A few explanatory remarks are in order here. The "Geometry" values in columns 2 and 3 indicate the path length from the surface to the tip of the triggering wire and to the top of the reconstructed channel, respectively. "Initial Slope" (column 6) is the only parameter quoted for the kernel timescale, $\tau(s)$, in cases where $L_\tau$ is much longer than the reconstructed channel, so that the profile of $\tau(s)$ is effectively linear. Values are omitted for unused parameters in $v(s)$ and $a(s)$. Instead of the exponential form specified in equation (10), a linear decrease of $v(s)$ from an initial value of $c$ appeared to be more appropriate for stroke 8726/1, as indicated in column 12. The last column of Table 1 gives the retarded time at which the onset of the current waveform arrives at the top of the reconstructed channel: the latest observer time, $t$, at which $E_c(t)$ can be computed.

[38] Table 2 gives the corresponding values of 10–90% current risetime, effective front velocity, $v_{eff}(s)$, and amplitude factor, $a(s)$, at representative path lengths along the channel in each case. It is these values that should be considered the results of our matching of $E_c(t)$ to $E_m(t)$, whereas the parameters in Table 1 are dependent on the specific form that is assumed for the current (equations (7)–(11)). (Recall that the amplitude factor in equation (5) determines the total charge passing a given point on the channel.) Note that the average of $v_{eff}(s)$ over the entire

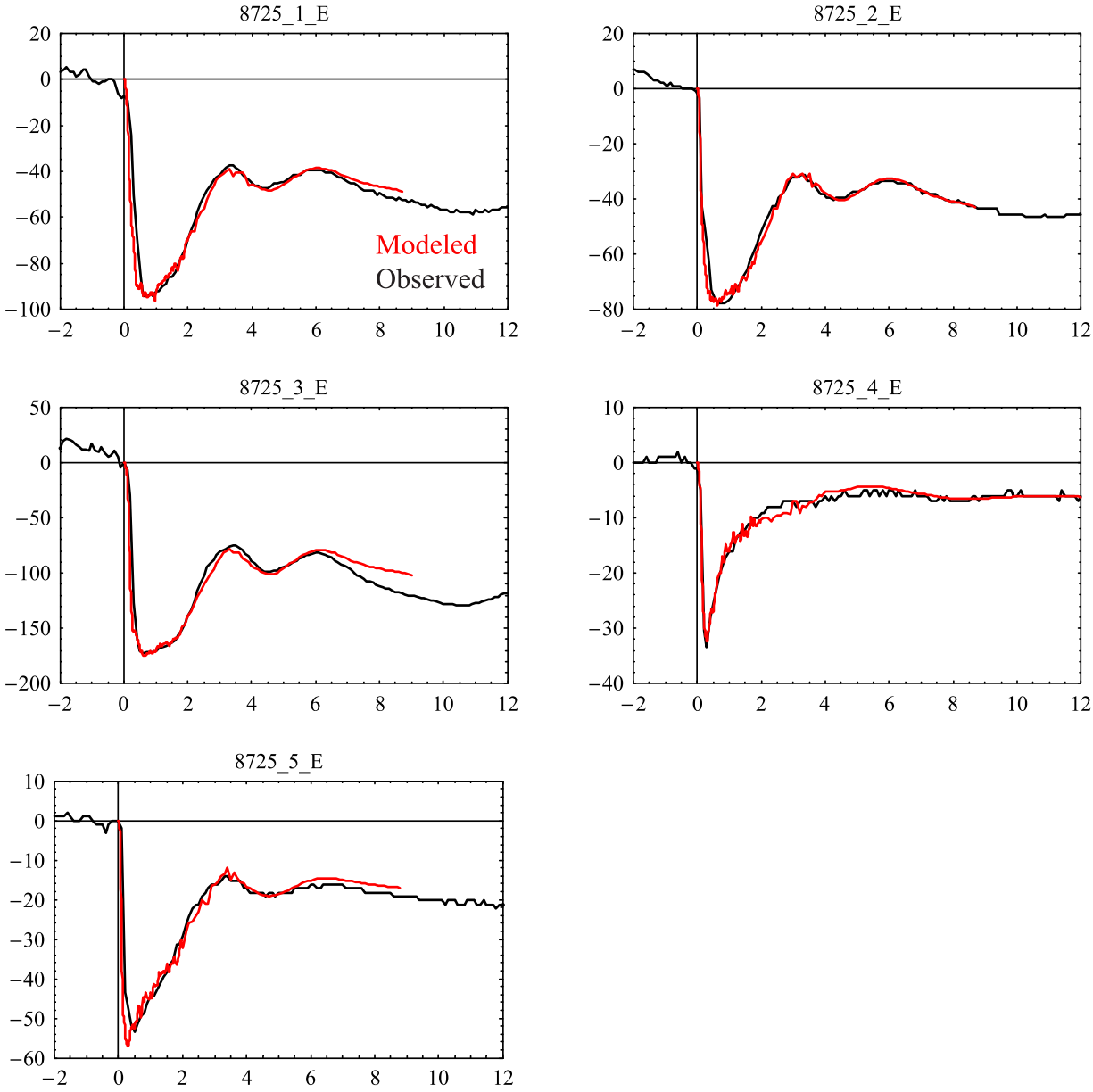


**Figure 16c.** Similar to Figure 16b.

current propagation interval (maximum path length reached by the half-amplitude point on the current waveform divided by the actual (not retarded) arrival time of current onset at the channel top) is given in column 8, and that values of $v_{eff}$(1000 m) are omitted from column 12 for the few strokes in which this half-amplitude point never reached $s$ = 1000 m.

[39] Figure 16 compares $E_c(t)$ and $E_m(t)$ for all 24 strokes. The pairs of strokes from three different flashes in Figure 16a make a familiar point: The field change waveforms that are produced by strokes within the same flash tend to be more similar than those from different flashes [e.g., *Le Vine and Willett*, 1995]. This is not always the case, however, as illustrated by Figure 16b, in which a single flash is seen to produce two qualitatively different classes of waveforms. Another example, in which two sharply peaked, relatively simple waveforms coexist with three having more rounded peaks and more pronounced fine structure, is shown in Figure 16c. The remaining eight strokes, all from the same flash, are shown in Figure 16d. Notice that we have been able to obtain good agreement in both fine structure and absolute amplitude between modeled and observed field changes over a wide variety of waveshapes. The corresponding extrapolated waveforms of channel base current are given in Figure 17.

## 8. Relative Light Intensity From Streak Photographs

[40] In addition to providing direct measurements of vertically averaged, two-dimensional, return stroke propagation speed [see *Willett et al.*, 1989a], the streak photographs of 14 of the 24 strokes in five of our six reconstructed lightning channels were processed to deter-

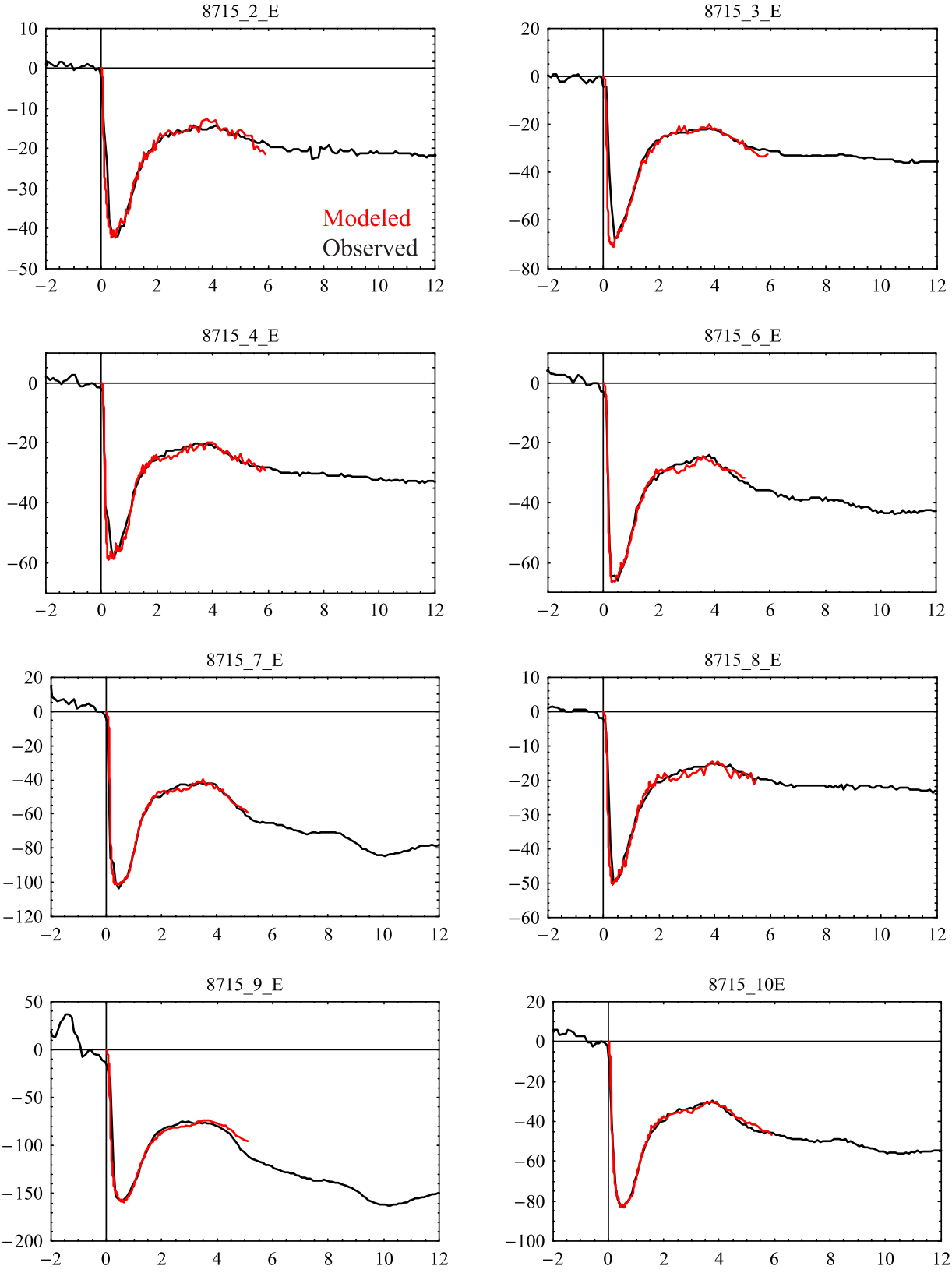


**Figure 16d.** Similar to Figure 16b.

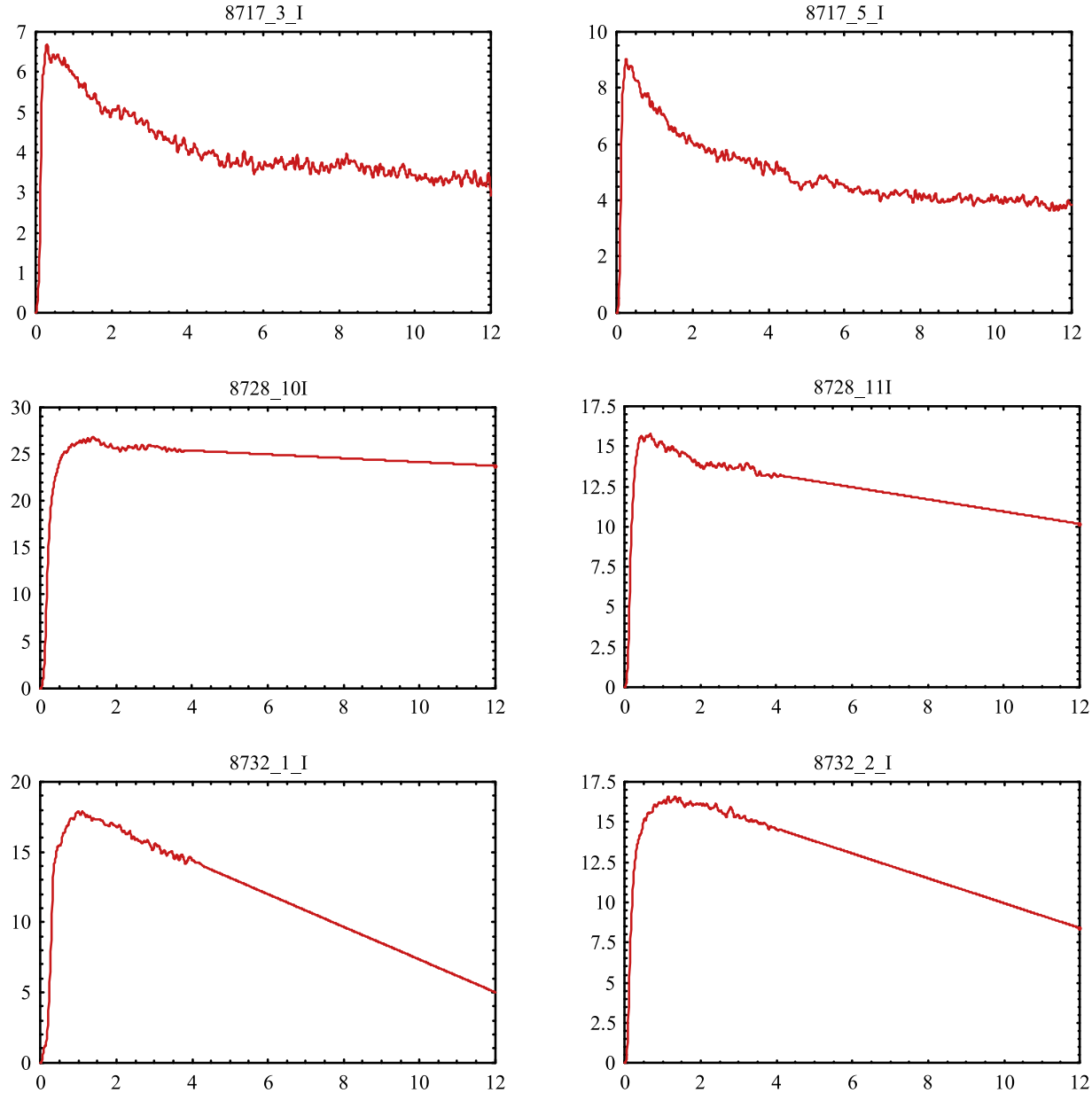


**Figure 17a.** Measured and extrapolated current waveforms. The scales are current in kA versus time in $\mu$s throughout. Note that the timescale is always 12 $\mu$s, whereas the current scale depends on the magnitude of the stroke. The current waveforms in this figure correspond to the field change waveforms of Figure 16a.

mine relative light intensity (RLI) as a function of time and position. A typical leader/return stroke image from our data set is shown in Figure 18. Such images were digitized, calibrated, and converted to time series of RLI at selected vertical levels. The resulting time series were then smoothed and analyzed to determine both peak amplitude and 10–90% risetime of the return strokes, for comparison with similar parameters deduced above for the corresponding current waveforms (see Table 2). This optical analysis is described in detail in Appendix C, and the results are presented in Table 3. Although we do not attempt to infer current amplitudes or risetimes from the optical parameters tabulated here, for the reasons explained in section 1, such a comparison is reasonable in view of the approximately linear relation that we found between RLI amplitude and peak current over our 14 strokes (like that reported by *Idone and Orville* [1985]) and the similarly linear relation between instantaneous RLI and current during the fast rising portions of four triggered strokes that was reported by *Wang et al.* [2005].

[41] The reconstructed height above ground and the path length along the lightning channel are shown in Table 3 for each measurement level on each streak photograph. (For comparison with the model results in Table 2, the path length must be used.) As detailed in Appendix C, the stroke RLI amplitude is the difference between the upper and lower limits of the fast rising portion of the corresponding time series. At levels above the first, the lower limit, or

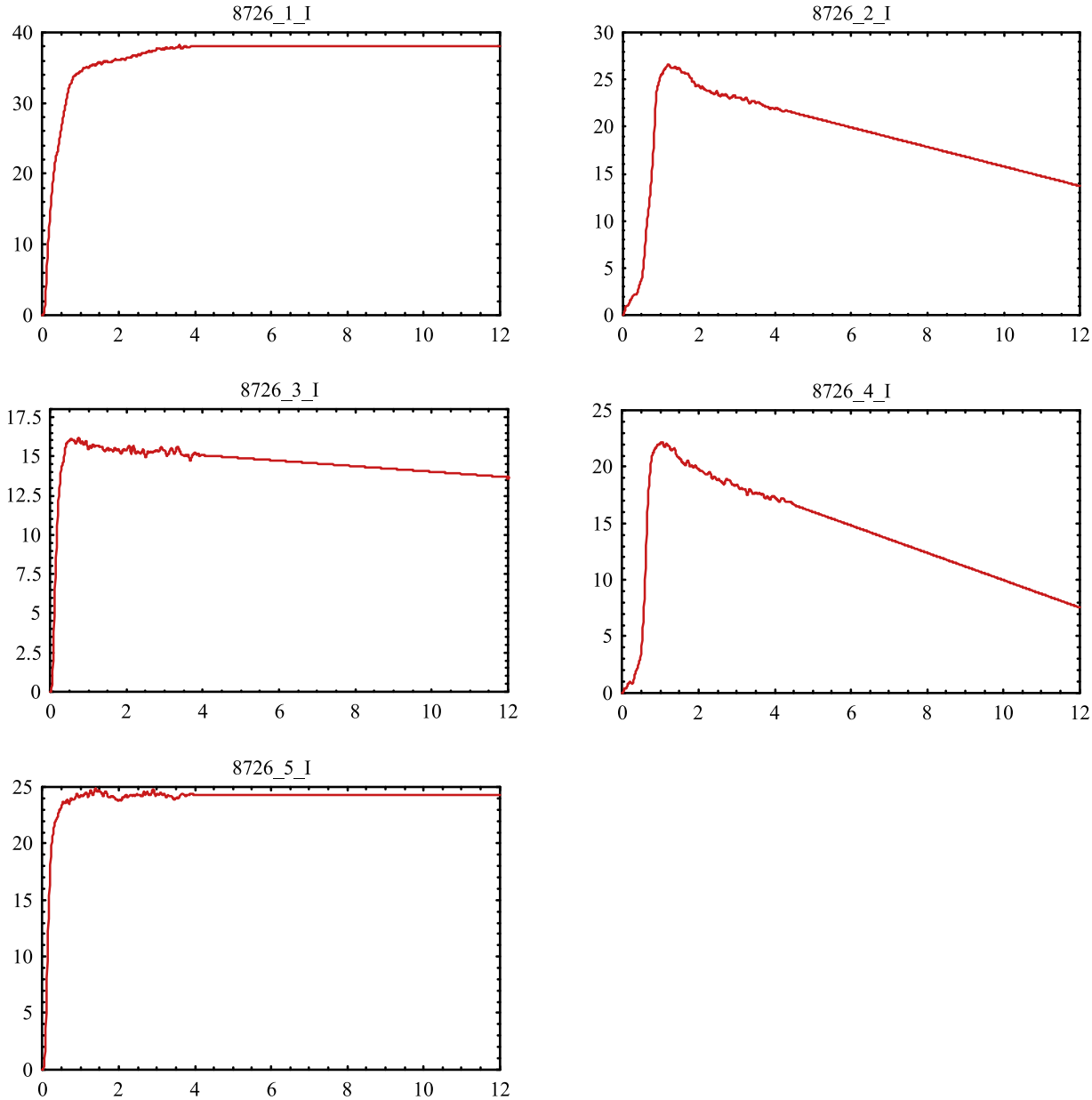


**Figure 17b.** Similar to Figure 17a but corresponding to the waveforms in Figure 16b.

"baseline" (also tabulated), can be viewed as an estimate of the residual brightness of the leader channel, just before stroke onset, since the zero of RLI was determined from the "background" film density prior to leader onset. The uncertainty in RLI amplitude is estimated at about ±0.1, on the basis of the typical noise level illustrated in Figure C1. The uncertainty in risetime is more difficult to estimate, depending as it does on the clarity with which the fast rising portion is manifest in the RLI waveforms. The error estimates in the last column of Table 3 are based on the scatter among multiple estimates of risetime, where such existed, as described with respect to Figure C2. The worst of these uncertainties are about ±23%, although most are much smaller.

[42] The optical parameters in Table 3 have been plotted against the corresponding electrical estimates in Figures 19a and 19b. Recall that the model peak current, $i_p(s)$, is not identical to the amplitude factor, $a(s)$, given in Tables 1 and 2. $i_p(s)$ is determined by both $a(s)$ (see equations (5) and (9)) and the convolution smoothing (see equations (7), (8), and (11)), which increases with path length as specified in Table 1. Therefore $i_p(s)$ has been computed and given in Table 4. (The values for zero path length are, of course, those directly measured at the surface.)

## 9. Discussion

[43] The entire procedure of adjusting the current model parameters in order to match the computed $E_c(t)$ waveform to the measured $E_m(t)$ has been illustrated in previous sections. Not only is this procedure somewhat subjective, but the various parameters interact with one another to a greater or lesser extent. We have already seen how the

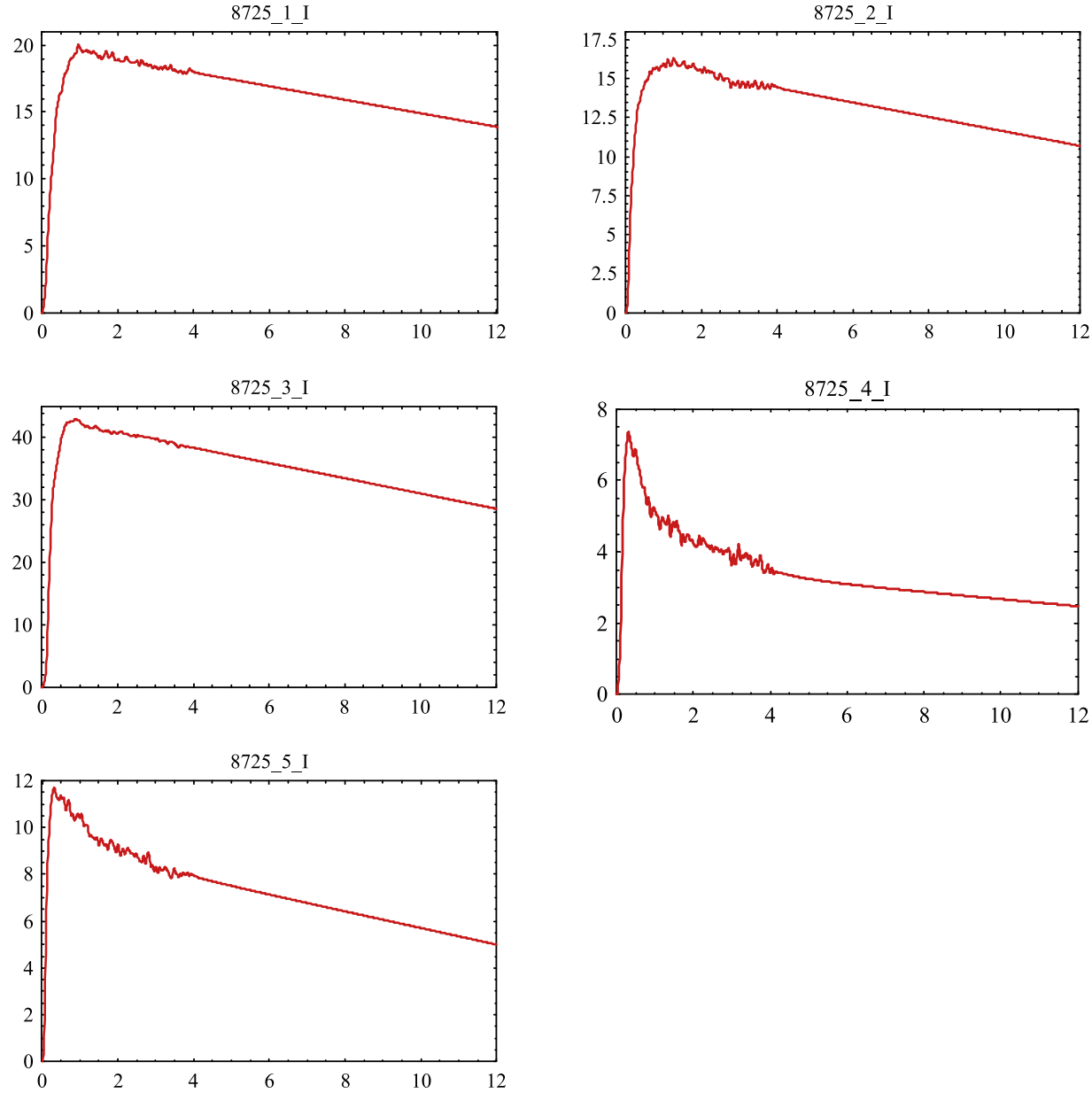


**Figure 17c.** Similar to Figure 17a but corresponding to Figure 16c.

introduction of a current risetime that increases with height, through $\tau(s)$ in equation (8), causes the effective front propagation speed, $v_{eff}(s)$, to decrease relative to $v(s)$, although this particular interaction does not cause any ambiguities beyond an occasional encounter with the physical limitation, $v(s) \leq c$. It has also been pointed out that the amplitude of $E_c$ is directly proportional to $v_{eff}$, so that speed changes affect the inferred amplitude factor, $a(s)$. Again, this causes no serious difficulties, since both the risetime and the effective speed of the current waveform are strongly tied to observed features of $E_m(t)$.

[44] The amplitude factor, in turn, affects not only the overall amplitude of $E_c$ but also the amplitude of its fine structure. (Compare the "TLM Decreasing" (red) curve in Figure 5 with the simulation (red curve) in Figure 7.) Nevertheless, one cannot normally trade off (for example) increased $a(s)$ against increased $\tau(s)$, maintaining the same level of fine structure, because this would make the overall amplitude of $E_c$ too large. A significant concern arises, however, when the extrapolation of the measured current waveform to later times is uncertain, as illustrated in Figure 14 for stroke 8725/4. In such cases it would be possible to trade off (for example) a higher current extrapolation against decreased $a(s)$ (maintaining the same overall amplitude of $E_c$ but reducing the fine structure) and decreased $\tau(s)$ (boosting the fine structure back to the correct level but yielding different inferred current risetime versus height).

[45] This last ambiguity exists to some extent in all 14 strokes having short current records (flashes 8725, 8726, 8728, and 8732), although examination of the measured current and/or computed field change waveforms in Figures 16 and 17 suggests that it might be a significant problem in

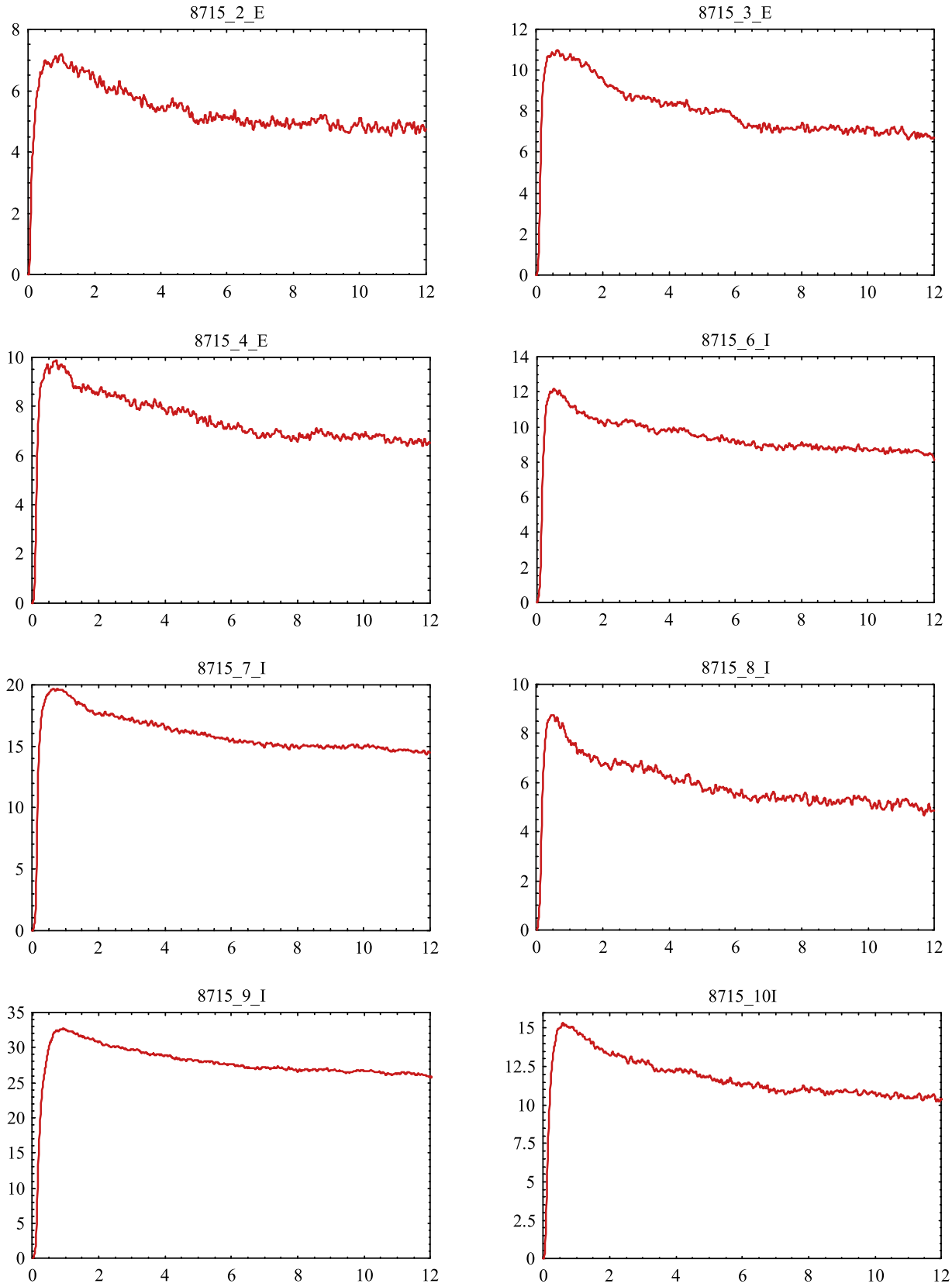


**Figure 17d.** Similar to Figure 17a but corresponding to Figure 16d.

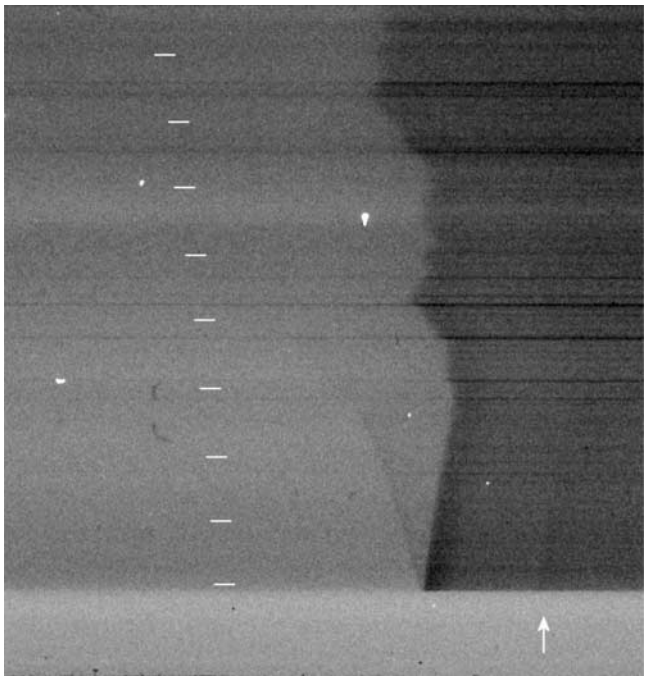

**Figure 18.** A typical streak image of leader/return stroke sequence for stroke 8725/1 as rendered by the Xillix camera. The analysis levels chosen for this event are illustrated by white horizontal bars. The vertical separation between level one (the lowest) and level nine (the highest) in this image corresponds to about 980 m at the range of the lightning channel. The horizontal extent of the image corresponds to about 125 $\mu$s of time. See Appendix C for further details.

only 8 (strokes 8725/2, 8725/3, 8725/4, 8725/5, 8726/1, 8726/4, 8732/1, and 8732/2). Since we have no way of assessing the accuracy of the extrapolated currents at late times in these cases, we cannot accurately evaluate the true uncertainties in the inferred risetime or amplitude of the current at those late times. (This is also why we have refrained from tinkering with the extrapolated currents in all cases except 8725/4.) The potential uncertainties in these parameters, primarily at the higher altitudes, due to the extrapolation of measured current waveforms are therefore ignored in the following discussion.

### 9.1. Risetime of Current

[46] The rapid increase in current risetime with increasing path length, illustrated in Figure 2 for example, is the most robust and inescapable conclusion of the present analysis. We could find no alternative to spreading out the fast rising current front, at least within the framework of our generalized transmission line model, to obviate the excessive high-frequency radiation that would otherwise result from the observed channel tortuosity. The first few rows of Table 5 show that the inferred 10–90% current risetime, averaged over all 24 strokes in the data set, increases by a factor of seven, from 0.31 ± 0.17 $\mu$s at the surface to 2.2 ± 0.5 $\mu$s at 1000 m. (It is worth mentioning that the results do not change much, especially at the higher altitudes, if we average only over the 10 strokes with long current records. In fact, the increase from the surface to 1000 m for this subset is nearly a factor of 12, apparently as a result of shorter risetimes at the surface for these strokes!) Although there is considerable relative variation from stroke to stroke around these means, the reduction in coefficient of variation from 55% at the surface to only 22% at 1000 m suggests that much of this is due to differences among the measured current waveforms at the surface.

[47] The accuracy of the individual risetimes in Table 2 is difficult to assess, given the qualitative nature of the fitting procedure, but the inferred values appear good to ±20% or better. This uncertainty was estimated by varying the risetime of the assumed current and observing the effects on the computed field change in comparison to the observed waveform. In any case, the uncertainty in deduced current risetime is clearly far too small to negate the overall conclusion here.

[48] Referring to the right sides of Figure 19, we see that the optical risetimes deduced from the streak photographs are nearly always larger than the inferred current risetimes, although the overall trends of these two parameters with increasing path length are roughly parallel in most cases (notable exceptions being 8725/5 and 8726/3). These results are also summarized in Table 5, where the estimated optical risetimes have been averaged over all 14 strokes and over all path lengths within ±100 m of the nominal 30, 300, and 1000 m levels. (The mean and standard deviation of the path lengths included in each of these averages are also given in Table 5.)

[49] As discussed in section 1, there are no direct comparisons in the literature for the current risetimes inferred by our modeling. We can, however, compare our optical risetimes with other optical measurements. Most relevant is the streak-recording analysis of *Jordan et al.* [1997] on dart leader and return stroke luminosity variation with height. Indeed, the return stroke risetime variation with height cited by Jordan et al. (1.5 to 4.0 $\mu$s between ground and 1.4 km aloft) is very similar to that presented here in Table 5. Also, *Olsen et al.* [2004], using a photoelectric technique applied to a triggered flash, provided in their Figure 3 a series of luminosity traces that have very similar characteristics to ours. *Mach and Rust* [1989] also presented some luminosity traces from a photoelectric sensor that are apparently quite consistent with our derived traces. On the other hand, *Wang et al.* [1999a] reported that the 10–90% risetime of RLI in two triggered return strokes increased by factors of 2 and 3.5 over the lowest 40–45 m of channel, a region rarely imaged in time-resolved photography.

[50] Comparing estimated optical and inferred current risetimes in Table 5, we see that the former average about 1 $\mu$s longer than the latter at 30 m and 300 m but almost 2 $\mu$s longer at 1 km. These differences cannot be fully explained by the approximately 0.5 $\mu$s native time resolution of the streak camera that was used for these measurements. In addition to the uncertain relationship between luminosity and current in return strokes (see literature review in section 1), however, there are two possible reasons for the greater discrepancy at the highest altitudes (latest times) in the present data set:

[51] 1. The uncertainty in our estimates of RLI risetime tends to be relative (see the last column of Table 3), so that the absolute uncertainty is greater for the larger values. This might be due, in part, to our use of stronger temporal

**Table 3.** Optical Parameters From Streak Photographs

| Event (Flash/Stroke) | Level | Reconstructed | | RLI | | Risetime | |
|---|---|---|---|---|---|---|---|
| | | Height, m | Path, m | Baseline | Amplitude | 10–90%, $\mu$s | Error, $\mu$s ± |
| 8715/9 | 1 | 30 | 30 | 0.0 | 3.6 | 1.3 | 0.07 |
| 8715/9 | 2 | 144 | 144 | 0.8 | 1.5 | 0.9 | 0.07 |
| 8715/9 | 3 | 274 | 299 | 0.5 | 1.5 | 1.3 | 0.07 |
| 8715/9 | 4 | 407 | 480 | 0.9 | 2.2 | 1.7 | 0.14 |
| 8715/9 | 5 | 488 | 597 | 0.6 | 1.5 | 1.1 | |
| 8715/9 | 6 | 675 | 864 | 0.4 | 1.6 | 4.2 | 0.21 |
| 8715/9 | 7 | 787 | 983 | 0.5 | 1.8 | 2.7 | 0.49 |
| 8715/9 | 8 | 919 | 1128 | 0.5 | 1.6 | 2.6 | 0.48 |
| 8715/9 | 9 | 1021 | 1240 | 0.5 | 1.5 | 4.0 | 0.77 |
| 8715/10 | 1 | 30 | 30 | 0.1 | 2.3 | 2.0 | |
| 8715/10 | 2 | 144 | 144 | 0.1 | 1.4 | 1.7 | |
| 8715/10 | 3 | 274 | 299 | 0.0 | 1.2 | 2.8 | 0.07 |
| 8715/10 | 4 | 407 | 480 | 0.3 | 0.8 | 2.6 | |
| 8715/10 | 5 | 488 | 597 | 0.1 | 0.9 | 4.7 | |
| 8715/10 | 6 | 675 | 864 | 0.0 | 0.8 | 4.6 | |
| 8715/10 | 7 | 787 | 983 | 0.1 | 0.6 | 3.8 | |
| 8715/10 | 8 | 919 | 1128 | −0.1 | 0.6 | 4.9 | |
| 8715/10 | 9 | 1021 | 1240 | 0.0 | 0.5 | 5.7 | 0.84 |
| 8725/1 | 1 | 30 | 30 | 0.0 | 1.8 | 1.6 | |
| 8725/1 | 2 | 149 | 150 | 0.1 | 1.1 | 2.3 | |
| 8725/1 | 3 | 267 | 269 | 0.2 | 0.9 | 1.8 | |
| 8725/1 | 4 | 394 | 409 | 0.3 | 0.9 | 2.8 | |
| 8725/1 | 5 | 515 | 580 | 0.2 | 0.8 | 1.4 | |
| 8725/1 | 6 | 603 | 734 | 0.2 | 0.7 | 3.4 | |
| 8725/1 | 7 | 728 | 886 | 0.2 | 0.8 | 3.7 | 0.13 |
| 8725/1 | 8 | 858 | 1077 | 0.2 | 0.5 | 3.0 | 0.06 |
| 8725/1 | 9 | 1011 | 1280 | 0.0 | 0.6 | 5.7 | 0.20 |
| 8725/2 | 1 | 30 | 30 | 0.0 | 1.5 | 0.8 | |
| 8725/2 | 2 | 149 | 150 | 0.2 | 0.7 | 1.8 | |
| 8725/2 | 3 | 267 | 269 | 0.1 | 0.7 | 2.2 | |
| 8725/2 | 4 | 394 | 409 | 0.2 | 0.7 | 2.0 | |
| 8725/2 | 5 | 515 | 580 | 0.1 | 0.7 | 4.2 | |
| 8725/2 | 6 | 603 | 734 | 0.1 | 0.6 | 3.1 | 0.14 |
| 8725/2 | 7 | 728 | 886 | 0.1 | 0.4 | 2.0 | 0.50 |
| 8725/2 | 8 | 858 | 1077 | 0.0 | 0.5 | 5.5 | 0.41 |
| 8725/2 | 9 | 1011 | 1280 | 0.1 | 0.4 | 5.3 | 0.07 |
| 8725/3 | 1 | 30 | 30 | 0.2 | 3.1 | 1.2 | |
| 8725/3 | 2 | 149 | 150 | 1.1 | 2.2 | 1.2 | |
| 8725/3 | 3 | 267 | 269 | 1.0 | 2.1 | 1.2 | |
| 8725/3 | 4 | 394 | 409 | 1.0 | 1.4 | 1.2 | |
| 8725/3 | 5 | 515 | 580 | 1.2 | 1.4 | 1.9 | |
| 8725/3 | 6 | 603 | 734 | 0.9 | 1.6 | 2.8 | |
| 8725/3 | 7 | 728 | 886 | 1.0 | 1.3 | 3.0 | |
| 8725/3 | 8 | 858 | 1077 | 0.7 | 1.5 | 4.2 | |
| 8725/3 | 9 | 1011 | 1280 | 0.5 | 1.3 | 4.5 | |
| 8725/5 | 1 | 30 | 30 | 0.0 | 0.6 | 1.2 | |
| 8725/5 | 2 | 149 | 150 | 0.0 | 0.4 | 2.4 | |
| 8725/5 | 3 | 267 | 269 | 0.0 | 0.3 | 1.2 | |
| 8725/5 | 4 | 394 | 409 | 0.0 | 0.3 | 3.5 | |
| 8725/5 | 5 | 515 | 580 | 0.0 | 0.3 | 6.3 | 1.42 |
| 8725/5 | 6 | 603 | 734 | 0.1 | 0.2 | 4.7 | 0.54 |
| 8725/5 | 7 | 728 | 886 | 0.0 | 0.2 | 5.8 | 0.55 |
| 8725/5 | 8 | 858 | 1077 | 0.1 | 0.2 | 3.9 | 0.54 |
| 8725/5 | 9 | 1011 | 1280 | 0.0 | 0.2 | 7.2 | 0.88 |
| 8726/1 | 1 | 30 | 30 | 0.1 | 2.6 | 0.9 | |
| 8726/1 | 2 | 151 | 151 | 0.8 | 2.2 | 1.4 | |
| 8726/1 | 3 | 269 | 270 | 0.7 | 1.8 | 1.6 | |
| 8726/1 | 4 | 388 | 390 | 0.5 | 1.7 | 2.0 | |
| 8726/1 | 5 | 510 | 513 | 0.5 | 1.6 | 2.3 | |
| 8726/1 | 6 | 627 | 642 | 0.7 | 1.6 | 1.6 | 0.34 |
| 8726/1 | 7 | 817 | 951 | 0.6 | 1.6 | 3.0 | |
| 8726/1 | 8 | 969 | 1167 | 0.7 | 1.5 | 2.1 | 0.21 |
| 8726/1 | 9 | 1098 | 1321 | 0.4 | 1.2 | 4.9 | 0.34 |
| 8726/2 | 1 | 30 | 30 | 0.2 | 3.0 | 0.9 | |
| 8726/2 | 2 | 151 | 151 | 0.0 | 1.0 | 1.4 | |
| 8726/2 | 3 | 269 | 270 | 0.1 | 1.0 | 2.2 | 0.07 |
| 8726/2 | 4 | 388 | 390 | 0.0 | 0.8 | 2.1 | 0.07 |
| 8726/2 | 5 | 510 | 513 | −0.1 | 0.6 | 1.6 | |
| 8726/2 | 6 | 627 | 642 | 0.0 | 0.6 | 2.0 | |
| 8726/2 | 7 | 817 | 951 | 0.0 | 0.7 | 2.6 | |

**Table 3.** (continued)

| Event | | Reconstructed | | RLI | | Risetime | |
|---|---|---|---|---|---|---|---|
| (Flash/Stroke) | Level | Height, m | Path, m | Baseline | Amplitude | 10–90%, $\mu$s | Error, $\mu$s ± |
| 8726/2 | 8 | 969 | 1167 | 0.1 | 0.5 | 4.5 | 0.68 |
| 8726/2 | 9 | 1098 | 1321 | 0.0 | 0.5 | 6.0 | 0.68 |
| 8726/3 | 1 | 30 | 30 | 0.0 | 1.0 | 1.3 | 0.07 |
| 8726/3 | 2 | 151 | 151 | 0.0 | 0.5 | 1.7 | 0.07 |
| 8726/3 | 3 | 269 | 270 | 0.1 | 0.5 | 2.4 | 0.07 |
| 8726/3 | 4 | 388 | 390 | 0.0 | 0.4 | 3.6 | |
| 8726/3 | 5 | 510 | 513 | 0.1 | 0.4 | 3.0 | |
| 8726/3 | 6 | 627 | 642 | 0.1 | 0.3 | 3.4 | |
| 8726/3 | 7 | 817 | 951 | 0.0 | 0.3 | 4.7 | 0.14 |
| 8726/3 | 8 | 969 | 1167 | 0.1 | 0.3 | 5.1 | 0.27 |
| 8726/3 | 9 | 1098 | 1321 | 0.0 | 0.2 | 6.8 | 0.07 |
| 8726/4 | 1 | 30 | 30 | 0.0 | 1.5 | 1.0 | 0.14 |
| 8726/4 | 2 | 151 | 151 | 0.0 | 0.9 | 1.4 | |
| 8726/4 | 3 | 269 | 270 | 0.0 | 0.6 | 1.4 | |
| 8726/4 | 4 | 388 | 390 | 0.0 | 0.5 | 1.4 | 0.14 |
| 8726/4 | 5 | 510 | 513 | 0.0 | 0.4 | 1.9 | |
| 8726/4 | 6 | 627 | 642 | 0.0 | 0.4 | 2.0 | 0.06 |
| 8726/4 | 7 | 817 | 951 | 0.0 | 0.4 | 2.8 | 0.07 |
| 8726/4 | 8 | 969 | 1167 | 0.0 | 0.3 | 4.6 | 0.13 |
| 8726/4 | 9 | 1098 | 1321 | 0.0 | 0.1 | 2.2 | 0.07 |
| 8728/10 | 1 | 30 | 30 | 0.1 | 3.2 | 1.5 | |
| 8728/10 | 2 | 139 | 139 | 0.6 | 2.0 | 1.3 | |
| 8728/10 | 3 | 253 | 273 | 0.5 | 1.9 | 1.9 | |
| 8728/10 | 4 | 394 | 472 | 0.3 | 1.5 | 2.3 | |
| 8728/10 | 5 | 526 | 665 | 0.5 | 1.3 | 2.7 | |
| 8728/10 | 6 | 643 | 851 | 0.6 | 1.4 | 3.1 | |
| 8728/10 | 7 | 738 | 1136 | 0.5 | 1.3 | 4.2 | |
| 8728/10 | 8 | 814 | 1273 | 0.2 | 0.7 | 4.0 | 0.40 |
| 8728/11 | 1 | 30 | 30 | 0.1 | 1.8 | 1.6 | |
| 8728/11 | 2 | 139 | 139 | 0.2 | 1.0 | 1.9 | |
| 8728/11 | 3 | 253 | 273 | 0.1 | 1.1 | 1.9 | |
| 8728/11 | 4 | 394 | 472 | 0.1 | 1.0 | 2.0 | |
| 8728/11 | 5 | 526 | 665 | 0.1 | 0.8 | 2.9 | 0.07 |
| 8728/11 | 6 | 643 | 851 | 0.2 | 0.7 | 3.9 | |
| 8728/11 | 7 | 738 | 1136 | 0.0 | 0.7 | 4.4 | |
| 8728/11 | 8 | 814 | 1273 | 0.0 | 0.3 | 4.8 | 0.14 |
| 8732/1 | 1 | 30 | 30 | 0.2 | 2.2 | 0.9 | 0.07 |
| 8732/1 | 2 | 150 | 150 | 0.1 | 1.6 | 0.9 | 0.07 |
| 8732/1 | 3 | 269 | 295 | 0.3 | 2.0 | 2.1 | |
| 8732/1 | 4 | 395 | 547 | 0.1 | 1.8 | 3.2 | |
| 8732/1 | 5 | 509 | 725 | 0.1 | 1.6 | 2.8 | |
| 8732/1 | 6 | 598 | 981 | 0.1 | 1.1 | 3.2 | 0.07 |
| 8732/1 | 7 | 639 | 1287 | 0.0 | 1.1 | 5.4 | 0.14 |
| 8732/1 | 8 | 705 | 1415 | 0.0 | 1.1 | 4.1 | |
| 8732/1 | 9 | 773 | 1534 | 0.0 | 0.7 | 4.6 | |
| 8732/2 | 1 | 30 | 30 | 0.2 | 2.3 | 1.7 | 0.07 |
| 8732/2 | 2 | 150 | 150 | 0.2 | 1.5 | 1.8 | |
| 8732/2 | 3 | 269 | 295 | 0.1 | 1.4 | 2.5 | |
| 8732/2 | 4 | 395 | 547 | 0.1 | 1.6 | 3.6 | |
| 8732/2 | 5 | 509 | 725 | 0.1 | 1.3 | 3.2 | 0.35 |
| 8732/2 | 6 | 598 | 981 | 0.1 | 1.0 | 4.7 | |
| 8732/2 | 7 | 639 | 1287 | 0.1 | 1.0 | 4.6 | |
| 8732/2 | 8 | 705 | 1415 | 0.1 | 0.9 | 4.6 | 0.14 |
| 8732/2 | 9 | 773 | 1534 | 0.0 | 0.7 | 4.6 | |

filtering for the slower rising waveforms, which also tend to have smaller amplitude (lower signal to noise).

[52] 2. The uncertain current extrapolations in some cases (see the beginning of section 9) result in greater uncertainty in the inferred current risetimes (and amplitudes) at late times (high altitudes).

### 9.2. Propagation Speed

[53] Table 5 also gives the mean, inferred, effective, current front propagation speeds, both at four representative path lengths above the surface and averaged over the full extent of the reconstructed channel for which this parameter could be computed. The individual inferred speeds (see Table 2) are fairly consistent from stroke to stroke (they have a low coefficient of variation around their mean at each level), the only obvious outlier being 8725/4, with an averaged speed of only $0.9 \times 10^8$ m/s. The means are also fairly uniform with height at about $1.8 \times 10^8$ m/s, in spite of the fact that there is a substantial (and apparently unavoidable) increase in $v_{eff}(s)$ with height in two strokes (8728/10

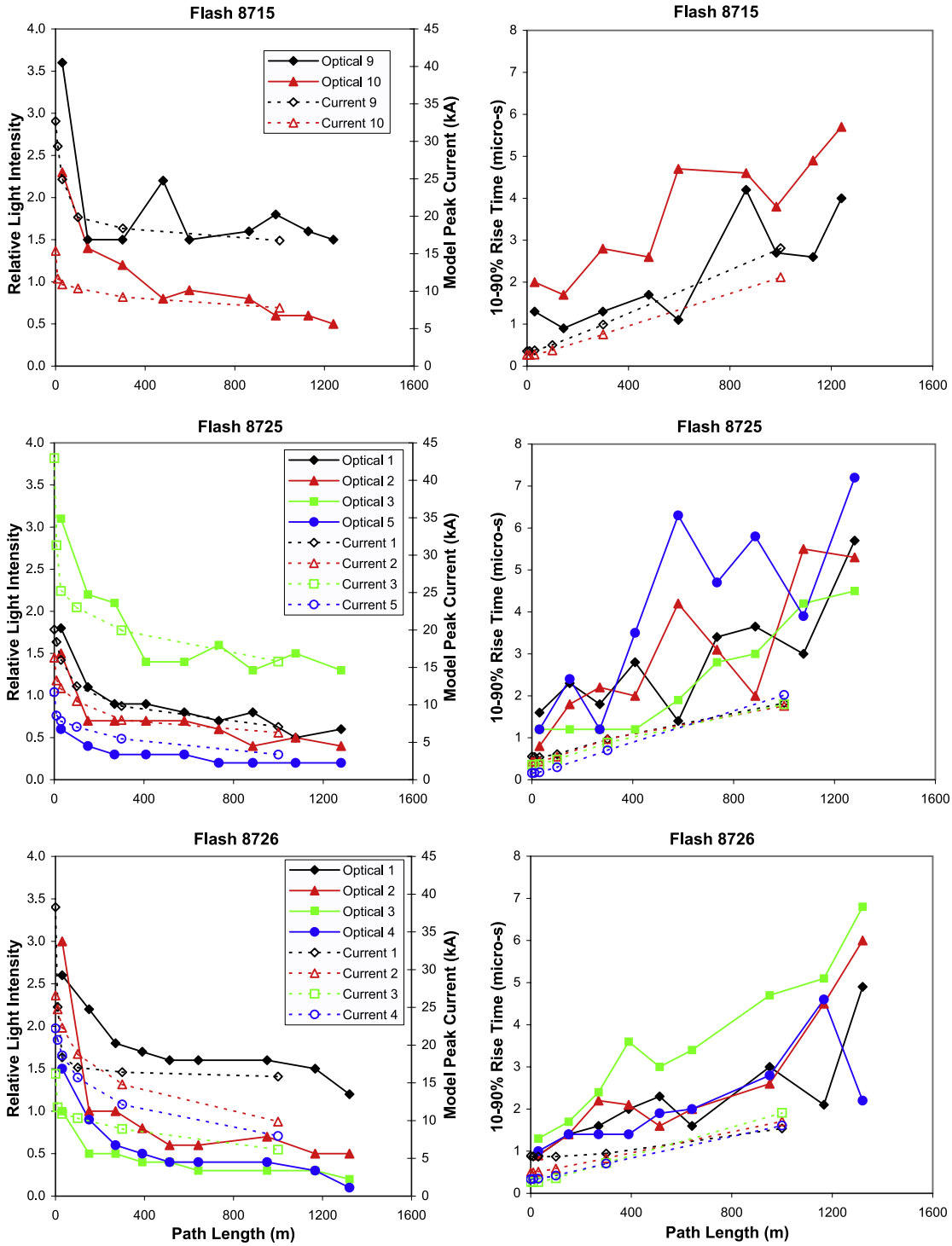


**Figure 19a.** A comparison of optical and electrical results shown as a function of path length. (left) Peak relative light intensity and peak current profiles and (right) 10–90% risetime profiles of RLI and of current. Each flash has its own row of two panels showing all strokes for which both optical data and electrical inferences are available in that flash. Optical results are plotted with solid symbols and lines, whereas electrical results have open symbols connected by dashed lines.

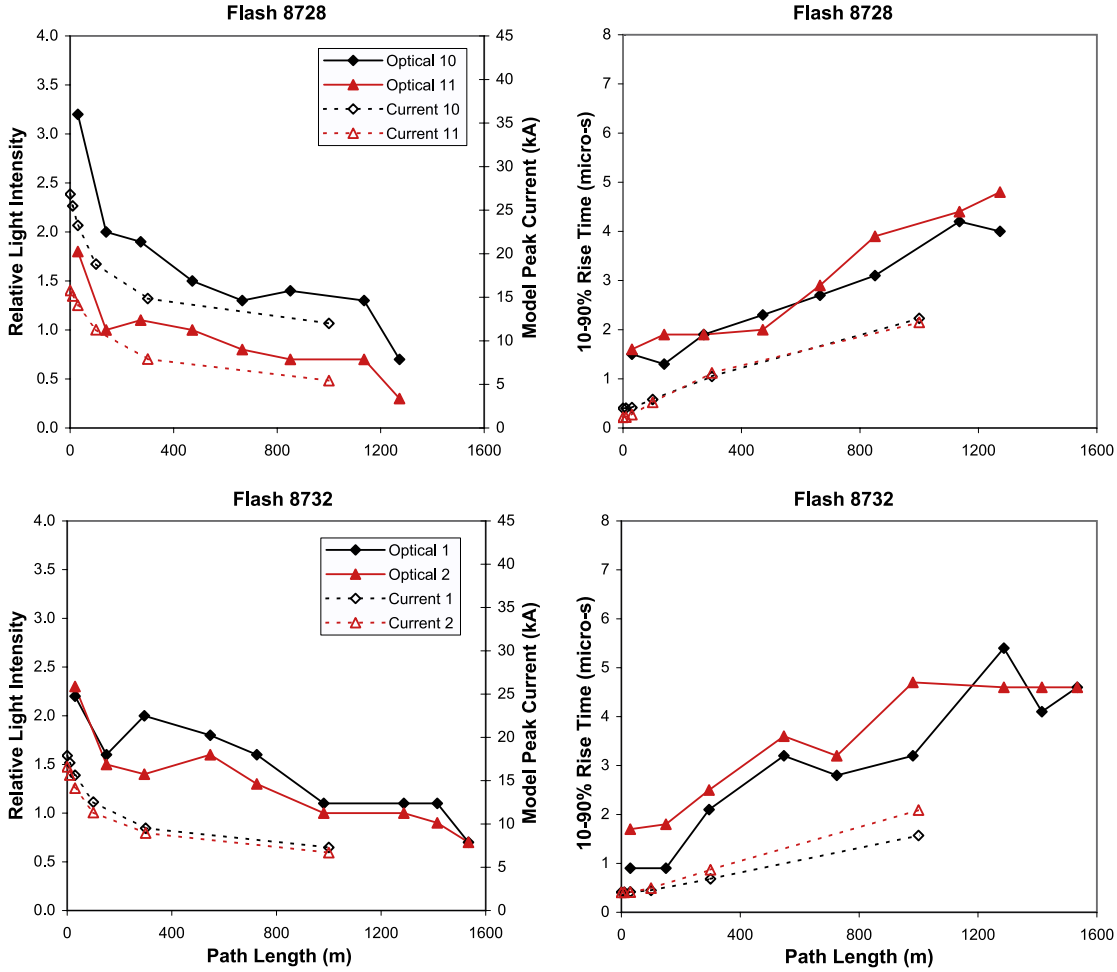


**Figure 19b.** Similar to Figure 19a for the remaining events in which both optical and electrical data are available.

and 8728/11) and an appreciable decrease with height in one other (8726/1). These trends in propagation speed should not be taken very seriously, as mentioned earlier, but the averaged speeds are probably good to better than ±10%: it is fairly easy to detect and eliminate timing differences between the computed and measured fine structure. The variation of averaged $v_{eff}$ from stroke to stroke is probably also real.

[54] The mean, two-dimensional, optical propagation speed, $v_{2D}$, over 14 of these same strokes in five of the six channels is given in Table 5 for comparison, from original data (averaged over the lowest several hundred meters of channel) reported by *Willett et al.* [1989a]. Note that our mean, averaged, three-dimensional $v_{eff}$ is about 23% larger than the mean, averaged, 2-D, optical speed. This difference is not too surprising in the light of previous work on 2-D versus 3-D channel lengths by *Idone et al.* [1984]. It can also be seen from Table 3 that the ratio of the total path length to the vertical height from the surface to optical level nine averages 1.45 ± 0.30 over our six reconstructed channels.

[55] Once again there are no direct comparisons for our inferred current front speeds, but the originally reported optical two-dimensional mean speed of $1.5 \times 10^8$ m/s is quite consistent with the results of *Idone et al.* [1984] and of *Mach and Rust* [1989], both of which contained sizable numbers of strokes from triggered flashes that were analyzed over comparable height ranges. More recently, the use of multiple, well-collimated, photoelectric sensors coupled

**Table 4.** Model Peak Current (kA) Versus Path Length

| | Path Length, m | | | | | |
|---|---|---|---|---|---|---|
| Event (Flash/Stroke) | 0 | 10 | 30 | 100 | 300 | 1000 |
| 8715/9 | 32.7 | 29.3 | 24.9 | 19.9 | 18.4 | 16.8 |
| 8715/10 | 15.4 | 11.7 | 10.9 | 10.4 | 9.2 | 7.8 |
| 8725/1 | 20.1 | 18.4 | 16.0 | 12.5 | 9.8 | 7.1 |
| 8725/2 | 16.3 | 13.3 | 12.2 | 10.5 | 8.0 | 6.3 |
| 8725/3 | 43.0 | 31.3 | 25.2 | 23.0 | 20.0 | 15.8 |
| 8725/5 | 11.7 | 8.6 | 7.8 | 7.1 | 5.5 | 3.4 |
| 8726/1 | 38.3 | 25.1 | 18.4 | 17.0 | 16.4 | 15.8 |
| 8726/2 | 26.6 | 24.8 | 22.3 | 18.8 | 14.8 | 9.9 |
| 8726/3 | 16.2 | 11.8 | 10.9 | 10.3 | 8.9 | 6.2 |
| 8726/4 | 22.2 | 20.7 | 18.6 | 15.7 | 12.1 | 8.0 |
| 8728/10 | 26.8 | 25.5 | 23.3 | 18.8 | 14.9 | 12.0 |
| 8728/11 | 15.8 | 15.2 | 14.1 | 11.3 | 7.9 | 5.4 |
| 8732/1 | 17.9 | 17.1 | 15.6 | 12.5 | 9.5 | 7.3 |
| 8732/2 | 16.6 | 15.7 | 14.1 | 11.3 | 9.0 | 6.7 |
| Mean scaled (see text) | 1.58 | 1.33 | 1.17 | 1.00 | 0.82 | 0.63 |
| SD scaled | 0.24 | 0.11 | 0.08 | 0.00 | 0.07 | 0.12 |

**Table 5.** Comparison Among Values Averaged Over Strokes

| | Path Length Above Surface | | | | | | |
|---|---|---|---|---|---|---|---|
| Parameter | 0 m | 10 m | 30 m | 100 m | 300 m | 1000 m | Averaged |
| | | | *10–90% Risetime of Current Waveform* | | | | |
| Average, $\mu$s | 0.312 | 0.313 | 0.332 | 0.460 | 0.884 | 2.18 | |
| SD, $\mu$s | 0.172 | 0.168 | 0.158 | 0.126 | 0.165 | 0.47 | |
| Number of samples | 24 | 24 | 24 | 24 | 24 | 24 | |
| | | | *10–90% Risetime of Relative Light Intensity* | | | | |
| Average, $\mu$s | | | 1.3 | | 2.0 | 3.8 | |
| SD, $\mu$s | | | 0.4 | | 0.6 | 1.0 | |
| Number of samples | | | 14 | | 18 | 20 | |
| Average path, m | | | 30 | | 303 | 1062 | |
| SD path, m | | | 0 | | 49 | 86 | |
| | | | *Effective Current Propagation Speed* | | | | |
| Average, $10^8$ m/s | | 1.76 | | 1.75 | 1.78 | 1.81 | 1.80 |
| SD, $10^8$ m/s | | 0.30 | | 0.20 | 0.22 | 0.30 | 0.24 |
| Number of samples | | 24 | | 24 | 24 | 22 | 24 |
| | | | *2-D Average Optical Propagation Speed* | | | | |
| Average, $10^8$ m/s | | | | | | | 1.5 |
| SD, $10^8$ m/s | | | | | | | 0.1 |
| Number of samples | | | | | | | 14 |
| | | | *Charge Amplitude Multiplier* | | | | |
| Average | 1.00 | 0.88 | 0.79 | 0.68 | 0.58 | 0.49 | |
| SD | 0.00 | 0.10 | 0.11 | 0.08 | 0.06 | 0.09 | |
| Number of samples | | 24 | 24 | 24 | 24 | 24 | |
| | | | *Peak Amplitude of Current Waveform* | | | | |
| Average, kA | 22.8 | 19.2 | 16.7 | 14.2 | 11.7 | 9.2 | |
| SD, kA | 9.4 | 7.1 | 5.6 | 4.6 | 4.4 | 4.3 | |
| Number of samples | 14 | 14 | 14 | 14 | 14 | 14 | |
| | | | *Amplitude of Relative Light Intensity* | | | | |
| Average | | | 2.2 | | 1.1 | 0.9 | |
| SD | | | 0.9 | | 0.6 | 0.5 | |
| Number of samples | | | 14 | | 18 | 20 | |
| Average path, m | | | 30 | | 303 | 1062 | |
| SD path, m | | | 0 | | 49 | 86 | |

to modern digitizing electronics has permitted *Wang et al.* [1999b] and *Olsen et al.* [2004] to measure two-dimensional propagation speeds for a few rocket-triggered strokes over much shorter channel segments near the surface. Their results are generally consistent with those cited above. Although *Olsen et al.* [2004] reported speeds that increased with height over the lowest 100–200 m of channel, *Wang et al.* [1999b] reported speeds that generally decreased with height.

### 9.3. Amplitude of Current

[56] The mean, inferred, charge amplitude multiplier, $a(s)$, can be seen in Table 5 to decrease from unity at the surface (by definition) to 0.68 ± 0.08 at 100 m and to 0.49 ± 0.09 at 1000 m. (It is worth mentioning that the result at the 1000 m level does change appreciably when we average only over the 10 strokes with long current records. This suggests that $a(s)$ in the upper parts of the channels might be affected significantly by our extrapolation of the corresponding surface current records, as mentioned in section 9.1.) The relative variability of the values for individual strokes at the various levels is quite small, although 8725/3 and 8726/1 might be considered outliers at the lower levels (see Table 2). As before, the uncertainty in our inferred values of $a(s)$ (and in the peak currents in Table 4, discussed below) was estimated to be ±10% or better by varying $a(s)$ and observing its effects on the computed field change amplitude in comparison to the observed waveform. This low apparent uncertainty should not be too surprising, since amplitude differences between computed and measured field change are fairly easy to detect and eliminate.

[57] Recall from earlier sections that two length scales were usually required for $a(s)$: a shorter one of a few tens of meters or less to fit the peak measured field change, $E_{mp}$, and a longer one of a few hundred meters to fit the amplitude of $E_m(t)$ at later times. We have tried to capture the relative importance of these two scales by focusing above on the 100 m and 1000 m levels, but it can be seen better by examining the relevant fit parameters in Table 1. Mean values of these parameters over the 19 strokes for which all four of them are defined are $a_{\min 1} = 0.72 \pm 0.09$, $L_{a1} = 31 \pm 29$ m, $a_{\min 2} = 0.62 \pm 0.15$, and $L_{a2} = 430 \pm 280$ m. As mentioned previously (e.g., Figure 13), the very rapid decreases in $a(s)$ with increasing path length that are inferred in several cases imply that these return strokes deposit a significant fraction of their total charge in the lowest few tens of meters above the surface.

[58] Such localized charge depositions are not implied by very close measurements, however. An example of such

measurements is given by *Rakov et al.* [2005, Figure 2], which shows electric field changes for two strokes that decrease in magnitude by nearly a factor of two from 15 m to 30 m range. *Schoene et al.* [2003] found that the ratio of return stroke electric field change measured 15 m from the channel base to that at 30 m range averaged 1.76 ± 0.15 over 77 rocket-triggered strokes, suggesting a range dependence of $r^{-0.8}$, a falloff noticeably slower than $1/r$. This may be compared with a similar average ratio for the field change due to the immediately preceding dart leaders of 1.88 ± 0.15, suggesting a range dependence of $r^{-0.9}$. Such a slow falloff of field change with range could be interpreted to indicate that the magnitude of the linear charge density deposited by the stroke (often assumed to be equal and opposite to that deposited by the leader) increases with height over the lowest hundred meters of so of channel [*Rakov et al.*, 1998]. In contrast, our own calculations of the close field changes that would be produced by model strokes having very rapid decreases in $a(s)$ (such as 8725/3 and 8726/3) predict a falloff with range that is considerably faster than $1/r$ within a few tens of meters of the channel base.

[59] We have found only one reference in the literature that appears consistent with our inference of rapidly decreasing $a(s)$ near the surface. *Wang et al.* [1999a] reported that time-resolved optical imaging near the channel base of two triggered strokes showed peak RLI to attenuate by about 30% over the lowest tens of meters. In spite of this lone observation, however, the discrepancy between our inference and the recent observations of close electric fields cited above leads us to question the meaning of our deductions. An alternative interpretation that is motivated by our streak images and appears more physically reasonable is proposed in the next section.

[60] Further insight into the need for coupling a value of $a_{\min 1}$ that is significantly less than unity with a very short $L_{a1}$ in certain cases (especially 8715/7, 8715/9, 8715/10, 8725/3, 8725/5, 8726/1, 8726/3, and 8726/5) can be obtained by comparison of the physical propagation speeds that are discussed above with the so-called transmission line model velocity, $v_{TLM} \equiv -(2\pi D/\mu_0)E_{mp}/i_p(0)$ [e.g., *Willett et al.*, 1989a]. This $v_{TLM}$ is just another way of looking at the ratio of peak radiation field measured at horizontal range, $D$, to peak current measured at the surface. Its values have been recalculated at our observing range, $D = 5.2$ km, using the new zero and peak levels of $E_m(t)$ that are shown in Figure 16, where we have attempted to better remove any field change due to the leader. Here, $v_{TLM}$ averages $1.34 \pm 0.15 \times 10^8$ m/s over our 24 strokes (only 10% smaller that the $1.49 \pm 0.15 \times 10^8$ m/s that would be computed by averaging $v'_{TLM}$ from *Willett et al.* [1989a, Table 1] over the same set of strokes). The ratio of observed $v_{2D}$ to calculated $v_{TLM}$ averages 1.17 ± 0.20 over the 14 strokes for which both are available. The fact that $v_{2D}$ tends to be the larger of the two indicates that its use as a physical propagation speed for the return stroke current front in our (or any other transmission line–like) model will tend to overpredict $E_{mp}$ in many cases (as already found, though to a lesser extent, by *Thottappillil and Uman* [1993]) unless radical measures (specifically, the very rapid decreases in $a(s)$ with increasing path length near the surface that have been discussed above) are taken to prevent this. (The comparable ratio computed from *Willett et al.* [1989a, Table 1] would be 1.03 ± 0.16, which is why those authors found excellent agreement in peak electric field between their TLM predictions from $v_{2D}$ and the observations.)

[61] We have already seen in the previous section that the inferred 3-D speed, $v_{eff}(s)$, when averaged over most of the reconstructed channel, tends to be even larger than $v_{2D}$. Thus it is not surprising that $v_{eff}(10)/v_{TLM}$ (where the effective front speed at the 10 m level from Table 2 has been used as the most relevant to the peak of $E_c(t)$) averages 1.34 ± 0.32 over all 28 return strokes. This implies an even greater overprediction of $E_{mp}$ in the present modeling, as illustrated in Figure 5 for example. To obviate this overprediction, a very rapid decrease in $a(s)$ with increasing path length is required in several cases. Indeed, the same strokes listed in the previous paragraph have among the largest ratios, $v_{eff}(10)/v_{TLM}$. Nevertheless, we are convinced that our inferred values of $v_{eff}$ are the best propagation speeds available for this application. The good agreement found in earlier evaluations of the TLM on this data set by *Willett et al.* [1989a] and by *Thottappillil and Uman* [1993] is evidently the result of using stroke propagation speeds that were too small.

[62] Next we compare the peak currents inferred from our modeling with the peak relative light intensity measured from the streak photographs. Inferred peak currents at several levels have been listed in Table 4 for the 14 strokes also having streak photographs. Mean values of $i_p(s)$ are given in Table 5 for comparison with the corresponding average amplitudes of relative light intensity from Table 3 (shown in the same manner as those of 10–90% RLI, discussed above). It is gratifying that both of these averages decrease at roughly the same rate with increasing height. (The agreement becomes nearly perfect if the mean RLI amplitude at optical level one is compared with $i_p$ at the surface instead of that at 30 m. An argument for this adjustment will also be discussed in the next section.) Looking back at the left sides of Figure 19, we also see that individual profiles of $i_p(s)$ and RLI amplitude agree reasonably well, both in slope and in overall relative magnitude, although exceptions to the former include strokes 8715/10 and 8726/1 and exceptions to the latter include 8726/2, 8726/3, 8726/4, 8732/1, and 8732/2.

[63] The evolution of relative light intensity with height in return stroke channels has also been evaluated photographically by *Jordan and Uman* [1983] and by *Jordan et al.* [1997]; *Mach and Rust* [1989] do not present formal analyses, but assert that their photoelectric data is generally consistent with that of *Jordan and Uman* [1983]. Fundamentally, the peak luminous intensity of the subsequent return stroke is observed to decrease with height by about a factor of two over 500 m, in fair agreement with the present optical results.

[64] Another noteworthy feature of the left sides of Figure 19 is that the RLI amplitude at optical level one is occasionally much brighter than that at level two. That is, there is sometimes a dramatic change in the slope of the amplitude profile at level two. This is especially evident in strokes 8715/9, 8726/2 and 8728/10. Looking at the streak photographs themselves, it is obvious that the first and last of these three strokes, plus 8725/3 and 8726/1, are preceded by particularly bright dart leaders. Figure 20 shows the most

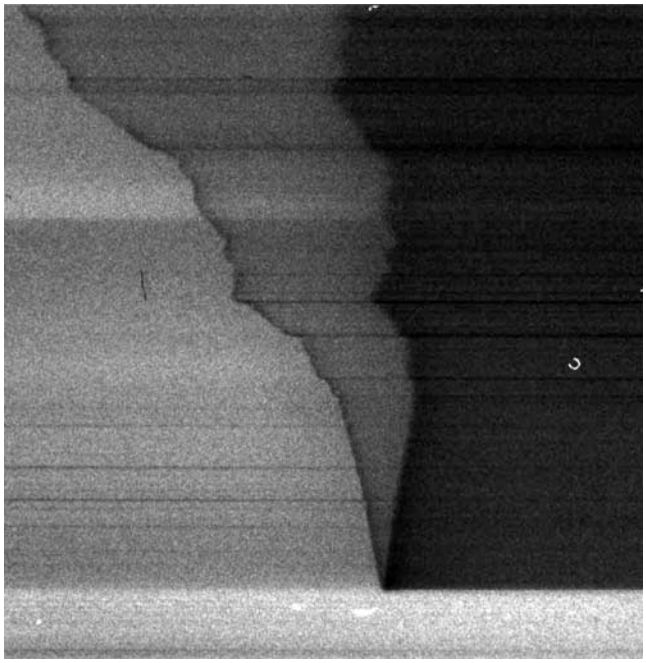

**Figure 20.** Similar to Figure 18 but for stroke 8725/3, which has an especially bright leader.

dramatic example, stroke 8725/3, which may be compared with more typical stroke 8725/1 in Figure 18. Since the optical emissions from leader and return stroke are generally indistinguishable at optical level one, because of the limited time resolution of the streak camera, the tabulated values of stroke RLI amplitude at the lowest measurement level must have been significantly exaggerated by leader light emission in at least some cases.

[65] An objective evaluation of any such exaggerated stroke brightness at the lowest optical level would involve a comparison of the brightness of the leader relative to its return stroke. This comparison can be made reasonably quantitative by forming the ratio, from Table 3, of the RLI "baseline" to its "amplitude" at each level. Recall that this baseline is measured immediately before the onset of the return stroke and thus approximately represents the residual brightness of the leader channel (relative to a zero at the same level before leader onset), whereas the amplitude is the difference between the peak RLI during the onset of the return stroke (relative to the same zero) and the corresponding baseline value. (At the higher levels this baseline value may be substantially less accurate than the stroke amplitude because considerable time may have elapsed since the corresponding zero reading. Note that the leader tip is often appreciably brighter, as in Figure 20, but is not measured here.) This ratio has been calculated for each stroke at every level (except where "baseline" is negative or where "amplitude" is small enough to produce excessive noise in the ratio) and then averaged over all levels except the lowest (where leader and return stroke are presumed indistinguishable). The results are indeterminate in two cases (8725/5 and 8726/3) because of low return stroke amplitudes, but otherwise range from near zero (strokes 8726/2, 8726/4, 8732/1 and 8732/2) to over 30% (8715/9, 8725/3, 8726/1, and 8728/10), the largest ratio being 59% for stroke 8725/3.

[66] The first indication that anomalously bright dart leaders do occur was from *Guo and Krider* [1985], who reported one or more of them in about 5% of natural multiple-stroke flashes in Florida and argued that leader brightness might occasionally equal or even exceed that of the corresponding subsequent return stroke. *Idone and Orville* [1985] found that the ratio of dart leader to return stroke RLI (measured 50 m above the channel base) averaged 0.1 ± 0.07 over 22 triggered strokes in which leader brightness could be measured; and they estimated the corresponding ratio of peak currents to average 0.17, but with a rather large range of [0.03, 0.3]. *Jordan et al.* [1997] reported that the brightest three of 23 dart leaders in natural subsequent strokes had peak RLIs 30–50% that of the corresponding return strokes. They also referred to (but did not report) measurements of the "plateau" brightness (after the dart peak but before the stroke onset), which is the quantity that is approximated by the "baseline" values in our Table 3. *Mach and Rust* [1997] reported what they called "postdart" brightness relative to that of the dart peak. Dividing mean values from their Table 1, we infer an average ratio of postdart to return stroke peak brightness of roughly 1/16. Finally, *Kodali et al.* [2005] reported a mean ratio of dart leader current (inferred from their near-field measurements on triggered strokes, assuming the leader current above the tip to be uniform and constant) to measured return stroke peak current of 0.22. On the basis of these references, the values in our Table 3 seem reasonable.

### 9.4. Leader Versus Return Stroke Current

[67] Table 6 compares our objective measure of leader/return stroke relative brightness with two possible indicators of radical measures to fit $E_{mp}$: $a(100)$ and $v_{eff}(10)/v_{TLM}$, both discussed in the previous section. As expected, the correlation coefficient between $a(100)$ and $v_{eff}(10)/v_{TLM}$ is high: −0.88 over all 24 strokes, significantly different from zero at well over the 99% confidence level. The correlations of our leader/return stroke brightness ratio with these two

**Table 6.** Correlations With Leader Relative Brightness

| Event | RLI Ratio | $a(100)$ | $v_{eff}(10)/v_{TLM}$ |
|---|---|---|---|
| 8715/2 | | 0.78 | 1.06 |
| 8715/3 | | 0.75 | 1.20 |
| 8715/4 | | 0.73 | 1.23 |
| 8715/6 | | 0.72 | 1.08 |
| 8715/7 | | 0.61 | 1.40 |
| 8715/8 | | 0.74 | 1.16 |
| 8715/9 | 0.36 | 0.61 | 1.35 |
| 8715/10 | 0.10 | 0.69 | 1.35 |
| 8717/3 | | 0.70 | 1.12 |
| 8717/5 | | 0.76 | 1.11 |
| 8725/1 | 0.23 | 0.64 | 1.41 |
| 8725/2 | 0.17 | 0.66 | 1.32 |
| 8725/3 | 0.59 | 0.54 | 1.62 |
| 8725/4 | | 0.76 | 0.96 |
| 8725/5 | | 0.64 | 1.44 |
| 8726/1 | 0.37 | 0.45 | 2.63 |
| 8726/2 | 0.04 | 0.72 | 1.35 |
| 8726/3 | | 0.65 | 1.44 |
| 8726/4 | 0.00 | 0.72 | 1.34 |
| 8726/5 | | 0.63 | 1.50 |
| 8728/10 | 0.32 | 0.71 | 1.23 |
| 8728/11 | 0.13 | 0.75 | 0.98 |
| 8732/1 | 0.05 | 0.71 | 1.46 |
| 8732/2 | 0.08 | 0.69 | 1.34 |

parameters are −0.74 and +0.41, respectively, over 12 strokes. Thus the brightness ratio is significantly correlated with the 100 m charge amplitude multiplier at the 99% confidence level, although its correlation with the velocity ratio is not statistically significant. These results suggest that the peak currents measured at the surface exaggerate those in the return strokes themselves by essentially the same mechanism that was described for RLI above, especially in cases of relatively bright (high-current) leaders. In other words, the leader and return stroke currents probably cannot be distinguished at the ground. We suspect that this is the reason for the above mentioned tendency toward overprediction of $E_{mp}$, as well as for the extremely rapid decreases in $a(s)$ that we have employed to obviate it.

[68] Although this is a new idea, to our knowledge, the relationship between leader and return stroke current that it presumes is not new. For example, *Lin et al.* [1980] assumed that the leader current continues to flow after the onset of the return stroke, remaining uniform and constant above the advancing return stroke front. This concept was mentioned again by *Jordan et al.* [1997, p. 22,030], who remarked that the optical "plateau" that they observed in natural dart leaders suggested "that a steady leader current flows through each channel section behind the downward moving leader tip before, and perhaps for some time after, the return stroke has passed that channel section."

[69] Consider the following simple argument, based on the transmission line model. (Here we ignore the transient effects of any upward connecting discharges and/or reflections at the ground on the currents and radiation fields in these triggered subsequent strokes.) Let the current and front propagation speed of the dart leader be $i_L$ and $-v_L$, respectively, while the corresponding parameters for the return stroke are $i_S$ and $+v_S$. Near the surface the leader front radiates a field proportional to $-i_L v_L$ that turns off when the leader reaches ground. The return stroke then begins radiating a field proportional to $-i_S v_S$ as it propagates up the leader channel from ground. Assume, with the references in the previous paragraph, that the leader current continues and remains uniform along the channel after stroke onset. The peak total current at any level (including that measured at stroke onset by a shunt at the surface) is then $i_L + i_S$, which may be significantly greater than $i_S$ alone in cases with relatively bright leaders. Since $i_L < i_S$ and $v_L << v_S$, however, the change in radiated field magnitude at return stroke onset is proportional to $-i_S v_S - (-i_L v_L) \approx -i_S v_S$. (For example, taking the average ratios, $v_L \approx v_S/6$ from *Idone et al.* [1984] and $i_L \approx 0.22 i_S$ from *Kodali et al.* [2005], we find a radiation field change proportional to $-0.96 i_S v_S$.) Thus it is essentially only the return stroke current itself that is relevant to the distant (radiation) field change. Our measured $E_m(t)$ at $D$ = 5.2 km consists essentially of radiation field at the time of $E_{mp}$, so this analysis should be relevant here. Thus it is our hypothesis that the downward propagating leader current is included in the measured current at the channel base, from which it must be removed in order to obtain an estimate of the upward propagating current in the return stroke that will be consistent with the radiated field change.

[70] The above argument appears consistent with both the streak photographs and our inferred rapid decreases of $a(s)$ and $i_p(s)$ in cases of relatively bright leaders. We claim that the latter are merely the inevitable consequence of presenting our model-fitting procedure with exaggerated measurements of return stroke current amplitude at the surface. It even makes sense to compare the mean RLI amplitude at optical level one with $i_p$ at the surface if both measurements then fully include the effects of the leaders. If correct, this argument obviously also has implications for the widespread estimation of return stroke speeds from measured $E_{mp}$ and $i_p(0)$ through $v_{TLM}$.

[71] The question remains whether the above inferences about $a(s)$ and $i_p(s)$ can be corrected for this effect. Since we do not know how to accurately remove the leader current from the measured surface current waveforms, however, we confine ourselves here to a single illustrative example. For stroke 8725/3 the velocity ratio in Table 6, $v_{eff}(10)/v_{TLM}$ = 1.62 $\approx E_{cp}/E_{mp}$, where $E_{cp}$ is the peak field that would be predicted in the absence of any radical adjustment of $a(s)$ near the ground. This implies an overprediction of the actual peak field by 62% unless the measured current waveform is adjusted in some way, for example, by assigning $i_L/(i_L + i_S) = 1 - [v_{eff}(10)/v_{TLM}]^{-1}$ = 38% of $i_p(0)$ to the leader. The level-averaged leader/return stroke brightness ratio, (*RLI Ratio*) = 0.59 $\sim i_L/i_S$, also suggests assigning $i_L/(i_L + i_S) \sim$ (*RLI Ratio*)/[(*RLI Ratio*) + 1] = 37% of $i_p(0)$ to the leader, almost the identical result in this case. On the other hand, the best fit model of this stroke that was determined in earlier sections gave $a(100) = 0.54 \sim i_S/(i_L + i_S)$, suggesting that $i_L/(i_L + i_S) \sim 1 - a(100)$ = 46% of $i_p(0)$ be assigned to the leader, probably an overestimate, since $a(100)$ likely includes some of the real decay of stroke current amplitude with height.

[72] In the model we find that a slightly smaller leader current equal to 44% of $i_p(0)$, corresponding to $i_S = 0.56 \times i_p(0)$ or to $i_L/i_S$ = 79%, allows us to entirely eliminate the shorter of the two length scales for $a(s)$. (To achieve this reduction, the measured current waveform is decreased to 56% of its original magnitude throughout the time interval before its peak, whereas a constant 18.9 kA leader current is subtracted from it at all later times, leaving the return stroke peak current at only 24.1 kA. Obviously this method of modifying the current waveform is somewhat arbitrary, but it is a reasonable manifestation of the concept of subtracting off a constant leader current.) A fit of $E_c(t)$ to $E_m(t)$ that is essentially the same as that shown in Figure 16c can then be obtained using $a_{\min 1}$ = 0.82, $L_{a1}$ = 500 m, and $a_{\min 2}$ = 1.0 (all other parameters remaining as in Table 1). The resulting measurements of 10–90% current risetime and of effective stroke front speed at the various levels remain essentially unchanged from those in Table 2. Although $a(s)$ changes dramatically, of course, $i_p(s)$ changes from the values in Table 4 only at the lowest two levels, remaining essentially the same at 30, 100, 300, and 1000 m. This satisfying result strengthens our suspicion that return stroke currents are exaggerated by surface measurements.

[73] Because of the uncertainties inherent in the above procedure, leader currents have not been estimated explicitly for the other return strokes in our data set. As seen in the above example, we used three potential indicators of leader current [$v_{eff}(10)/v_{TLM}$, (*RLI Ratio*), and $a(100)$], which do not necessarily agree. The required data are available in Table 6 (and elsewhere), in case the reader wishes to work out values of $i_L/(i_L + i_S)$ for additional cases. It is worth

pointing out, however, that the only other truly clear-cut example, in which all indicators point to an unusually bright leader that would result in a serious overprediction of peak field in the absence of either radical adjustment of $a(s)$ or removal of the leader current, is stroke 8726/1. There is also one case, 8728/11, in which the leader is faint and there is no overprediction, so that significant adjustments are clearly unnecessary. The other cases either are missing usable streak photographs or are more ambiguous, but only one is potentially at odds with our hypothesis: Stroke 8715/10 appears to have a faint leader but to require considerable adjustment of $a(s)$ in order to obviate significant overprediction of peak field.

[74] Nevertheless, the data in Table 6 do lend statistical support to our hypothesis, as shown at the beginning of this section, so a field experiment that is specifically targeted at testing this hypothesis is recommended. It is suggested that modern, near-field measurements, such as have been reported recently from Camp Blanding, Florida (e.g., *Kodali et al.* [2005], which allowed more direct estimation of the leader currents), coupled with far-field measurements of the peak fields radiated by the same return strokes, might be appropriate.

[75] On the basis of our hypothesis, the inference in Tables 1, 2, 4, and 5 (and elsewhere) of very rapid decreases in $a(s)$ and $i_p(s)$, and the consequent concentrations of charge deposition that are illustrated in Figures 8 and 13, near the surface in several cases are probably invalid. These artifacts are argued to result from using the total measured current at the surface as the initial current into the base of the return stroke itself. There is no fully satisfactory way to correct this problem in the present data set. Nevertheless, it appears that the inferred values of current risetime at all levels and of average effective stroke propagation speed are unaffected, even in strokes with very bright leaders. Further, we believe our inference of decreasing current amplitude above about 100 m of path length (taken as a compromise between the mean values of $L_{a1}$ = 31 m and $L_{a2}$ = 430 m, noted in the previous subsection, the former length scale now being assumed to be largely spurious). The last two rows of Table 4 are intended to better distinguish the presumed valid and the probably invalid variations of inferred peak current. There we have first scaled the values tabulated for each stroke relative to that at 100 m and then calculated means and standard deviations of these scaled results for each level. We conclude that the peak current probably does decrease by about 37%, on average, between 100 m and 1000 m of path length above the ground. On the other hand, the peak current may well increase much less than 58%, on average, between 100 m and the surface.

## 10. Summary and Conclusions

[76] This paper has attempted to take advantage of three-dimensional channel reconstructions of rocket-triggered lightning flashes in Florida in order to infer the behavior of the current in return strokes above the ground from current waveforms measured at the channel base and electric field change waveforms measured at a range of 5.2 km. The reconstruction of six lightning channels from stereo photographs was described in detail in Appendix A. The method of calculating field change signatures due to return strokes that follow these piecewise linear channels was then explained. Formal assumptions about the variation of stroke current waveforms along the channels constrained the problem enough that the risetime, propagation speed, and peak amplitude of the current could be estimated as a function of path length with reasonable confidence. Results were first presented in Tables 1, 2, 4 and 5, on the tacit assumption that the measured current waveforms were entirely due to the return strokes themselves.

[77] Some of the results derived in this way are the following: (1) The fine structure of the field change waveforms that are radiated by subsequent return strokes can be explained, in large part, by channel geometry, although it can also be affected significantly by the shape of the current waveform that enters the channel base. (2) The average 10–90% risetime of the stroke current increased by about a factor of seven in our sample of 24 triggered strokes, from an observed $0.31 \pm 0.17$ $\mu$s at the surface to an inferred $2.2 \pm 0.5$ $\mu$s at 1 km path length above the surface. (3) The three-dimensional propagation speed of the current front averaged $1.80 \pm 0.24 \times 10^8$ m/s over channel lengths typically greater than 1 km for the same 24 strokes.

[78] Next, streak photographs of a subset of these return strokes were analyzed in terms of relative light intensity versus path length and time (see Table 3), and the resulting estimates of risetime, propagation speed, and peak amplitude of the RLI were compared with the corresponding electrical estimates for current in Table 5 and Figure 19. Although these comparisons appeared generally reasonable, two anomalies were noted that suggested a variation in the modeling. First, it was remarked that even the optically measured, two-dimensional, stroke propagation speeds (which were a reasonable amount smaller than the electrically inferred, three-dimensional, current front propagation speeds, as shown in Table 5) tended to overpredict the peak radiation fields unless radical measures (which appeared to conflict with other results in the literature) were employed to obviate this (see section 9.3). Second, it was noted that peak RLI amplitudes for return strokes sometimes decreased dramatically between the lowest measurement level, where the leader and return stroke could not be distinguished, and the next higher level, where they could be (see Figure 19). Both of these anomalies tended to occur most markedly in cases where the leaders were brightest relative to their strokes (again see section 9.3). It was concluded that (4) a significant fraction of the measured current at the surface was probably due to the leaders in cases when they were relatively bright (see section 9.4 and Table 6). Therefore our assumption that these measured currents were entirely due to the return strokes was forcing an unreasonably large and abrupt reduction in inferred current amplitude over the first few tens of meters above the surface.

[79] With this conclusion in mind, the first inferences of current amplitude as a function of height were reexamined. It was judged that the anomalously abrupt decreases with increasing height near the surface were probably spurious, but that the slower increases at higher altitudes were valid. Thus the final conclusion of our study is that (5) return stroke peak currents decreased by about 37 ± 12% from 100 m to 1 km of path length above the surface over our 24 strokes. Although these peak currents likely also decreased

between the surface and 100 m, this decrease was probably not as great as originally inferred.

## Appendix A: Three-Dimensional Channel Reconstruction

[80] Figure A1 shows one example (flash 8732) of the six stereo pairs of still photographs that were taken with automated 35 mm cameras from the two sites (NRL and SUNY) during the 1987 experiment. These photographs were all printed at the same magnification (6.8×) on $8'' \times 10''$ paper, and the lightning channels were then digitized by marking a point at every visually detectable deviation from straight lines. Typically, this produced a few hundred points per channel image that were tabulated in centimeters ($X$, $Y$) relative to the "principal point" [*Hallert*, 1960, p.18], which was taken to be at the center of the print (±0.5 cm). Connecting these points with straight lines results in a piecewise linear representation of the channel.

[81] Figure A2a shows the locations of the two cameras relative to the triggering site, which is taken as the origin of a right-handed, Cartesian coordinate system ($x$, $y$, $z$) with its $z$ axis vertical and its $x$ axis passing through the NRL site (almost due east of the triggering site). The position parameters for each site are given in Figure A2a, as determined (±0.6 m) from a survey of the area that was conducted by KSC. The azimuthal orientation of the cameras (rotation about the vertical axis passing through each camera, e.g., $\gamma_S$ in Figure A2b) could not be accurately measured in the field, but the "swing" (rotation of the image frame about the "optical axis," the ray passing through the optical center of the lens and the principal point on the image) was approximately zeroed (±0.3°) by leveling the camera bodies, and the camera elevation angles (rotation about the horizontal axis that is perpendicular to the optical axis, e.g., $\alpha_N$ in Figure A2c) were estimated (±0.5°) with a spirit level to be 10.0° at NRL and 9.5° at SUNY. Finally, the focal lengths of the camera lenses (nominally 55 mm at NRL and either 35 mm or 24 mm at SUNY) were carefully measured (±1%) to be 54.7 mm, 35.7 mm, and 23.7 mm, respectively. The "barrel distortion" of the 24 mm lens that produced all of the SUNY photographs except that of flash 8715 was also measured and was applied to correct the corresponding tabulations (but see the discussion below).

[82] Extrapolating the lightning channels (which were nearly straight at the bottom, following the triggering wires) to ground level (estimated from the measured camera elevation angles), it was possible to accurately determine the azimuth angles of the two camera optical axes (e.g., $\gamma_S$ in Figure A2b). This procedure was insensitive to small errors in the camera elevation angles because the triggering wires were nearly vertical. By visually identifying the top of the triggering wire on each image and forcing these points to coincide in the 3-D reconstruction of each channel, it was also possible to correct the measured elevation angle of the NRL camera ($\alpha_N$ in Figure A2c; note that this sketch has been slightly simplified and gives the precise definition of $\alpha_N$ only when $\gamma_N = 0$ so that the optical axis lies in the x-z plane) relative to that of the SUNY camera, which was assumed correct. It would have been better to have two or more fixed objects of known location in the field of view of both cameras, from which to fully determine the camera orientations, but the triggering site was not suitable for this refinement. Table A1 lists the camera orientation parameters that were determined in this manner. Notice that the deduced camera azimuths, as well as the corrected elevation of the NRL camera, varied slightly from flash to flash, presumably because of instability of the tripods on which they were mounted.

[83] The formulae of *Hallert* [1960, Appendix A], together with the camera orientation parameters tabulated above, have been used to convert the points ($X$, $Y$) that were digitized from the photographic prints into absolute angle pairs ($\theta$, $\varphi$) (elevation measured upward from horizontal and azimuth measured clockwise from the direction of the y axis, respectively) that define rays from the camera positions. Then the position parameters in Figure A2a have been used to compute the intersections of these rays ($x$, $y$, $z$) in our Cartesian coordinate system. The latter step is nontrivial and was performed in practice by solving simultaneous equations with the Mathematica (TM) software, following an outline originally due to Stan Heckman (personal communication, 1995).

[84] Figure A3 is a conceptual illustration of the channel reconstruction procedure. (Note that $\alpha_P$ here has been given the opposite sign from Figure A2a, solely for convenience of illustration.) The central problem is that, in general, it is not possible to identify any given point on the lightning channel in one image with the corresponding point in the other image. Therefore this is not the classical double-theodolite problem, where there is redundant data (four angles to determine a point in 3-space). A heuristic description of the channel reconstruction method is as follows. The ray, $\mathbf{l_r}$, that is defined by point $r$ in the first camera image can be projected onto the second camera image as the line, $l'_r$, which intersects the second channel image somewhere (in general, between two of the vertices, $s$ and $s + 1$, as shown in the inset of Figure A3). This intersection point (call it $s'$) defines a ray from the second camera, $\mathbf{l_{s'}}$, that intersects the first ray, defining a point in 3-space (identified by the indices, ($r$, $s'$)) on the reconstructed channel. The apparently redundant piece of information (the fourth angle) is effectively used up to determine the intersection point, $s'$, on the second channel image.

[85] Mathematically, our solution of this problem proceeds from two vector equations, each specifying the location in 3-space of the intersection point, $\mathbf{r}$, of rays $\mathbf{l_r}$ and $\mathbf{l_{s'}}$ in terms of the angles, ($\theta_i$, $\varphi_i$), and the range, $r_i$, from camera $i$:

$$\mathbf{r} = \mathbf{r_{01}} + r_1(\hat{\mathbf{x}}\sin(\phi_1)\cos(\theta_1) + \hat{\mathbf{y}}\cos(\phi_1)\cos(\theta_1) + \hat{\mathbf{z}}\sin(\theta_1))$$
$$\mathbf{r} = \mathbf{r_{02}} + r_2(\hat{\mathbf{x}}\sin(\phi_2)\cos(\theta_2) + \hat{\mathbf{y}}\cos(\phi_2)\cos(\theta_2) + \hat{\mathbf{z}}\sin(\theta_2)) \quad \text{(A1)}$$

The $\mathbf{r_{0i}}$ are the positions of the two cameras; $\hat{\mathbf{x}}$, $\hat{\mathbf{y}}$, and $\hat{\mathbf{z}}$ are the unit vectors in our Cartesian coordinate system. Equating these two expressions for $\mathbf{r}$, we obtain three linear scalar equations in two explicit unknowns, $r_1$ and $r_2$. Recall, however, that the angles from camera 1, ($\theta_1$, $\varphi_1$), are implicitly functions of the index, $r$, whereas those from camera 2 are implicitly functions of $s$ (we have linearly interpolated the angles between integral values of these indices) and that it has not yet been explained how to find the $s'$ (see Figure A3) that corresponds to any particular


**Figure A1.** Still camera images of flash 8732 (a) from the NRL site, located about 5.2 km east of the triggering site and using a 55 mm lens, and (b) from the SUNY site, located about 2.2 km SSE of the triggering site and using a 24 mm lens.

value of $r$. Given $r$, we might simply solve numerically the three simultaneous equations (now nonlinear in the implicit variable, $s$) for $r_1$, $r_2$, and $s'$, as Stan Heckman (personal communication, 1995) originally suggested. Once $r_1$ and $r_2$ are known, it is obviously trivial to find **r** from either of equation (A1). (This approach might be generalized to find the "best" solution, in the least squares sense, from three or more camera images of a single lightning channel.) Because we have only two cameras, however, the computation can be simplified as follows:

[86] Three linear equations in two unknowns have a unique solution if and only if the rank of the $3 \times 2$ coefficient matrix and the rank of the $3 \times 3$ "augmented matrix," **A** (containing an additional column of the constant terms), both equal two [e.g., *Boas*, 1966, section 3.7]. Thus the determinant of the augmented matrix must equal zero. Given a particular value of $r$, the nonlinear equation

$$\det(\mathbf{A}) \equiv 0 \tag{A2}$$

can be solved numerically for the implicit variable, $s'(r)$. From equation (A1) the augmented matrix is found to be

$$\mathbf{A} = \begin{pmatrix} -\sin(\phi_1)\cos(\theta_1) & \sin(\phi_2)\cos(\theta_2) & x_{01} - x_{02} \\ -\cos(\phi_1)\cos(\theta_1) & \cos(\phi_2)\cos(\theta_2) & y_{01} - y_{02} \\ -\sin(\theta_1) & \sin(\theta_2) & z_{01} - z_{02} \end{pmatrix} \tag{A3}$$

where $(x_{0i}, y_{0i}, z_{0i})$ are the known Cartesian components of $\mathbf{r_{0i}}$, the angles, $(\theta_1, \varphi_1)$, are known functions of the specified index $r$, and $(\theta_2, \varphi_2)$ are known functions of the unknown index, $s$. Once $s'$ is determined, the two linear equations with the largest determinant are solved for $r_1$ and $r_2$, and **r** is found.

[87] Occasionally, equation (A2) has multiple solutions for $s'$ at a given $r$. One way to deal with this situation is as follows. Notice that the two rays, one from each camera intersecting at the reconstructed channel point $(r, s')$ in Figure A3, define a plane. This "solution plane" is fully determined by the locations of the two cameras and by the point, $r$, on the first channel image, as described heuristically above. The plane cuts each camera image in a projection line, as further illustrated by $l'_r$ and $l'_{s'}$ in Figure A4, where these projection lines correspond to the point, $r = 155$, on the NRL channel image of flash 8732. (Channel points are numbered here in ascending order from the channel base upward. Note that Figure A4 actually shows the "image planes" after transformation from the original linear measurements on each print, $(X, Y)$, into the absolute angles $(\theta, \varphi)$ (independent of camera orientation, focal length, etc.) since this was the notation in which the data were analyzed mathematically to find points on the lightning channel. Thus "lines" $l'_r$ and $l'_{s'}$ in Figure A4 are not actually straight, although they appear so in these small

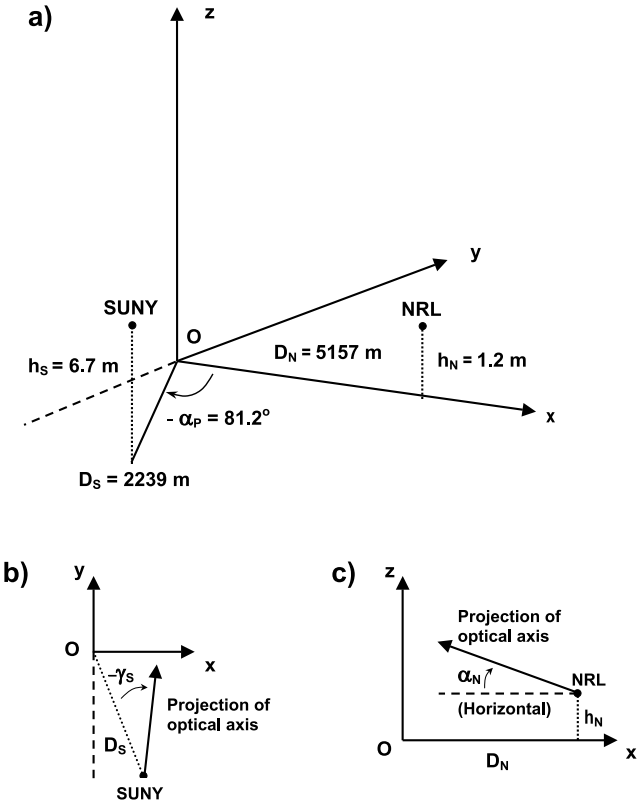


**Figure A2.** Camera locations and orientations at the NRL (subscript N) and SUNY (subscript S) sites relative to the triggering site: the origin, O, of the ($x$, $y$, $z$) coordinate system. (a) $D_i$ and $h_i$ represent the relative ranges and heights of the two cameras. The NRL site is taken to be just above the $x$ axis. Angle $\alpha_P$ represents the coazimuth of the SUNY site. (b) The definition of the camera azimuth angle at the SUNY site, $\gamma_S$. (c) The (simplified, see text) definition of the camera elevation angle at the NRL site, $\alpha_N$.

sections of the images.) There are two interesting facts to note here:

[88] 1. Any channel image vertices that lie on the projection line in one photograph project onto the same line in the other photograph and are thus indistinguishable. For example, points 152–156 on the NRL image all correspond to the projection line, $l'_s$, shown on the SUNY image of the same flash, which intersects that channel image near the point, $s$ = 145, among other places. Close examination of the original photographs suggests channel propagation almost directly toward the SUNY camera in this region.

[89] 2. Downward apparent propagation relative to the projection line in one camera image must correspond to downward apparent propagation relative to the corresponding projection line in the other image. Hence certain channel kinks can be unambiguously identified in both images. For example, the downward loop that is defined by points 162–176 in the NRL image corresponds to the downward loop, points 150–163, in the SUNY image.

[90] Using these conclusions, we can resolve the apparent ambiguity of the multiple solutions that are indicated by the projection lines in Figure A4. Points 152–156 on the NRL image correspond to points 145 and 146 in the SUNY image (not to point 149 nor point 164), whereas NRL segment 161–162 corresponds to SUNY point 149, and NRL segment 176–177 corresponds to SUNY point 164.

[91] Loops of the same sense, such as the pair (NRL 162–176 and SUNY 150–163) identified above, that could be unambiguously associated between the two images were used as a check on the uncertainties that are inherent in our 3-D channel reconstructions. In most of the flashes the top of the triggering wire was readily identifiable in both photographs. (As mentioned above, the elevation angle of the NRL camera was adjusted (in each case by less than the 0.5° uncertainty in our measurement of that angle) to make the top of the wire in both images coincide in the reconstruction.) In each of two flashes (8717 and 8732), there were two obvious kinks, in addition to the top of the wire, that could be used to check the reconstructions. (Figure A4 illustrates one of these four major kinks.) Surprisingly, best agreement was obtained by eliminating the correction for barrel distortion of the 24 mm lens at the SUNY site. In fact, it was found that all identifiable kinks in all of the channel images could be made to coincide by this simple parameter change. In retrospect this seems reasonable, since the barrel distortion was measured at close focus, whereas the lens was actually used at infinity focus, where aberrations are usually minimized by design. Therefore it is presumed that the reconstructions without the barrel distortion correction are the best possible under the circumstances. (The data in Table A1 correspond to this assumption.)

[92] The significance of eliminating the barrel distortion correction, and an example of the uncertainty that is inherent in our reconstructions, are illustrated by Figures A5a and A5b, which show two views of reconstructed channel 8732, with (blue) and without (red, preferred) the correction. Notice that the differences between these two reconstructions are a few tens of meters or less throughout, which is typical. Two views of all six reconstructed channels are given in Figures A6a and A6b. Flashes 8715, 8717, 8725, 8726, 8728, and 8732 are shown in cyan, magenta, blue, green, red, and black, respectively. Notice that there is considerable variability (much greater than a few tens of meters) in both the length of the triggering wire and the overall channel shape among these flashes.

[93] In order to illustrate the impact of uncertainties in the reconstructed channels, Figure A7 compares electric field changes for stroke 2 of flash 8732 that have been calculated from the two different channel reconstructions shown in Figure A5. The shape, amplitude, and propagation speed of the return stroke current waveform that is deduced for this event in the body of the paper has been used in both cases.

**Table A1.** Camera Orientation Angles, as Defined in Figure A2[a]

| | Flash | | | | | |
|---|---|---|---|---|---|---|
| Parameter | 8715 | 8717 | 8725 | 8726 | 8728 | 8732 |
| $\alpha_N$, deg | 9.98 | 9.65 | 10.08 | 9.96 | 9.84 | 9.87 |
| $\gamma_N$, deg | 1.32 | 1.34 | 1.97 | 1.74 | 1.89 | 2.02 |
| $\gamma_S$, deg | −0.77 | −1.33 | −1.61 | −1.74 | −1.16 | −1.68 |

[a] $\alpha_i$ represents elevation relative to the horizontal, and $-\gamma_i$ represents azimuth relative to the direction to the triggering site. Subscript "N" stands for the NRL site, and "S" stands for SUNY.

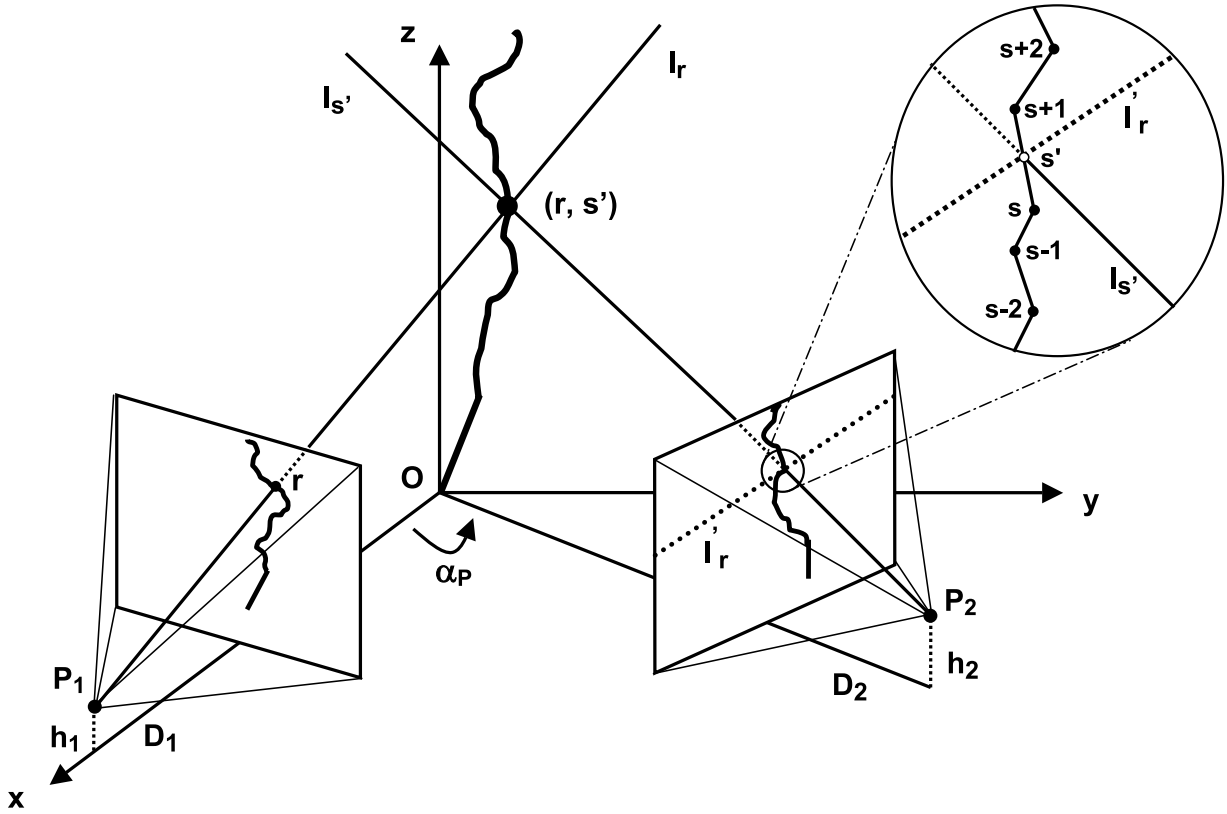


**Figure A3.** A heuristic illustration of the channel reconstruction method used in this paper. The locations of the two cameras are indicated by $P_1$ (representing NRL) and $P_2$ (representing SUNY, except for a change in the sign of $\alpha_P$ for convenience of illustration), with the other parameters as in Figure A2a. Point $r$ on the channel in the first idealized image defines the ray, $\mathbf{l}_r$, which projects onto the second image as the line, $l'_r$. This line intersects that imaged channel at point, $s'$, which in turn defines a second ray, $\mathbf{l}_{s'}$, and a point on the 3-D channel, identified as ($r$, $s'$) (see text).

Again, the blue curve is with, and the red (preferred) curve is without, the barrel distortion correction. The differences between these two waveforms are small and are typical of the impact of geometrical uncertainties on the model field changes in our data set. This satisfying result is a consequence of both the good overall accuracy of the 3-D reconstructions and the considerable smoothing of fine structure that is caused by the rapid increase in current risetime with height, as discussed in the body of the paper.

## Appendix B: Calculation Method for Piecewise Linear Channel

[94] A numerical code was written in Mathematica [TM], following the general outline of the FORTRAN code that had been developed previously by *Le Vine and Meneghini* [1978], to compute the electric field change at the observing site from simulated return strokes in the reconstructed channels. The adoption of the "generalized TLM" form for the stroke current (basically, equations (5)–(7)) allowed a number of simplifications in these calculations. The key attributes of this model are that the entire current waveform propagates monotonically upward along the channel while its principal parameters, $a(s)$, $v(s)$, and $K(t', s)$, depend only on position. Thus the "pure TLM" current parameters that are required on each linear channel segment for equations (2)–(4) (the fixed current waveshape, $I_{TLM}[argument]$, and constant propagation speed, $v$) can be computed in advance from knowledge of the channel geometry. Then the field change calculation can proceed time step by time step.

[95] At each successive time step the current integral on each channel segment is updated for use in equation (4), and a list of the segments from which radiation can reach the observer is computed. Then the contributions to the total field change are summed, both over equations (2)–(4) and over all such "radiating" segments. In this way the field change waveform is built up over time. The size of the time steps is not critical (as long as they are short enough to compute the current integrals with sufficient accuracy), except in the sense that waveform details will be missed if they occur entirely between time steps. As long as the channel segments are made short enough, this calculation method has been shown to accurately approximate the exact field change from a tortuous channel, even when the peak amplitude, risetime, and propagation speed of the current waveform all depend strongly on position. The code has even been shown accurate in the near field by comparison with independent numerical calculations of Jens Schoene (personal communication, 2003) of the University of Florida.

## Appendix C: Analysis of Streak Photographs

[96] Relative light intensity (RLI) determinations from the streak recordings were possible because the data strips

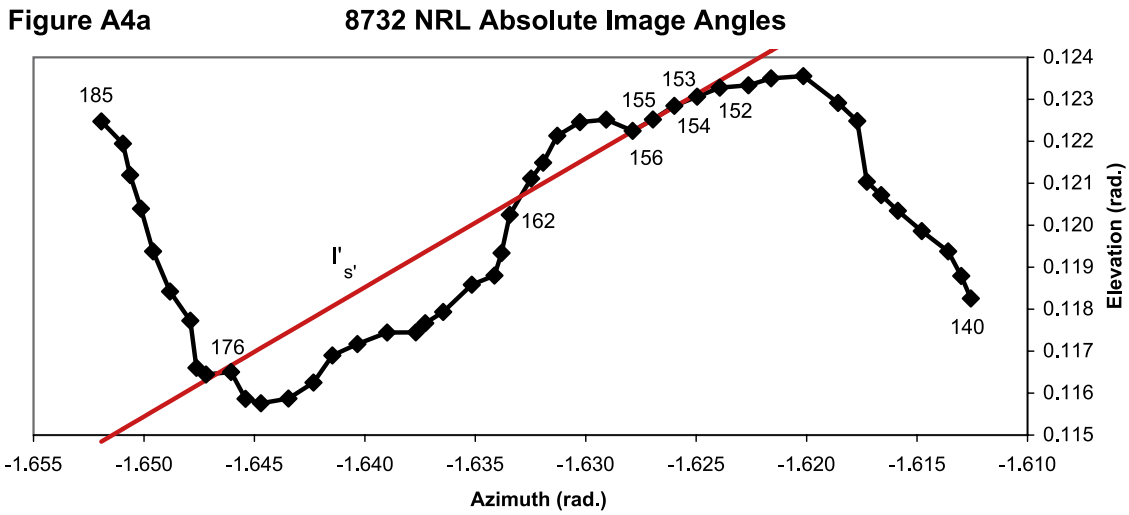


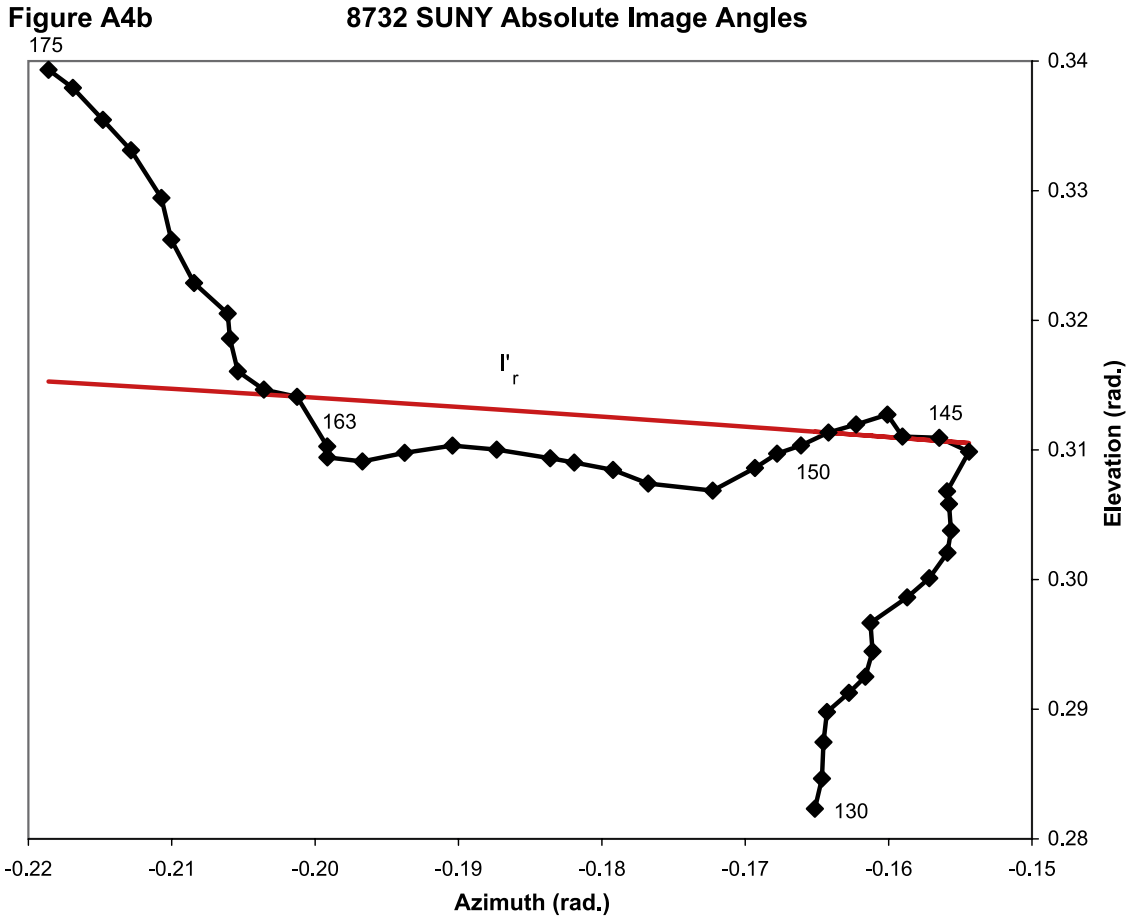


**Figure A4.** Magnified portions of idealized images from the (a) NRL and (b) SUNY cameras, showing a major channel kink, leading to multiple solutions. The graph axes give the absolute elevation and azimuth angles, ($\theta_i$, $\varphi_i$), in radians. Digitized points on the two images are numbered consecutively from the channel base upward. The "lines," $l'_r$ and $l'_{s'}$, where the "solution plane" corresponding to point $r$ = 155 on the NRL image cuts both images are indicated by the solid lines (red). See text for interpretation.

were developed with a "calibration strip" of known relative exposure. Each calibration strip was exposed to a single Xenon flash of about 3 $\mu$s duration, which evenly illuminated a film strip positioned directly behind a Kodak calibration step tablet. The tablet has 21 steps of known density values, thereby transmitting a 1000× range of RLI. With this information, film density can be converted reliably to RLI on a microsecond timescale, as previously demonstrated convincingly by *Jordan and Uman* [1983].

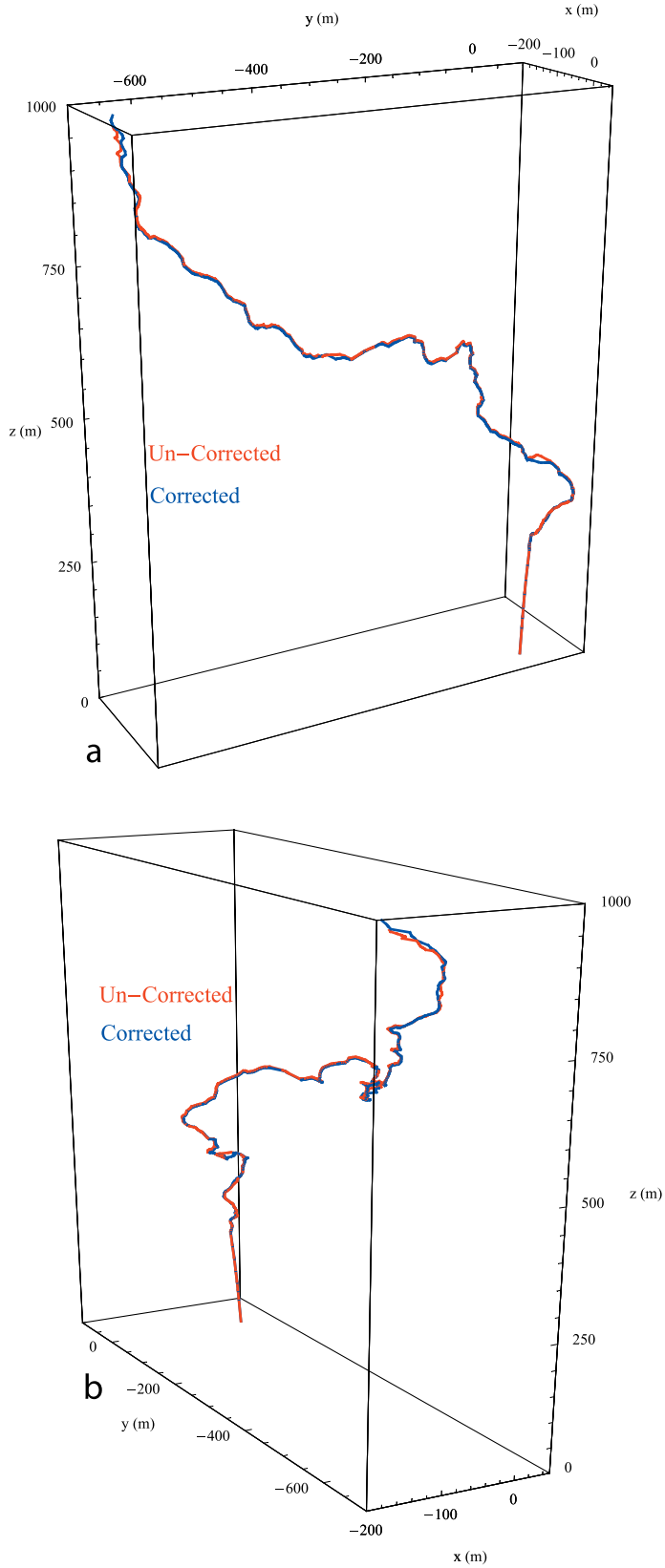


**Figure A5.** Two views of the 3-D reconstructed channel for flash 8732, with (blue) and without (red) the barrel distortion correction to the SUNY lens. The scales of the (x, y, z) axes are in meters relative to the location of the triggering site. (a) This figure shows the view from a location above the surface to the ESE of the triggering site. (b) Similar to Figure A5a but showing the view from a location above the surface to the SSW of the triggering site.

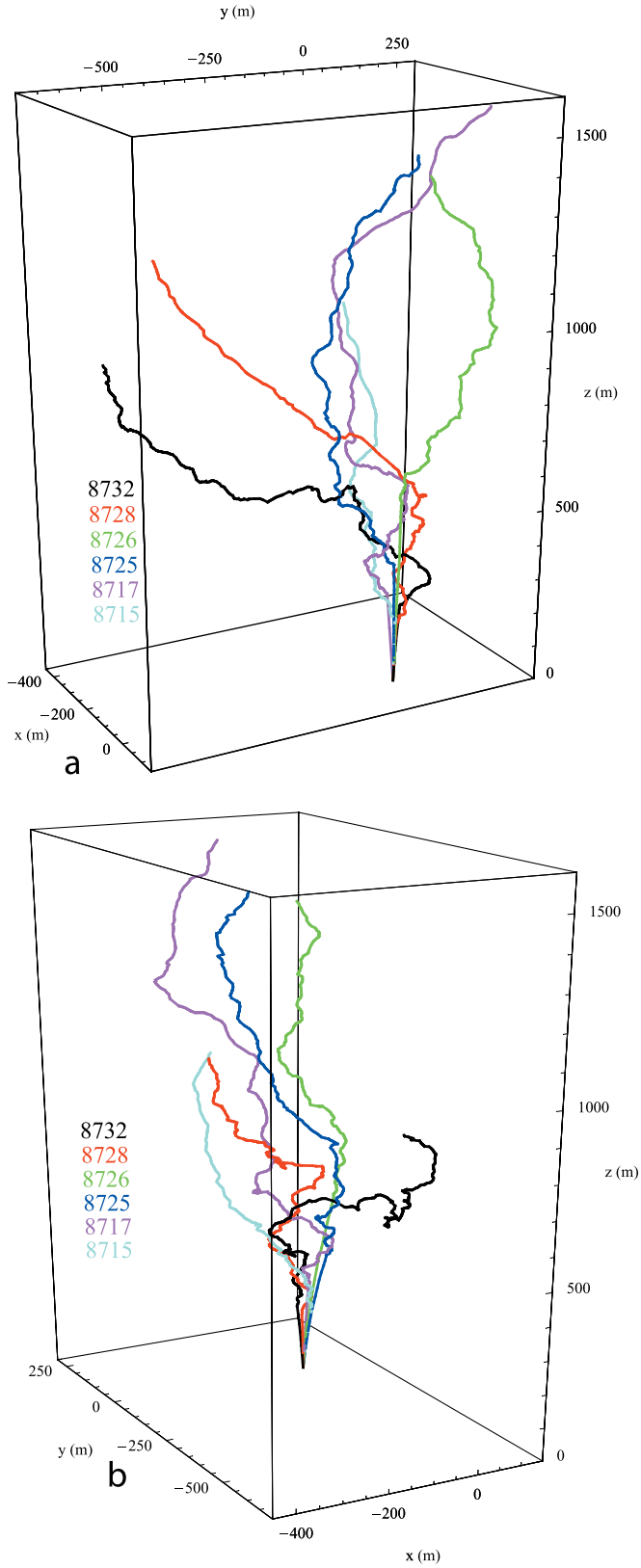


**Figure A6.** (a) Same view as in Figure A5a but this time showing all six reconstructed flashes used in this study. Again, the scales of the (x, y, z) axes are in meters relative to the location of the triggering site. (b) Similar to Figure A6a but from the perspective of Figure A5b.

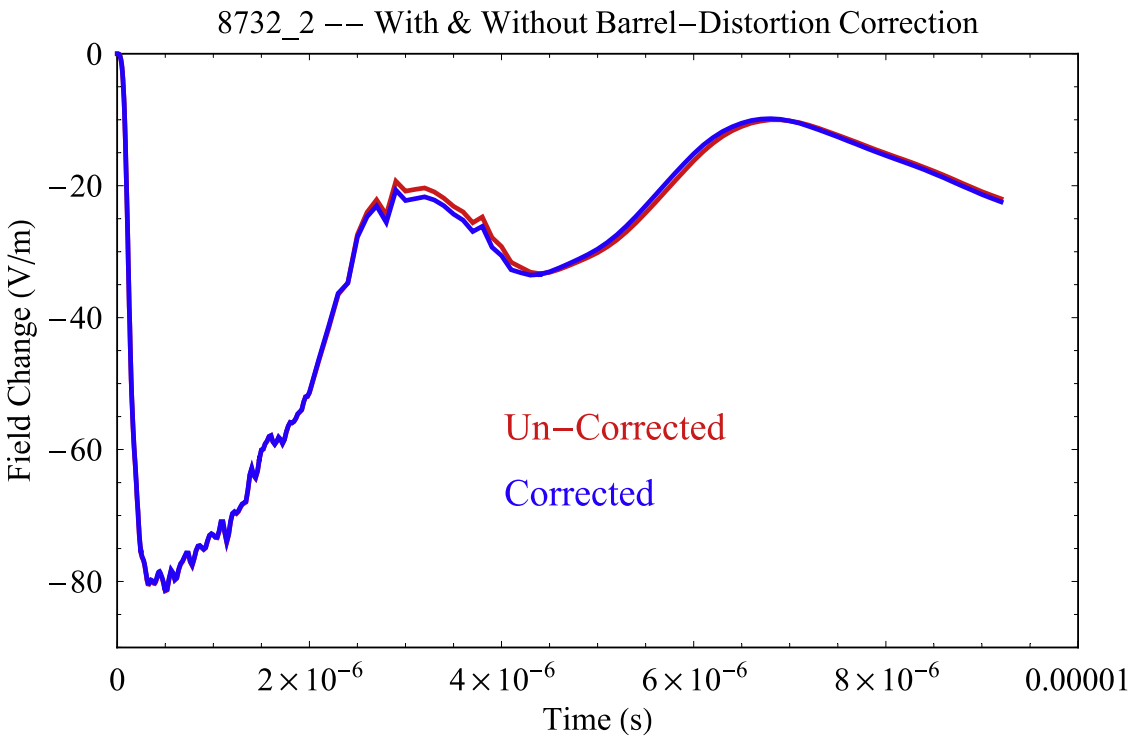


**Figure A7.** Electric field changes computed for stroke 8732/2 using the current model inferred in this paper (see section 5) together with the two channel reconstructions shown in Figure A5. The blue curve uses the barrel distortion correction, whereas the red curve does not.

[97] Here, a Xillix 1412 CCD camera was used to image the data and calibration film strips. The Xillix camera has an image plane sensor of 1344 × 1035 square pixels and 12-bit output, with a specified dynamic range of >60 dB. Various tests confirmed that a factor of slightly more than a thousand in RLI could be reliably recognized with this device, comparable to the range of the Kodak step tablet and the film emulsion itself. The data and calibration strips were imaged with the Xillix camera under identical illumination conditions; the Xillix output for known relative exposures on the calibration strip establishes a "lookup table" for values on the data strip, thereby yielding RLI values for the streak image data. Fortunately, the densities for almost all the data and calibration strips were outside the problematic "toe" and "shoulder" portions of the film response curve, allowing good interpolation accuracy.

[98] All images rendered with the Xillix camera were scanned at 77 pixels per mm on the film, appropriate to having the film grain ultimately limit the analysis. This yields a vertical (spatial) scale of about 0.84 pixels per meter in the object plane and a typical temporal scale of about seven pixels per microsecond for the streak camera.

[99] In this analysis, eight or nine separate vertical levels were first selected for each image, being careful to avoid intense "streak lines" or scratches in the emulsion. Figure 18 for stroke 8725/1 is a typical example. At each preselected vertical level, a horizontal strip of 1344 × 7 pixels centered on that level was then extracted from the digital image and averaged vertically across the seven adjacent pixels (typically about 8 m of channel height) to reduce grain noise. Using the streak camera's known writing rate and the calibration information, the averaged values at each level were converted to a time series of RLI.

[100] The background RLI before the onset of any perceptible leader illumination was estimated separately for the time series of each stroke at each level and used as the zero of RLI for that particular time series. A typical example of the resulting "raw" time series is given in Figure C1, corresponding to level seven (counting upward from the lowest level, always considered level one) of stroke 8725/1. This procedure should allow the RLI to be compared between different levels of the same stroke and also between different strokes in the same flash. (Comparison between strokes in different flashes is potentially somewhat problematic, since they are normally on different pieces of film developed on different days, although in principle the film calibration should permit such a comparison as well.)

[101] To determine the true altitude and the path length along the channel that corresponds to any given level on a streak image, we projected the corresponding three-dimensional channel reconstruction from the perspective of the streak camera and then visually lined up features in the two images. (In many cases it was easier to do this with the leader image when it was visible, since it was often sharper than that of the return stroke.) In this way, for example, level seven of stroke 8725/1 (see Figure 18) was determined to be about 728 m above the surface, or about 886 m of path length of from the channel base. Interpolation was required on the nearly straight sections of channel where the lightning had followed the triggering wire, of course. (The actual bottom of the channel was obscured by an intervening tree line. Consequently, level one was taken as 30 ± 15 m altitude in each case,

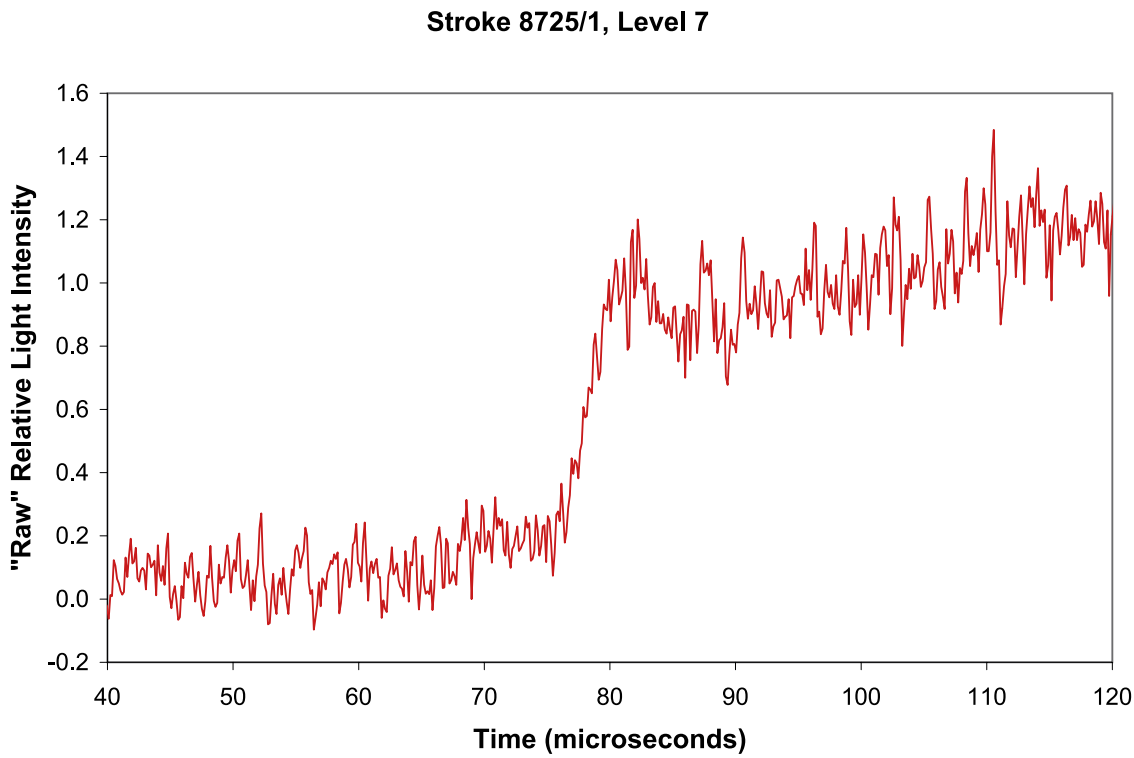


**Figure C1.** "Raw" relative light intensity, after averaging seven pixels vertically and after zero subtraction but before any temporal smoothing, at level seven of stroke 8725/1 (see Figure 18).

on the basis of several lines of evidence.) This procedure allowed the path length corresponding to each level to be determined to an accuracy of ±50 m or better. On the basis of the average 3-D stroke propagation speeds estimated in Table 2, this corresponds to a temporal uncertainty of ±0.3 $\mu$s or better for these events, certainly adequate for our purposes.

[102] Determination of the 10–90% optical risetime and the peak optical amplitude are related by the choice of onset and peak RLI for the return stroke under consideration. Both determinations were made difficult by the noise on the raw RLI data (e.g., Figure C1, already vertically averaged as indicated above), which became a greater problem as the stroke amplitude decreased. In an effort to minimize this noise without unduly broadening the observed risetime, the data were temporally smoothed by the application of a weighted moving average. The weighting function was a "cosine bell" [e.g., *Willett et al.*, 1990, equation A8] with an adjustable full width at half maximum (FWHM), normalized to have unity area. It was found experimentally that, as this FWHM was increased for a given time series, the ratio of apparent risetime to FWHM approached 0.80 (when the risetime became dominated by the width of the weighting function). Therefore FWHM was kept as small as possible, consistent with the unambiguous determination of risetime, and an absolute minimum of 1.6 was imposed on this ratio.

[103] In choosing the onset and peak RLI for each stroke, we focused only on the fast rising portion of the time series (e.g., about 75.5 to 82.5 $\mu$s in Figure C1). This was done both to avoid broadening of the risetime by any light scattering either in the camera or in the film itself and to ignore the gradual rise or "hump" that is often present later in return stroke light emissions, particularly above the surface (again see Figure C1). In general, these levels were chosen by applying excessive smoothing to find an average "baseline" level just before the onset of the fast rising portion, and an average peak or plateau just after it, that were reasonably independent of noise spikes. In the case of large, strongly peaked RLI records (typically at measurement levels near the surface for strokes with large peak currents), however, the peak value was allowed to "float" to the maximum of the smoothed waveform as FWHM was varied.

[104] Once the onset and peak RLI were determined, 10% and 90% levels were "drawn" on the smoothed waveform for automatic determination of the last time that the 10% level was exceeded and the first time that the 90% level was exceeded, their difference being the estimated 10–90% risetime. The FWHM of the smoothing was then gradually increased from zero until the observed risetime stabilized, but not so much that it became steadily increasing. As FWHM increased, risetime typically passed through a minimum, which was generally taken as the best value, and then slowly increased. Often, however, inconveniently located noise spikes were large enough that they caused abrupt jumps in risetime as increasing smoothing caused them to fall below one or the other RLI threshold. In these cases the determination of risetime became more subjective. Sometimes two or more values of risetime seemed consistent with the data, as illustrated in Figures C2a and C2b, for which the relevant parameters are given in the caption. Fortunately, there was normally a rather small range of deduced risetimes in such cases.

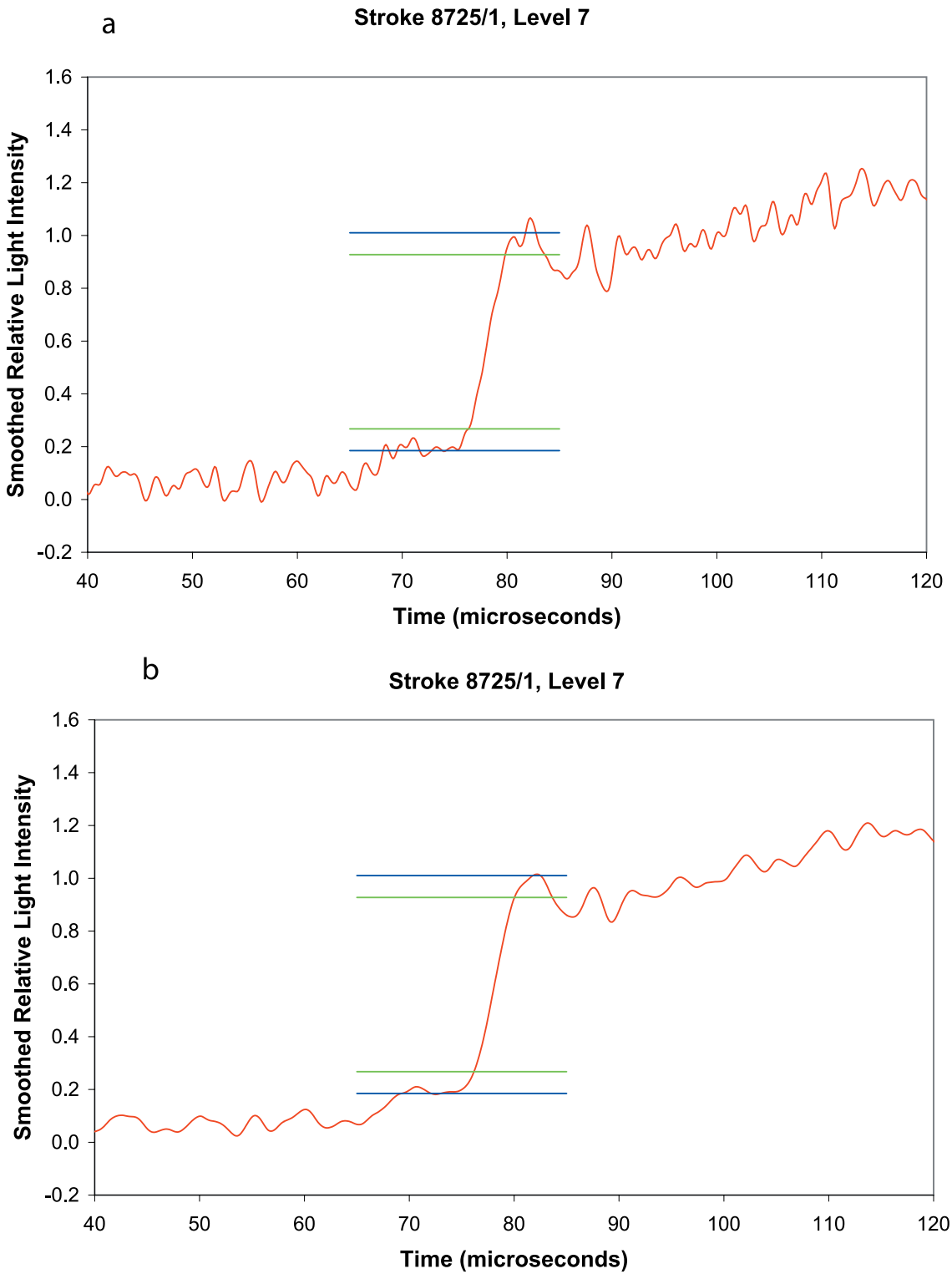


**Figure C2.** Similar to Figure C1 except that temporal smoothing has been added, the "baseline" and peak magnitudes of the fast rising portion of the return stroke RLI have been indicated by the blue horizontal lines, and the corresponding 10–90% levels have been shown by the green horizontal lines. "Baseline" and peak RLI are 0.185 and 1.010, respectively, in both figures. (a) Here the "cosine bell" smoothing comprises 13 horizontal pixels of the streak image, equivalent to a FWHM of 0.81 $\mu$s, yielding a 10–90% risetime of 3.51 $\mu$s. (b) Similar to Figure C2a, but here the smoothing comprises 27 pixels, FWHM = 1.78 $\mu$s, and the 10–90% risetime is 3.78 $\mu$s.

[105] The optical peak amplitude of a stroke was taken as the difference between the baseline and peak values determined above. This measurement is also somewhat subjective, the more so as the stroke amplitude decreases toward the noise level.

[106] **Acknowledgments.** The authors would like to thank W. Jafferis for making the field experiment possible at KSC, C. Leteinturier for making the current data available, S. Heckman for outlining an efficient calculation of channel geometry in Mathematica, J. Schoene for help validating our near-field calculations, and E. P. Krider for valuable consultations and encouragement. The field work was performed while the first author was employed by the Naval Research Laboratory in Washington, D. C., with help from J. C. Bailey and R. V. Anderson. The analysis was conceived for, and begun during, a National Research Council senior associateship at the NASA GSFC; was continued while the first author was employed by the Air Force Geophysics Laboratory (sponsored in part by the Air Force Office of Scientific Research); and has been completed under National Science Foundation individual grant ATM-00004372. Partial support was also provided by NSF grant ATM-9627276.

## References

Baba, Y., and M. Ishii (2002), Lightning return-stroke model incorporating current distortion, *IEEE Trans. Electromagn. Compat.*, *44*, 476–478.

Berger, K., R. B. Anderson, and H. Kroninger (1975), Parameters of lightning flashes, *Electra*, *41*, 23–37.

Boas, M. L. (1966), *Mathematical Methods in the Physical Sciences*, 778 pp., John Wiley, New York.

Bruce, C. E. R., and R. H. Golde (1941), The lightning discharge, *J. Inst. Electr. Eng. London*, *88*, 487–520.

Christian, H. J., V. Mazur, B. D. Fisher, L. H. Ruhnke, K. Crouch, and R. P. Perala (1989), The Atlas/Centaur lightning strike incident, *J. Geophys. Res.*, *94*, 13,169–13,177.

Colvin, J. D., C. K. Mitchell, J. R. Greig, D. P. Murphy, R. E. Pechacek, and M. Raleigh (1987), An empirical study of the nuclear explosion-induced lightning seen on IVY-MIKE, *J. Geophys. Res.*, *92*, 5696–5712.

Cooray, V. (2003), On the concepts used in return stroke models applied in engineering practice, *IEEE Trans. Electromagn. Compat.*, *45*, 101–108.

Cooray, V., and R. E. Orville (1990), The effects of variation of current amplitude, current rise time, and return stroke velocity along the return stroke channel on the electromagnetic fields generated by return strokes, *J. Geophys. Res.*, *95*, 18,617–18,630.

Crawford, D. E. (1998), Multiple-station measurements of triggered lightning electric and magnetic fields, Masters thesis, Univ. of Fla., Gainesville.

Depasse, P. (1994), Statistics on artificially triggered lightning, *J. Geophys. Res.*, *99*, 18,515–18,522.

Diendorfer, G., and M. A. Uman (1990), An improved return stroke model with specified channel-base current, *J. Geophys. Res.*, *95*, 13,621–13,644.

Eriksson, A. J. (1978), Lightning and tall structures, *Trans. S. Afr. Inst. Electr. Eng.*, *69*, 2–16.

Fisher, R. J., G. H. Schnetzer, R. Thottappillil, V. A. Rakov, M. A. Uman, and J. D. Goldberg (1993), Parameters of triggered-lightning flashes in Florida and Alabama, *J. Geophys. Res.*, *98*, 22,887–22,902.

Garbagnati, E., and G. B. Lo Pipero (1982), Parameter von Blitzstromen, *Electrotech. Z.*, *103*, 61–65.

Gomes, C., and V. Cooray (1998), Correlation between the optical signatures and current wave forms of long sparks: Applications in lightning research, *J. Electrost.*, *43*, 267–274.

Guo, C., and E. P. Krider (1982), The optical and radiation field signatures produced by lightning return strokes, *J. Geophys. Res.*, *87*, 8913–8922.

Guo, C., and E. P. Krider (1985), Anomalous light output from lightning dart leaders, *J. Geophys. Res.*, *90*, 13,073–13,075.

Hallert, B. (1960), *Photogrammetry: Basic Principles and General Survey*, 340 pp., McGraw-Hill, New York.

Heidler, F. (1985), Traveling current source model for LEMP calculation, paper presented at 6th International Zurich Symposium on Electromagnetic Compatibility, ETH-Zent., Zurich, Switzerland, March.

Hill, R. D. (1969), Electromagnetic radiation from erratic paths of lightning strokes, *J. Geophys. Res.*, *74*, 1922–1929.

Hubert, P. (1985), A new model of lightning subsequent stroke—Confrontation with triggered lightning observations, paper presented at Tenth International Aerospace and Ground Conference on Lightning and Static Electricity, Assoc. Aeronaut. et Astronaut. de France, Paris, 10–13 June.

Idone, V. P., and R. E. Orville (1982), Lightning return stroke velocities in the thunderstorm research international program (TRIP), *J. Geophys. Res.*, *87*, 6555–6562.

Idone, V. P., and R. E. Orville (1985), Correlated peak relative light intensity and peak current in triggered lightning subsequent return strokes, *J. Geophys. Res.*, *90*, 6159–6164.

Idone, V. P., R. E. Orville, P. Hubert, L. Barret, and A. Eybert-Berard (1984), Correlated observations of three triggered lightning flashes, *J. Geophys. Res.*, *89*, 1385–1394.

Jordan, D., and M. A. Uman (1983), Variations in light intensity with height and time from subsequent return strokes, *J. Geophys. Res.*, *88*, 4903–4915.

Jordan, D., V. A. Rakov, W. H. Beasley, and M. A. Uman (1997), Luminosity characteristics of dart leaders and return strokes in natural lightning, *J. Geophys. Res.*, *102*, 22,025–22,032.

Kodali, V., V. A. Rakov, M. A. Uman, K. J. Rambo, G. H. Schnetzer, J. Schoene, and J. Jerauld (2005), Triggered-lighting properties inferred from measured currents and very close electric fields, *Atmos. Res.*, *76*, 355–376.

Leteinturier, C., and J. Hamelin (1991), Submicrosecond characteristics of lightning return-stroke currents, *IEEE Trans. Electromagn. Compat.*, *33*, 351–357.

Leteinturier, C., C. Weidman, and J. Hamelin (1990), Current and electric field derivatives in triggered lightning return strokes, *J. Geophys. Res.*, *95*, 811–828.

Le Vine, D. M., and M. Kao (1988), The effects of current risetime on radiation from tortuous lightning channels, in *Proceedings of the 8th International Conference on Atmospheric Electricity*, pp. 509–514, Int. Comm. on Atmos. Electr., Uppsala, Sweden.

Le Vine, D. M., and R. Meneghini (1978), Simulation of radiation from lightning return strokes: The effects of tortuosity, *Radio Sci.*, *13*, 801–809.

Le Vine, D. M., and R. Meneghini (1983), A solution for the electromagnetic fields close to a lightning discharge, paper presented at 8th International Aerospace and Ground Conference on Lightning and Static Electricity (ICOLSE), Natl. Interagency Coord. Group, Natl. Atmos. Electr. Hazards Prot. Program, Fort Worth, Tex., 21–23 June.

Le Vine, D. M., and J. C. Willett (1992), Comment on the transmission-line model for computing radiation from lightning, *J. Geophys. Res.*, *97*, 2601–2610.

Le Vine, D. M., and J. C. Willett (1995), The influence of channel geometry on the fine scale structure of radiation from lightning return strokes, *J. Geophys. Res.*, *100*, 18,629–18,638.

Le Vine, D. M., J. C. Willett, and J. C. Bailey (1989), Comparison of fast electric field changes from subsequent return strokes of natural and triggered lightning, *J. Geophys. Res.*, *94*, 13,259–13,265.

Lin, Y. T., M. A. Uman, and R. B. Standler (1980), Lightning return stroke models, *J. Geophys. Res.*, *85*, 1571–1583.

Mach, D. M., and W. D. Rust (1989), Photoelectric return-stroke velocity and peak current estimates in natural and triggered lightning, *J. Geophys. Res.*, *94*, 13,237–13,247.

Mach, D. M., and W. D. Rust (1997), Two-dimensional speed and optical risetime estimates for natural and triggered dart leaders, *J. Geophys. Res.*, *102*, 13,673–13,684.

Master, M. J., M. A. Uman, Y. T. Lin, and R. B. Standler (1981), Calculations of lightning return stroke electric and magnetic fields above ground, *J. Geophys. Res.*, *86*, 12,127–12,132.

Mattos, M. A. da F., and C. Christopoulos (1990), A nonlinear transmission line model of the lightning return stroke, *J. Phys. D Appl. Phys.*, *23*, 40–46.

Mazur, V., and J.-P. Moreau (1992), Aircraft-triggered lightning: processes following strike initiation that affect aircraft, *J. Aircr.*, *29*, 575–580.

Mazur, V., B. D. Fisher, and J. C. Gerlach (1984), Lightning strikes to an airplane in a thunderstorm, *J. Aircr.*, *21*, 607–611.

Mazur, V., B. D. Fisher, and P. W. Brown (1990), Multistroke cloud-to-ground strike to the NASA F-106B airplane, *J. Geophys. Res.*, *95*, 5471–5484.

Murphy, D. P., J. R. Greig, R. E. Pechacek, M. Raleigh, E. Laikin, and S. Hauver (1986), Nuclear explosion induced lightning: A laboratory simulation, *NRL Memo. Rep. 5688*, U.S. Nav. Res. Lab., Washington, D. C., 4 Feb.

Nucci, C. A., G. Diendorfer, M. A. Uman, F. Rachidi, M. Ianoz, and C. Mazzetti (1990), Lightning return stroke models, *J. Geophys. Res.*, *95*, 20,395–20,408.

Olsen, R. C., III, D. M. Jordan, V. A. Rakov, M. A. Uman, and N. Grimes (2004), Observed on-dimensional return stroke propagation speeds in the bottom 170 m of a rocket-triggered lightning channel, *Geophys. Res. Lett.*, *31*, L16107, doi:10.1029/2004GL020187.

Rakov, V. A., and M. A. Uman (1998), Review and evaluation of lightning return stroke models including some aspects of their application, *IEEE Trans. Electromagn. Compat.*, *40*, 403–426.

Rakov, V. A., et al. (1998), New insights into lightning processes gained from triggered-lightning experiments in Florida and Alabama, *J. Geophys. Res.*, *103*, 14,117–14,130.

Rakov, V. A., V. Kodali, D. E. Crawford, J. Schoene, M. A. Uman, K. J. Rambo, and G. H. Schnetzer (2005), Close electric field signatures of dart leader/return stroke sequences in rocket-triggered lightning showing residual fields, *J. Geophys. Res.*, *110*, D07205, doi:10.1029/2004JD005417.

Reazer, J. S., A. V. Serrano, L. C. Walco, and H. D. Burket (1987), Analysis of correlated electromagnetic fields and current pulses during airborne lightning attachments, *Electromagnetics*, *7*, 509–539.

Schoene, J., M. A. Uman, V. A. Rakov, V. Kodali, K. J. Rambo, and G. H. Schnetzer (2003), Statistical characteristics of the electric and magnetic fields and their time derivatives 15 m and 30 m from triggered lightning, *J. Geophys. Res.*, *108*(D6), 4192, doi:10.1029/2002JD002698.

Schonland, B. F. J., D. J. Malan, and H. Collens (1935), Progressive lightning, 2, *Proc. R. Soc. London, Ser. A*, *152*, 595–625.

Strawe, D. F. (1979), Non-linear modeling of lightning return strokes, in *Proceedings of Federal Aviation Administration/Florida Institute of Technology Workshop on Grounding Lightning Technology*, *Rep. FAA-RD-79-6*, pp. 9–15, Fed. Aviation Admin., Melbourne, Fla., March.

Thottappillil, R., and M. A. Uman (1993), Comparison of lightning return-stroke models, *J. Geophys. Res.*, *98*, 22,903–22,914.

Thottappillil, R., V. A. Rakov, and M. A. Uman (1997), Distribution of charge along the lightning channel: Relation to remote electric and magnetic fields and to return-stroke models, *J. Geophys. Res.*, *102*, 6987–7006.

Uman, M. A. (1987), *The Lightning Discharge*, 377 pp., Academic, Orlando, Fla.

Uman, M. A. (1988), Natural and artificially-initiated lightning and lightning test standards, *Proc. IEEE*, *76*, 1548–1565.

Uman, M. A., and D. K. McLain (1970), Lightning return stroke current from magnetic and radiation field measurements, *J. Geophys. Res.*, *75*, 5143–5147.

Uman, M. A., V. A. Rakov, G. H. Schnetzer, K. J. Rambo, D. E. Crawford, and R. G. Fisher (2000), Time derivative of the electric field 10, 14, and 30 m from triggered lightning strokes, *J. Geophys. Res.*, *105*, 15,577–15,595.

Vecchi, G., D. Labate, and F. Canavero (1994), Fractal approach to lightning radiation on a tortuous channel, *Radio Sci.*, *29*, 691–704.

Wang, D., N. Takagi, T. Watanabe, V. A. Rakov, M. A. Uman, K. J. Rambo, and M. V. Stapleton (1999a), A comparison of channel-base currents and optical signals for rocket-triggered lightning strokes, *J. Geophys. Res.*, *104*, 2143–2150.

Wang, D., N. Takagi, T. Watanabe, V. A. Rakov, and M. A. Uman (1999b), Observed leader and return-stroke propagation characteristics in the bottom 400 m of a rocket-triggered lightning channel, *J. Geophys. Res.*, *104*, 14,369–14,376.

Wang, D., V. A. Rakov, M. A. Uman, N. Takagi, T. Watanabe, D. E. Crawford, K. J. Rambo, G. H. Schnetzer, R. G. Fisher, and Z.-I. Kawasaki (2005), Attachment process in rocket-triggered lightning strokes, *Atmos. Res.*, *76*, 412–422.

Willett, J. C., and D. M. Le Vine (1995), 3-D channel reconstruction for triggered lightning return strokes, *Eos Trans. AGU*, *76*(46), Fall Meet. Suppl., F118.

Willett, J. C., and D. M. Le Vine (1996), On the current distribution in lightning subsequent return strokes, in *Proceedings of the 10th International Conference on Atmospheric Electricity*, pp. 492–495, Int. Comm. on Atmos. Electr., Osaka, Japan.

Willett, J. C., and D. M. Le Vine (2002), Lightning return-stroke current waveforms aloft, from measured field change, current, and channel geometry, *Eos Trans. AGU*, *83*(47), Fall Meet. Suppl., Abstract A21E-11.

Willett, J. C., and D. M. Le Vine (2003), Lightning return-stroke current waveforms aloft, from measured field change, current, and channel geometry, in *Proceedings of the 12th International Conference on Atmospheric Electricity* [CD-ROM], Int. Comm. on Atmos. Electr., Versailles, France.

Willett, J. C., J. C. Bailey, V. P. Idone, A. Eybert-Berard, and L. Barret (1989a), Submicrosecond intercomparison of radiation fields and currents in triggered lightning return strokes based on the transmission-line model, *J. Geophys. Res.*, *94*, 13,275–13,286.

Willett, J. C., D. M. Le Vine, M. Kao, and V. P. Idone (1989b), Calculated and observed electric fields of rocket-triggered-lightning return strokes with known channel geometries, *Eos Trans. AGU*, *70*, 1015.

Willett, J. C., J. C. Bailey, C. Leteinturier, and E. P. Krider (1990), Lightning electromagnetic radiation field spectra in the interval from 0.2 to 20 MHz, *J. Geophys. Res.*, *95*, 20,367–20,387.

Willett, J. C., D. M. Le Vine, and V. P. Idone (1995), Lightning-channel morphology revealed by return-stroke radiation field waveforms, *J. Geophys. Res.*, *100*, 2727–2738.

V. P. Idone, Department of Earth and Atmospheric Sciences, State University of New York at Albany, 1400 Washington Avenue, Albany, NY 12222, USA.

D. M. Le Vine, NASA Goddard Space Flight Center, Code 614.6, Greenbelt, MD 20771, USA.

J. C. Willett, P.O. Box 41, Garrett Park, MD 20896, USA. (j.c.willett@comcast.net)